

High temperature oxidation behaviour of boiler steels with emphasis on shot-peening effects - experimental results and simulation

RAVISANKAR NARAPARAJU



SIEGENER WERKSTOFFKUNDLICHE BERICHTE | BAND 9/2013
HERAUSGEBER: PROF. DR.-ING. HABIL. H.-J. CHRIST



RAVISANKAR NARAPARAJU

High temperature oxidation behaviour of boiler
steels with emphasis on shot-peening effects -
experimental results and simulation

Bibliografische Information der Deutschen Nationalbibliothek
Die Deutsche Nationalbibliothek verzeichnet diese Publikation in der Deutschen
Nationalbibliografie; detaillierte bibliografische Daten sind im Internet über
<http://dnb.d-nb.de> abrufbar.

Zugl.: Siegen, Univ., Diss., 2013

Herausgeber:
Prof. Dr.-Ing. habil. H.-J. Christ
Lehrstuhl für Materialkunde und Werkstoffprüfung
Institut für Werkstofftechnik
Paul-Bonatz-Str. 9-11
Universität Siegen
D-57068 Siegen

© Copyright Ravisankar Naraparaju 2013
© Copyright Lehrstuhl für Materialkunde und Werkstoffprüfung,
Universität Siegen 2013
Alle Rechte vorbehalten, auch das des auszugsweisen Nachdruckes,
der auszugsweisen oder vollständigen Wiedergabe, der Speicherung
in Datenverarbeitungsanlagen und das der Übersetzung.
Als Manuskript gedruckt. Printed in Germany.

URN:nbn:de:hbz:467-7647
ISSN 2193-5114

High temperature oxidation behaviour of boiler steels with emphasis on shot-peening effects - experimental results and simulation

DISSERTATION

zur Erlangung des Grades eines Doktors
der Ingenieurwissenschaften

vorgelegt von

Ravisankar Naraparaju, M. Sc.
aus Indien

eingereicht bei der Naturwissenschaftlich-Technischen Fakultät
der Universität Siegen
Siegen 2012

Referent: Prof. Dr.-Ing. habil. H.-J.Christ

Korreferent: Prof. Dr. rer. nat. habil. X. Jiang

Tag der mündlichen Prüfung: 11.10.2013

To my grand father late Sri Venkata Subbarao Tammavarapu

Kurzfassung

Das Ziel dieser Arbeit ist es, die Hochtemperatur-Oxidationsbeständigkeit von Kesselbaustählen zu verbessern. Diese Stähle werden in niedriglegierte (9 Gew.%), mittlere (12 Gew.%) und hochlegierte (18 Gew.%) Chrom (Cr)-Stähle eingeteilt. Die isothermen Oxidationsuntersuchungen werden mit Hilfe der Thermogravimetrie in Laborluft im Temperaturbereich von 700-750°C durchgeführt. Die Oxidschicht, welche auf den Stählen wächst, wurde analysiert und die Oxidationsmechanismen wurden aufgeklärt. Der Cr- Gehalt und die Diffusion von Cr aus der Legierung in Richtung der Oxidationsfront hat einen großen Einfluss auf den Schutz der Stähle. Der Schwerpunkt liegt auf der Wirkung einer Kugelstrahlbehandlung auf das Oxidationsschutzverhalten von mittleren- und hochlegierten Cr-Stählen. Es wurde festgestellt, dass Kugelstrahlen einen erheblichen Einfluss auf die Diffusion von Cr und das Oxidationsschutzverhalten der mittleren Cr-legierten Stähle hat. Dieser Effekt ist noch stärker bei hochlegierten Cr-Stählen ausgeprägt, bei denen Kugelstrahlen die Oxidationsgeschwindigkeit erheblich senkt, da sich auf der Oberfläche eine schützende Chromoxid-Schicht gebildet hat. Auf die kugelgestrahlten Stähle wird das „Dislocation-Engineering“ angewendet, um die Oxidationsbeständigkeit der Stähle zu verbessern. Dies wird durch das Vorglühen der kugelgestrahlten Stähle unter Hochvakuum für unterschiedliche Zeiträume bei der gleichen Temperatur wie der Oxidationstemperatur erreicht. Die vorgeglühten Stähle werden einer Oxidation bei 750°C unterzogen. Mit Hilfe von Focused Ion Beam (FIB) und Transmissionselektronenmikroskopie (TEM) wurden die Oberflächen dieser Stähle untersucht. Es wurde festgestellt, dass das Vorglühen über kurze Zeiträume zur Bildung eines stabilen Netzwerks von Versetzungen führt. Die Dislocation-Engineering-Methode hat sich als sehr effektiver Oxidationsschutz der mittleren Cr-legierten Stähle erwiesen. Die Diffusion von Cr wurde durch dieses Netzwerk verbessert und eine Schutzschicht aus Chromoxid hat sich auf der Oxidationsfront dieser Stähle entwickelt.

Basierend auf den Oxidationsmechanismen, die in den Experimenten beobachtet wurden, wird ein Modell für das gleichzeitige Oxidschichtwachstum (interne und externe Oxidschichtbildung) entwickelt. Dieses Modell wird in das bestehende Simulationstool Incorr eingearbeitet. Dieses Tool simulierte bisher nur das Phänomen der inneren Korrosion. Es funktioniert grundsätzlich durch das Lösen des zweiten Fick'schen Gesetzes mit Hilfe der Finite-Differenzen-Methode (Diffusionskinetik) in Kombination mit thermodynamischen Gleichgewichtsberechnungen. Der wichtigste Beitrag dieser Arbeit ist das Einfügen des externen Oxidschichtwachstums in die Simulation. Die Wirkung vom Kugelstrahlen auf die Mikrostruktur der Legierung wird auch berücksichtigt und in das Modell implementiert. Durch die Modifizierung von Incorr kann das gleichzeitige Oxidschichtwachstum auf den untersuchten Stählen simuliert werden. Die errechneten Ergebnisse zeigen eine gute Übereinstimmung mit den experimentellen Ergebnissen.

Unter Verwendung einer weiter fortgeschrittenen Finite Elemente Methode (FEM) wurde das Netz von quadratischen zu wabenförmigen Strukturen modifiziert. Die Simulation des internen Oxidschichtwachstums wird unter der Verwendung von FEM durchgeführt und die Ergebnisse sind in der vorliegenden Arbeit dargestellt.

Abstract

The goal of this work is to improve the high temperature oxidation resistance of boiler steels. These steels are categorized as low (9 wt.%), medium (12 wt.%) and high (18 wt.%) Cr steels. The isothermal oxidation studies are done with the help of thermogravimetry in lab air in the temperature range of 700-750°C. The oxide scales grown on the steels are analysed and oxidation mechanisms were understood. Cr- content and the diffusion of Cr towards the oxidation front in the alloy has a major ascendancy on the protection behaviour of the steels. Main emphasis is kept on the effect of shot-peening on the oxidation behaviour of medium and high Cr steels. It is found that shot-peening has a considerable influence on the diffusion of Cr and protection behaviour of medium Cr steels. This effect is more pronounced in high Cr steel, where shot-peening has largely reduced the oxidation rate. A protective chromia layer is found to be formed on the surface of the shot-peened high Cr steel. ‘Dislocation engineering’ is applied on the shot-peened steels to improve the oxidation resistance of the steels. This is done by pre-annealing the shot-peened steels under high vacuum for different times at the same temperature as the oxidation temperature. The pre-annealed steels are subjected to oxidation at 750°C. With the help of Focussed Ion Beam (FIB) and Transmission Electron Microscope (TEM), the subsurfaces of these steels are analysed. It is found that the pre-annealing for shorter times has resulted in forming a stable network of dislocations. The dislocation engineering method has proved to be very effective in protecting the medium Cr steels against the oxidation. The diffusion of Cr has been enhanced through this network and a protective chromia layer is developed at the oxidation front of these steels.

Based on the oxidation mechanisms observed from the experiments, a model for the simultaneous oxide scale growth (internal and external oxide formation) is developed. This model is incorporated in the existing simulation tool Incorr. This tool simulates the internal corrosion phenomenon only. It works basically by solving Fick’s second law using the finite difference method (diffusion kinetics) in combination with thermodynamic equilibrium calculations. The major contribution of this work is the addition of external scale growth in the simulation. The effect of shot-peening on the microstructure of the alloying system is also considered and implemented in the model. By modifying the Incorr the simultaneous oxide layer growth on the studied steels is simulated and the results are found to be in reasonable agreement with the experimental results.

The modification of the mesh from a square shaped grain structure to the honeycomb shaped structure was implemented by using a more advanced Finite Element Method (FEM). Simulation of the internal oxide scale growth is performed using FEM and the results are presented in the work.

Acknowledgements

I would like to convey my heartiest gratitude to my Professor, and guide Prof. Dr.-Ing. H.-J. Christ, for taking me and introducing me into this exciting field of high temperature corrosion. It has been a pleasure working with him as a PhD student. His guidance helped me in developing not only in scientific aspect but also in my personality. I would like to thank my best 'Kollega' Dr. Burk for supporting me through the entire period of this journey. I would like to thank Dr. Guillen-Giron, Mr. Wang and Dr. Gorr who made my time pleasant and with full of joy. I am happy to say that the help from Dipl. -Ing. Kramer in organising and developing experimental techniques was exceptional and I am grateful to him.

I would like to mention the names of Dr. Renner and Dr. Kostka from Max-Planck-Institut für Eisenforschung (MPIE), Düsseldorf, without them the whole TEM investigation would not be possible. I am thankful to Dr. Auinger from MPIE, Düsseldorf for his contribution to our simulation work. Prof. Siefert from the group Festkörperphysik / Grenzflächen, University of Siegen has been generous by allowing me to work with Auger electron microscope. I would like to convey my gratitude to him. I convey my deepest thankfulness to Dr. Schulz from DLR (Deutsches Zentrum für Luft- und Raumfahrt), Köln for supporting me in the end phase of my thesis.

I would like to thank all my friends, well-wishers and family members for their co-operation, support and wishes. Last but not the least I am very glad that my wife Lakshmi Deepthi and my cute daughter Sri Hansitha were on my side even throughout the phase of my work.

Table of Contents

Symbols and abbreviations	X
1. Introduction and problem definition	1
2. Technical background and literature review	4
2.1. Alloys for high temperature applications	4
2.2. Basic theory of high temperature oxidation	7
2.2.1. Basic thermodynamics of a chemical reaction	7
2.2.2. Basics of oxidation kinetics.....	10
2.2.3. Solid state diffusion	16
2.2.4. High diffusivity paths in metals.....	17
2.2.4.1. Diffusion along grain boundaries.....	18
2.2.4.2. Diffusion in dislocations	23
2.2.5. Plastic deformation of the surface	24
2.2.5.1. Shot-peening.....	25
2.2.5.2. Shot-blasting.....	26
2.2.5.3. Air blast shot-peening (ABSP).....	26
2.2.5.4. Ultrasonic shot-peening (USSP)	27
2.3. Oxidation of Fe-Cr alloying system	27
2.3.1. Oxidation of iron.....	27
2.3.2. Oxidation of Fe-Cr alloying system	30
2.3.3. Oxidation in the Fe-Cr-Ni alloying system	36
3. Materials and experimental methods	38
3.1 Chemical composition and microstructure of the materials.....	38

Table of contents

3.2	Experimental techniques used for oxide scale characterization.....	43
3.2.1	Light microscopy.....	44
3.2.2	Scanning electron microscopy.....	44
3.2.3	Transmission electron microscopy.....	44
3.2.4	Focused ion beam.....	45
3.2.5	X-ray diffraction.....	45
3.2.6	Auger electron spectroscopy.....	46
4.	Experimental results and discussion.....	47
4.1	Influence of Cr content on the oxidation behavior.....	47
4.1.1	Results on the influence of Cr content on the oxidation behaviour.....	47
4.1.2	Discussion on the effect of Cr content on the oxidation behaviour.....	54
4.2	Effect of shot-peening on the oxidation behaviour.....	55
4.2.1	Effect of shot-peening on the microstructure of the sample.....	55
4.2.2	Effect of shot-peening on the oxidation behaviour of Cr-12 martensitic steel at 700°C and 750°C.....	57
4.2.2.1.	Results.....	57
4.2.2.2.	Discussion.....	67
4.2.3	Effect of shot-peening on Cr-18 at 700°C and 750°C.....	69
4.2.3.1.	Results.....	69
4.2.3.2.	Discussion.....	72
4.3	Dislocation engineering on the shot-peened steels.....	73
4.3.1	Results.....	73
4.3.2	Discussion.....	90
5.	Modelling and simulation.....	96

Table of contents

5.1	Background.....	96
5.2	Physical modelling of the effect of shot-peening on the oxidation behaviour of steels.....	100
5.3	Physical modelling for the simulation of external scale formation.....	102
5.4	Simulation results	107
5.4.1	Simulation of external scale formation	107
5.4.2	Simulation of effect of shot-peening.....	114
5.5	Simulations using finite element method (FEM)	117
5.5.1	Modelling using FEM	117
5.5.2	Simulation results using Comsol.....	119
5.6	Discussion of the simulation results.....	122
6.	Concluding discussion	125
6.1	The mechanisms of internal and external layer formation.....	125
6.2	Effect of Cr content on the oxidation behaviour	126
6.3	Effect of shot-peening on the oxidation behaviour	128
6.4	Dislocation engineering.....	130
6.5	Simulation of the external scale formation and effect of shot-peening	132
7.	Conclusions and future aspects	134
8.	References	137

Symbols and abbreviations

Symbols and abbreviations

Latin symbols

a	Interatomic distance
a_i	Chemical activity of the species i
a_M	Chemical activity of metal
a_{MO}	Chemical activity of metal oxide
a_r	Dislocation pipe radius
A	Surface area
A, B, C	Integration constants
b	Burgers vector
c	Concentration
c_{Cr}	Chromium concentration
c_{gb}	Concentration inside the grain boundary
C_p	Specific heat at constant pressure
C_v	Specific heat at constant volume
d	Spacing between the grain boundaries
d_l	Dislocation length
D	Lattice diffusivity
D^0	Pre-exponential factor for diffusion
D_d	Pipe diffusivity
D_{eff}	Effective diffusion coefficient
D_{gb}	Grain boundary diffusivity
D_{gb}^0	Pre-exponential factor of grain boundary diffusion
D_M	Diffusion coefficient of the metal

Symbols and abbreviations

D_s	Diffusivity at surface
D_x	Diffusion coefficient along x direction
D_y	Diffusion coefficient along y direction
e^-	Electron
E	Activation energy
E_C	Carnot efficiency
E_d	Activation energy of the diffusivity in dislocation
E_{gb}	Activation energy for the grain boundary diffusion
E_s	Activation energy of the diffusivity at surface
\mathbf{E}_u	Unit matrix
E_v^f	Activation energy for the vacancy formation
E_v^m	Activation energy for the vacancy migration
g	Fraction of atomic sites in the grain boundary
G	Gibbs free energy
\mathbf{G}	Shear modulus
h	Electron hole
H	Enthalpy
H_0	Enthalpy of the material at 0K
I	Identity matrix
J	Net flux of the atoms
k	Logarithmic rate constant
\mathbf{k}	Boltzmann constant
k_1	Linear rate constant
k'	Inverse logarithmic rate constant
k_p	Parabolic rate constant

Symbols and abbreviations

K	Equilibrium constant
K	Dimensionless parameter with an order of unity
L_d	Spacing between dislocations
M	Metal
\mathbf{M}	Tridiagonal matrix
M^{2+}	Metal cation
M_I	M atom on interstitial site
M_M	M atom on M site
\mathbf{M}_x	Coefficient matrix with components on x-direction
\mathbf{M}_y	Coefficient matrix with components on y-direction
MO	Metal oxide
n	An integer
n_i	Number of moles of component i
O^{2-}	Oxygen anion
p	Pressure
p_{O_2}	Partial pressure of the oxygen
p'_{O_2}	Partial pressure of the oxygen at the oxide-metal interface
p''_{O_2}	Partial pressure of the oxygen at the oxide-gas interface
$p_{O_2}(\text{MO})$	Dissociation pressure of the metal oxide MO
R	Universal gas constant
\mathbf{R}_x	Diagonal matrix along x direction
\mathbf{R}_y	Diagonal matrix along y direction
s	Grain boundary segregation factor
S	Entropy
t	Time

Symbols and abbreviations

T	Absolute temperature in K
T_m	Melting temperature
T_1	Temperature of heat source
T_2	Temperature of heat sink
U	Internal energy of the system
U_0	Internal energy of the material at 0K
V	Volume
V_I	Vacancy on interstitial site
V_M	Vacancy on M site
$W_V(\lambda)$	Decrease in the dislocation dipole energy
x	Thickness of the oxide scale

Greek symbols

γ	Grain boundary energy
δ	Grain boundary width
δ	Deviation from stoichiometry
ΔE	Change in the activation energy
ΔG	Change in the Gibbs free energy
ΔG^0	Change in the standard Gibbs free energy
Δm	Specific mass gain
$\Delta m'$	Mass gain of a single non-SP side
$\Delta m''$	Mass gain of the SP side of SP sample
$\left(\frac{\Delta m_{\text{non-SP}}}{A}\right)$	Specific mass gain of the non-SP sample
$\left(\frac{\Delta m_{\text{SP}}}{A}\right)$	Specific mass gain of the SP sample

Symbols and abbreviations

$\left(\frac{\Delta m}{A}\right)_{\text{non-SP}}$	Specific mass gain of non-SP side
$\left(\frac{\Delta m}{A}\right)_{\text{SP}}$	Specific mass gain of SP side
ΔS	Change in the entropy
Δt	Difference in time
Δx_l	Variable step width in left direction
Δx_r	Variable step width in right direction
η	Integration variable
θ	Angle of misorientation between grain boundaries
ϑ	Bragg angle
μ_i	Chemical potential of the species i
μ_i^0	Standard chemical potential of the species i
ϑ_i	Stoichiometric constant of the chemical species i
ν	Poisson's ratio
ρ_d	Dislocation density
λ	Wavelength of the X-rays
L	Average distance between dislocations

Abbreviations

ABSP	Air blast shot-peening
BF	Bright Field
COORETEC	Carbon dioxide reduction technology
DF	Dark Field
EDX	Energy Dispersive X-ray analysis
FIB	Focused Ion Beam

Symbols and abbreviations

HP	High Pressure
ICDD	International Centre for Diffraction Data
IP	Intermediate Pressure
LP	Low Pressure
MP	Measuring-point position
SEM	Scanning Electron Microscope
SP	Shot-peening
STEM	Scanning Electron Microscopy
TEM	Transmission Electron Microscope
USSP	Ultrasonic shot-peening
XRD	X-ray diffraction
ZP	Zero-point position

1 Introduction and problem definition

Ever since the first ever power plant was built in the late 19th century, the need for electricity has resulted in the construction of more power plants all over the world. Today, the major portion of the electricity is produced using coal-fired power plants [1-3]. Fuel efficiency and environmental issues drive the need to increase the operating temperatures of the power plants [4-7]. As the temperatures of the power plants increase the need to develop alloys which can withstand the detrimental effects of high temperature exposures during service also increases. The major problem concerning current alloys in power plants is their corrosion/oxidation behaviour at service temperatures and atmospheres. Selection of the alloys and the development of the alloying systems as well as understanding of their corrosion/oxidation mechanisms has been the subject for many researchers for the past decades [8-13].

The development of high-temperature alloys based on Fe, Ni, and Co alloyed with Cr has led to a gradual increase in secondary alloying elements for strengthening purposes accompanied by decreasing the Cr percentage in the alloy [14, 15]. This process has reached a situation where the strength became more satisfactory than the oxidation resistance of the alloy. The growth of non-protective Fe-oxides on boiler steels when exposed to high temperature environment in power plants often controls the service life of components. In general, the growth of these oxides is parabolic in time, but sometimes it is also linear. These oxides are very porous, brittle in nature and have a high point defect concentration. This can cause severe degradation and material failure. Much research work has been done to reduce the growth rates of these oxides by adding Cr to the alloy [16-20]. The key technology that drives high efficiency power plants is the development of advanced materials and coatings with a considerable increase over traditional alloys in creep strength and corrosion resistance. Major attempts have been made for the 9-12wt.% Cr ferritic steels containing boron, cobalt, tungsten, and other elements for both boilers and steam turbines that are capable of operating at temperatures up to 625°C [21, 22]. To operate beyond this limit, vastly improved austenitic steels are being evaluated.

The aim of the submitted work is to improve the oxidation behavior of boiler steels and to develop a simulation tool for the computation of the corrosion behaviour for applications in power plants using experimental data obtained in the framework of the project 'COORETEC'. Microstructural details of the high temperature oxidation behaviour of 9wt.% and 12wt.% Cr ferritic martensitic and 18wt.% Cr austenitic alloys will be examined.

1 Introduction and problem definition

The structure of the work is as follows. After giving the state of literature and theory of oxidation of the Fe-Cr alloying system in chapter 2, the used experimental methods and alloys will be discussed in chapter 3.

High temperature oxidation experiments will be carried out in order to characterise the mechanisms of the oxidation of the different materials which appear in a temperature area of 700-750°C. The influence of Cr content on the oxidation behaviour is investigated and will be discussed in chapter 4. Depending on these results, a model for the external scale formation on these materials will be developed.

Further improvement in the oxidation kinetics of the 12wt.% and 18wt.% Cr alloys is done by applying surface modification techniques such as shot-peening on the materials before the oxidation, and its effect on the oxidation behaviour which will be examined in the same chapter.

For further improvement of the oxidation kinetics of the 12wt.% and 18wt.% Cr steels and experimental verification of the effect on the oxidation behaviour of the materials the concept of dislocation engineering was examined and will be discussed in chapter 4. The idea is based on the action of interfacial defects (dislocations introduced by shot-peening) in the creation and annihilation of point defects supporting the diffusional growth of scales. For the scale growth by cation diffusion, cation point defects (vacancies/interstitials) can be formed/annihilated by the dislocation climb in the metal resulting in an enhancement/reduction in the diffusion of substitutional elements.

A prediction of the service life of boiler steels in corrosive/oxidative atmospheres requires a full understanding of the degradation mechanisms of the material due to high temperature oxidation. The intended model should be useful to simulate such degradation processes under complex conditions and hence, to contribute to new mechanism-based life-prediction methods. The development of the simulation tool KinCorr (Kinetics of Corrosion) is based on the ability to compute solutions of the diffusion equation numerically using local thermochemical equilibrium computation, with simultaneous consideration of different parameters for the description of the influence of the microstructure on oxidation kinetics, e.g. the grain size. The aim of this simulation is to predict the oxidation kinetics (e.g. oxide layer thickness, internal oxidation depth, chemical composition profiles of the alloying elements and corrosion products) of the boiler steels for longer periods of time. From the experimental results, a model for the effect of shot-peening on the oxidation behaviour was developed and is presented in

1 Introduction and problem definition

chapter 5. Implementation of most advanced Finite Element Method in simulating the honeycomb microstructure of the grains and the oxidation behaviour of the studied materials is done in this chapter.

A concluding discussion of the whole experimental study in combination with the evaluated simulation results is given in chapter 6 and the future aspects and conclusions will be presented in chapter 7.

2 Technical background and literature review

2.1 Alloys for high temperature applications

Almost all metals of technological interest oxidise and corrode at high temperature [23]. The material properties such as strength, creep resistance, fatigue and corrosion resistance define the alloy composition at high temperature applications. High temperature applications such as power industries, petrochemical industries, furnace and thermal elements, gas turbines and Solid Oxide Fuel Cell necessitated the development of such alloys having superior properties. Materials used in power industries undergo oxidation and corrosion from boiling water and steam from one side and hot corrosion from the other side due to burning of coal and gas [24]. Aerospace and gas turbine materials undergo degradation due to oxidation and sulphidation at high temperatures. Chemical and petro-chemical industries require materials that can sustain high temperatures coupled with severe oxidising, sulphidising, carburising and other reducing atmospheres. Oxidation can result in sudden loss of strength in furnace materials due to material loss. For the past 50 years researchers have developed several suitable alloying systems for the above applications. These include materials of high melting point, high Young's modulus, good creep resistance, high-temperature strength, and microstructure stability at high temperatures. From the corrosion point of view there is a need to study the properties of the alloys to know how fast a metal can react with atmospheres at high temperatures, the mechanism of the reaction, the corrosiveness of the environment, how to protect the metal to such environment and alloy selection for such applications. Oxidation is the most predominant corrosion problem. Besides, other forms of corrosion are sulphidation, carburisation and nitridation. Sulphidation occurs when the atmosphere is having a high sulphur activity. In a sulphur dioxide environment both oxidation and sulphidation can occur depending upon the partial pressure of oxygen. Both carburisation and nitridation can occur in similar mechanism. When oxygen activity is reduced in a carbon/nitrogen atmosphere, it could lead to carburisation/nitridation while an increase in the oxygen activity would lead to oxidation [25].

The selection of alloy systems is based on the ability to form a protective layer against corrosion attack. This protective layer should offer a high diffusion barrier to the motion of the species that control the oxidation process. The electrical conductivity of the oxide layer is a measure of the diffusivity of the moving ions. A very low conductivity indicates negligible deviation from stoichiometry and, hence, a low diffusivity, which effectively increases the oxidation resistance. A relatively high conductivity oxide will mean/indicate much faster dif-

fusion of the diffusing species [26]. The oxidation resistance of a metal is improved by the addition of suitable alloying elements to the base metal. The alloying element must be present in sufficient concentration to produce the desired oxide layer. The most common alloying elements added to iron for this purpose are chromium, aluminium and silicon [27].

Alloys in power plants

In a power plant, the heat energy either from fuel combustion or nuclear fission is used to produce jets of steam. The kinetic energy of the steam is converted into electrical energy by using a turbine and a generator. Fig. 2.1.1 shows the route followed by the steam and water.

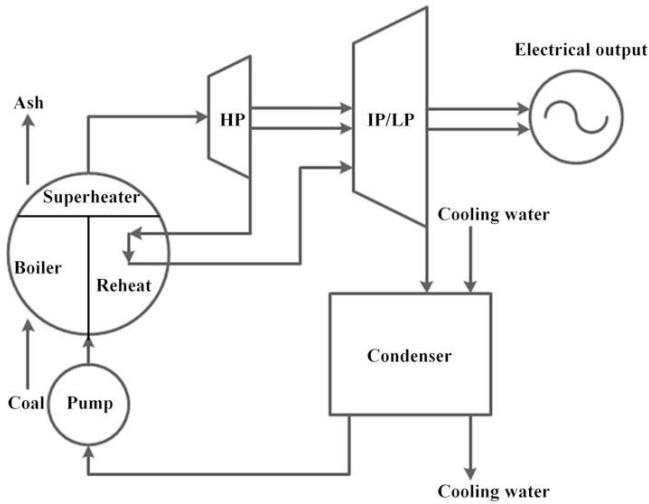


Fig. 2.1.1: Schematic of a power plant steam cycle.

Water is pumped into the boiler, where it is converted into steam, then superheated. It is injected through nozzles onto the blades of the high pressure (HP) turbine. Following this, it is reheated and sent to the intermediate pressure (IP) turbine and then to the low pressure (LP) turbine. The rotary motion of the turbines is used to drive the generator to produce electric power, and eventually the exhaust steam is condensed and further recirculated.

The Carnot efficiency E_C of such a cycle is given by:

$$E_C = \frac{T_1 - T_2}{T_1}. \quad (2.1)$$

2 Technical background and literature review

T_1 and T_2 in the above equation are representing the absolute temperatures of the heat source and the heat sink, respectively. It is, therefore, desirable from both economic and environmental points of view to use operating temperatures as high as possible. Progress in power plant alloy design has allowed T_1 to be increased from 370°C in the 1920s to 600°C or higher (present situation) and there is a drive towards further increases. However, an improvement in thermal efficiency of the plant not only reduces the fuel costs but it also reduces the release of SO₂, NO_x and CO₂ emissions. The latter is very significant with regard to the world-wide agreements to reduce CO₂ emissions and the fact that a 1% increase in efficiency of an 800MW machine would lead to a life-time reduction in CO₂ of approaching 1 million tonnes [28]. These environmental factors have provided an added incentive to building ultra super-critical plants in recent years. The main enabling technology is the development of stronger high-temperature materials, capable of operating under high stresses at ever increasing temperatures.

Under such conditions, there are several life limiting mechanisms, including corrosion, oxidation and fatigue. Steels of 2.25Cr1Mo type have been used in power plants since many decades [29-32], however, recently 9-12CrMoV for the production of pipes and headers capable of operating at inlet steam temperatures of up to 650°C were used [21, 33]. Among the fully commercialised 9wt.% Cr steels, the P91 steel has the highest allowable stress and has been extensively used all over the world as a material for steam pipes for ultra supercritical plants operating at steam temperatures up to 593°C [34]. Alloy P92 is developed by partly substituting Mo by W and can be operated up to 620°C [33]. Beyond 620°C the usage of the 9wt.% Cr is limited due to its corrosion resistance, therefore, the 12wt.% Cr and austenitic steels have to be used. For the conditions and heat treatment of power plants, steels are chosen in providing a fine and stable microstructure containing fine carbides. An austenitisation treatment to dissolve existing precipitates is carried out above 1000°C, the exact temperature depending on the steel composition. The steel is then air cooled. In 2.25Cr1Mo, this results in a predominately bainitic microstructure, but the 9-12wt.% Cr steels are fully air-hardenable, and martensite is formed. Tempering is then carried out, typically at around 700°C, to produce fine carbides and reduce the stored energy in the microstructure so that there is only a very small driving force for microstructural change during service.

Several austenitic alloys consisting of Fe-Cr-Ni were used in the finishing stages of superheater/heater tubing, where oxidation resistance and fireside corrosion becomes important in addition to creep strength at 600°C and above. The high carbon content and the high solu-

tion-annealing temperatures promote a large stable grain size, which provides better creep properties. The steels fall into four categories: 15Cr, 18Cr, 20-25Cr and higher stainless steels. Alloy modifications based on the 18Cr-8Ni steels, such as TP304H, 316H, 347H and Tempalloy A-1 are among the few austenitic steel grades which are used frequently in Europe. The various stages in the evolution of these steels consisted of initially adding Ti and Nb to stabilise the steels from a corrosion point of view, then reducing the Ti and Nb content to promote creep strength rather than corrosion, followed by Cu additions for increased precipitation strengthening by fine precipitation of a Cu rich phase. Further trends have included austenite stabilisation using 0.2% nitrogen and W addition for solid solution strengthening [35].

Several Ni-based alloys like Alloy 617, Ni-Cr based Hastelloy X with further alloying additions of cobalt, molybdenum, and aluminium were intended to apply in service at temperatures in excess of 750°C. These alloys have exceptional creep strength at temperatures above 800°C, enhanced by solution strengthening from the molybdenum and cobalt additions. They have good cyclic oxidation and carburisation resistance, imparted by the chromium and aluminium additions. The alloys retain toughness after long-term exposure at elevated temperatures. They furthermore exhibit good weldability and lower thermal expansion than most austenitic stainless steels.

2.2 Basic theory of high temperature oxidation

2.2.1 Basic thermodynamics of a chemical reaction

The internal energy of a system at any given temperature is defined by

$$U(T) = U_0 + \int_{298}^T C_v dT', \quad (2.2)$$

where U_0 is the internal energy of a material at 298K and C_v is the specific heat at constant volume [36]. The following thermodynamic equations are well explained in the literature [37, 38]. The heat content or enthalpy H of a material is given by

$$H(T) = H_0 + \int_{298}^T C_p dT', \quad (2.3)$$

where H_0 is the enthalpy of the material at 298K and C_p is the specific heat at constant pressure. From the basic laws of thermodynamics, the enthalpy of a system is given by equation 2.4.

2 Technical background and literature review

$$H = U + pV, \quad (2.4)$$

where p is the pressure of the system and V is the volume of the system. The product pV is regarded as the external energy as opposed to the internal energy and is equal to the work done by the system at constant pressure in increasing volume V for itself. For condensed phases like liquids and solids, pV is negligible so that $U \cong H$. H_0 in equation 2.3 represents the energy released when the individual atoms of the material are brought together from gaseous state to form a solid at 298K which is considered as the reference state. If the system releases energy then H_0 is written as negative, and positive when the system gains energy. All the energy that a system processes is not available as work during a chemical change. That part of energy which becomes available as work is called free energy. The part which cannot be released as work is called bound energy. Entropy can be defined as the relation between total energy and free energy given by equation 2.5.

$$S = \int_0^T \frac{C_p}{T'} dT' \quad (2.5)$$

In general, the entropy of a material is zero at 0K and increases as T increases. It is a measure of the disorder introduced in a solid, as it is heated above 0K. The Gibbs free energy G is defined in terms of enthalpy H and entropy S as

$$G = H - TS \quad (2.6)$$

As mentioned earlier, the free energy represents the available part of the energy which can be converted to work. As the temperature increases, H increases, but since TS increases more rapidly than H , G decreases with increasing temperature. The most stable state of a material is the one which has the minimum free energy. For a process occurring spontaneously the free energy must decrease. Changes in their thermodynamic quantities are always defined as the final value minus the initial value.

$$\Delta G = G_{\text{final}} - G_{\text{initial}} \quad (2.7)$$

For a spontaneous process, the free energy change ΔG during the process must be negative. At constant temperature and pressure, condition for a spontaneous change can be written as

$$\Delta G = (\Delta H - T \Delta S) < 0. \quad (2.8)$$

Only if there is no change in the entropy of a system during a process, the enthalpy change ΔH can be used instead of ΔG as a criterion of stability. If an oxide reaction is occur-

2 Technical background and literature review

ring as in equation 2.9 the stability of the reaction can be determined by calculating the Gibbs free energy.



From equations 2.4 and 2.6 at constant temperature and pressure, the Gibbs free energy can be postulated as

$$G = H - TS = U + pV - TS. \quad (2.10)$$

For a system in which compositional change is possible through chemical reaction, the reversible internal change is provided by the basic laws of thermodynamics.

$$dU = TdS - pdV + \sum_i \mu_i dn_i, \quad (2.11)$$

where n_i is the number of moles of component i and μ_i is the chemical potential of the species and is defined as

$$\left(\frac{dG}{dn_i}\right)_{T,p} = \mu_i. \quad (2.12)$$

The combination of equations 2.10 and 2.11 yields equation 2.13:

$$dG = V dp - S dT + \sum_i \mu_i dn_i. \quad (2.13)$$

For an isothermal isobaric system which is in thermodynamic equilibrium, G must be minimum, i.e.,

$$dG = 0, \quad (2.14)$$

integration of equation 2.12 leads to

$$G = \sum_i \mu_i n_i, \quad (2.15)$$

with the condition for equilibrium at constant temperature and pressure

$$\sum_i \mu_i dn_i = 0. \quad (2.16)$$

For an isothermal system of fixed composition of species i , the chemical potential of a species μ_i can be calculated by

$$\mu_i = \mu_i^0 + RT \ln a_i. \quad (2.17)$$

Here, μ_i^0 is the standard chemical potential of the species. R is universal gas constant and a_i is the activity of the species. If the species belongs to the gas phase, the activity must be replaced with the partial pressure of the species. Based on simple assumptions, n_i can be re-

placed by ϑ_i which is called the stoichiometric constant of the chemical species i . Then equation 2.16 can be modified as the condition for equilibrium.

$$\sum_i \mu_i d\vartheta_i = 0. \quad (2.18)$$

Combination of equation 2.15 and 2.18 yields to

$$\Delta G = \sum_i \vartheta_i (\mu_i^0 + RT \ln a_i), \quad (2.19)$$

$$\Delta G = \Delta G^0 + RT \ln K, \quad (2.20)$$

K is called as the equilibrium constant of the reaction. At equilibrium, $\Delta G = 0$, hence,

$$\Delta G^0 = -RT \ln K. \quad (2.21)$$

For the oxidation reaction 2.9, the equilibrium constant can be calculated by

$$K = \frac{a_{MO}}{a_M (p_{O_2})^{\frac{1}{2}}}, \quad (2.22)$$

where p_{O_2} is of partial pressure of oxygen. At this precisely defined temperature-dependent value p_{O_2} , the metal and its oxide co-exist at equilibrium. This value is called the dissociation pressure of the oxide and will be denoted as $p_{O_2}(MO)$.

2.2.2 Basics of oxidation kinetics

Up to a certain extent, equilibrium thermodynamics governs the oxidation of metals. That means, thermodynamics determines which compounds will be formed, but the reaction rates are determined by the oxidation kinetics. The oxidation of a metal includes several fundamental stages referred as elementary steps. These elementary steps include adsorption of gas molecules on the alloy surface, oxide nucleation and growth, oxygen dissolution, oxide scale growth, internal oxidation, formation of cavities and microcracks [27].

Once the formed oxide separates the two phases, the oxidation progresses by means of ionic transport through the oxide layer. These transport mechanisms of ions consist of cation and anion motion. The schematic Fig. 2.2.1 shows the oxidation process through ionic transport for two exceptional cases (a) cation and (b) anion motion.

2 Technical background and literature review

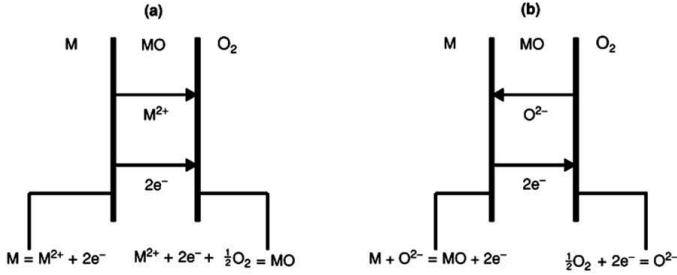


Fig. 2.2.1: Interfacial reactions and transport processes for high temperature oxidation mechanisms: (a) cation motion and (b) anion motion [39].

In the above Fig. 2.2.1, it can be seen that the ions and electrons are migrating through the layer in order for the reaction to proceed. It needs to be noticed that there is an important difference in the scale growth by cation transport and anion transport in that cation migration leads to the scale formation at the scale-gas interface, whereas anion migration leads to scale formation at the metal-scale interface. For a thicker scale, the ionic species have to travel longer distances while for thinner scales the transport distance is less.

If the thickness of the oxide scale is increasing with respect to the oxidation time, the oxidation rate can be fitted mathematically using the following laws.

Linear rate law

During the stage of linear oxidation, the oxidation of a metal proceeds at a constant rate and follows the linear rate law, i.e., equation 2.23

$$x = k_1 t, \quad (2.23)$$

where x is the thickness of the scale and k_1 is the linear oxidation rate constant. The linear rate law is generally observed under conditions where a phase-boundary process is the rate-limiting step for the reaction. Examples are during the steady state of oxidation where the oxide layer is very thin with the reactions occurring at the surface playing a rate determining role. The ionisation of metals in case of cation conductors or ionisation of metal and oxide formation in the case of anion conducting scales are rapid and follow the linear kinetic law as well.

Parabolic rate law

Various high temperature alloys exhibit parabolic oxidation as a function of time. As per this law, the oxide growth occurs with a continuously decreasing oxidation rate. The rate of the

2 Technical background and literature review

reaction is therefore inversely proportional to the scale thickness or the weight of the oxide formed. This is represented as

$$\frac{dx}{dt} = \frac{k_p}{x}, \quad (2.24)$$

after integrating the above equation it yields to

$$x^2 = 2k_p t + C, \quad (2.25)$$

where C is an integration constant.

Logarithmic law

In the case of most of the metals heated at low temperatures, the oxidation kinetics usually obeys a logarithmic behavior where initial oxide formation is characterized by a rapid reaction that slows down quickly to a very low reaction rate. The logarithmic reaction rate law is given in equation 2.26

$$x = k \log(t + t_0) + A, \quad (2.26)$$

and related inverse logarithmic oxidation rate law is given in equation 2.27

$$\frac{1}{x} = B + k' \log(t + t_0), \quad (2.27)$$

where k and k' are the oxidation rate constants for a logarithmic and inverse logarithmic process. It is generally agreed that logarithmic and inverse logarithmic oxidation results from the effect of an electrical potential gradient within very thin oxide layers in assisting ionic transport across the scale.

Wagner theory of oxidation

As explained previously most of the high temperature alloys exhibit parabolic kinetics of oxidation. Wagner has given a model to describe the parabolic oxidation rate [40, 41]. The main assumptions he made are given below.

- (1) The oxide layer is compact and adherent
- (2) Migration of ionic species, ions, electrons or electron holes across the scale is the rate controlling process
- (3) Thermodynamic equilibrium is established at both the metal/scale and scale/gas interfaces

2 Technical background and literature review

- (4) The oxide scale is stoichiometric, hence the ionic fluxes are independent of position within the scale
- (5) Thermodynamic equilibrium is locally established throughout the scale
- (6) Oxygen solubility in the metal is neglected

Since the thermodynamic equilibrium is established at both interfaces, metal/scale and scale/gas, an activity gradient of both metal and oxygen occurs across the scale. Consequently, metal ions and oxygen ions tend to migrate across the scale in opposite directions. As the ions are charged, this migration causes an electric field across the scale consequently resulting in transport of electrons across the scale from metal matrix to gas atmosphere. The relative migration rates of cations, anions, and electrons are therefore balanced and no net charge transfer occurs across the oxide layer. Fig. 2.2.2 gives a summary of the conditions.

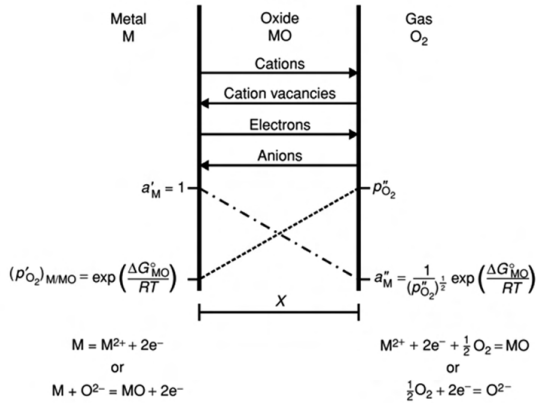


Fig. 2.2.2: Schematic of scale formation according to Wagner's model of oxidation [24].

The parabolic constant of the oxide growth according to Wagner is given by

$$k' = \frac{1}{RT} \int_{\mu_M'}^{\mu_M''} D_M d\mu_M, \quad (2.28)$$

and

$$k' = \frac{1}{RT} \int_{\mu_X'}^{\mu_X''} D_X d\mu_X. \quad (2.29)$$

Here μ_M and μ_X are the chemical potentials and D_M and D_X are the diffusion coefficients of the metal M and non-metal X through the scale respectively.

Limitations of Wagner's model

There are only few oxides strictly obey Wagner's law. The reason is the basic assumptions of the model. The main assumption, a compact and adherent oxide layer formation is not possible for many oxides. Another assumption is that the oxide is more or less stoichiometric which is again rarely observed. Thermodynamic equilibrium at each boundary is also detected seldom. Further ionic transport in many oxides is partly accompanied by grain boundary diffusion. Therefore, most metals show strong deviations from Wagner's law upon high temperature oxidation.

Transport mechanisms in non-stoichiometric compounds

For a long time, it was believed that inorganic compounds have a defined composition, determined by the valence of atoms as per Dalton's law and the atoms were arranged in an ideal and completely ordered structure, with all lattice sites occupied. However, it was recognised that many inorganic compounds, in fact, had a variable composition and today it is well established that an exact stoichiometric composition exists only at a definite partial pressure of the components at a given temperature. Deviation from the stoichiometric composition is called non-stoichiometry.

In non-stoichiometric oxides, defects are often confined either to the oxygen or the metal lattice. They can, therefore, be classified as those containing predominately oxygen defects or those having cation defects. Non-stoichiometric ionic compounds are classified as negative or positive semiconductors.

Some oxides have an excess and others a deficiency of metallic ions, or equivalently a deficiency or excess of oxygen atoms. Fig. 2.2.3 schematically shows a metal excess zinc oxide (ZnO). Here Zn^{2+} is represented as possible occupiers of interstitial sites. Cation conduction occurs over interstitial sites and electrical conductance occurs by virtue of having the excess electrons excited into the conduction band. These electrons are called excess or quasi-free electrons. Zinc oxide is termed as an n-type semiconductor since it contains an excess of negatively charged electrons. Other n-type semiconducting oxides include CdO, TiO_2 , Al_2O_3 , SiO_2 etc.

2 Technical background and literature review

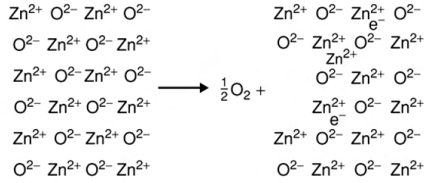


Fig. 2.2.3: Formation of metal-excess ZnO with excess electrons and interstitial Zn ions from perfect ZnO [39].

Nickel oxide, NiO shown in illustration Fig. 2.2.4, is a metal deficient oxide. For each nickel ion vacancy there are two trivalent nickel ions in normal lattice positions. By virtue of energetically close valence states of the cation it is relatively easy for an electron to transfer from a Ni^{2+} to a Ni^{3+} thus reversing the charges on the two ions. The site Ni^{3+} is thus seen to offer a low energy position for an electron and is called an electron hole. Electronic conduction occurs by the diffusion of these positively charged electron holes and hence, this oxide is termed as p-type semiconductor. Ionic transport occurs by the diffusion of nickel vacancies. Other p-type oxides are FeO, Cu_2O , MnO and CoO.

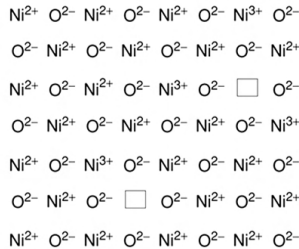


Fig. 2.2.4: Typical p-type metal-deficit semiconductor NiO with cation vacancies and positive holes [39].

Summarizing, the oxidation of some metals is controlled by the diffusion of ionic defects through the scale. A given ionic species can only be mobile if interstitial or vacancy defects exist in its sublattice. Likewise the interface at which new oxide scale is formed is determined by the ionic species which is mobile. In principle, a diffusion-controlled oxidation may be retarded by decreasing the concentration of ionic defects in the scale.

2.2.3 Solid state diffusion

From the above subchapters, it is clear that for the growth of oxide scales, metal ions or oxygen anions must move through the formed oxide layer. At the same time the movement of the oxidising elements to the metal-scale interface defines the oxidation rate and the oxidation products. In order to understand this diffusion mechanism, a basic understanding of the diffusion is required. Diffusion can be defined as the mass flow process by which atoms change their positions relative to their neighbours in a given phase under the influence of thermal energy and a gradient. The gradient can be a concentration gradient, an electric or a magnetic gradient. The thermal energy is necessary for mass flow, as the atoms have to jump from one site to another site during diffusion. The thermal energy is in the form of the vibrations of atoms and about their mean positions in the solid. Most of the diffusion phenomena of interest in metallurgy are described by two fundamental equations. These are known as Fick's first and second laws [42, 43].

If n is the number of moles of atoms per unit area per unit time crossing a plane of area A perpendicular to the diffusional direction x , then Fick's first law is written as

$$J = -D \frac{dc}{dx}, \quad (2.30)$$

where J is the net flux of the atoms, $\frac{dc}{dx}$ is the concentration gradient and D is called the diffusion coefficient and is a constant characteristic of the system. The diffusion coefficient depends on the nature of the diffusing species, the matrix in which it is diffusing and the temperature at which diffusion occurs. The negative sign indicates that the flow of matter occurs opposite the concentration gradient. Fick's first law can be used to describe flow under steady state conditions. Under steady state flow, the flux is independent of time and remains the same at any cross-sectional plane along the diffusion direction.

As it does not include time as a variable, the second law has been formulated for diffusion of a species with respect to time and distance. Here, at any given instant, the flux is not the same at different cross-sectional planes along the diffusion direction x . At the same cross-section, the flux is also not the same at different times. Consequently, the concentration-distance profile changes with time. Fick's second law for unidirectional flow under non-steady state conditions is given by

$$\frac{\partial c}{\partial t} = D \frac{\partial^2 c}{\partial x^2}. \quad (2.31)$$

2 Technical background and literature review

Even though D may vary with concentration, solutions of the differential equation 2.31 are quite commonly used for practical problems, due to their relative simplicity. The solution to the above equation for unidirectional diffusion from one medium to another across a common interface is of the general form

$$C(x, t) = A - B \operatorname{erf}\left(\frac{x}{2\sqrt{Dt}}\right). \quad (2.32)$$

Where A and B are the constants to be determined from the initial and boundary conditions of a particular problem. In the above equation ‘erf’ stands for error function, which is a mathematical function defined as follows:

$$\operatorname{erf}\frac{x}{2\sqrt{Dt}} = \frac{2}{\sqrt{\pi}} \int_0^{\frac{x}{2\sqrt{Dt}}} \exp(-\eta^2) d\eta. \quad (2.33)$$

η is an integration variable that gets deleted as the limits of the integral are substituted.

2.2.4 High diffusivity paths in metals

In general all metals exhibit several structurally different paths by which the atomic diffusion can take place. The defects which allow diffusion through the crystal are atomic defects such as vacancies or interstitials. Grain boundaries, dislocations and free surfaces are introduced only in order to help in attaining equilibrium concentration of point defects. It has been known that the jump rates of atoms along dislocations, grain boundaries and at free surfaces are much higher than in the lattice [44]. Because the diffusivity is high in these regions, the terms high diffusivity paths or diffusion short circuits were used to describe the very fast diffusion phenomena which is shown schematically in Fig. 2.2.5. Lattice diffusion is characterised by its diffusion length \sqrt{Dt} . The deep penetrating diffusion fringes near the free surface, around the grain boundary, and the dislocation line illustrate the effect of high-diffusivity paths [45].

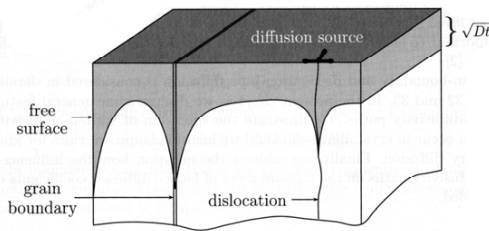


Fig. 2.2.5: Schematic illustration of high-diffusivity paths in a solid [45].

2 Technical background and literature review

High diffusivity paths are of interest for several reasons. First of all there are kinetic processes which are limited by high diffusivity paths. For example, the grain boundary diffusion in polycrystalline materials display a key role at temperatures below $0.6 T_m$ (T_m is the melting temperature). The lattice diffusion represents the most severe constraint to the atomic migration, leading to the lowest diffusivities and the highest activation energies in a given material. Due to their distorted structure, the dislocation cores have smaller constraints for atomic motion than the lattice. High-angle grain boundaries with their less densely packed structure enable fast atomic diffusion. Surfaces offer the least constraints to the motion of the diffusing defects and as a result, both atoms and vacancies can promote the diffusion process. The comparison among the lattice diffusivity D , dislocation pipe diffusivity D_d , grain boundary diffusivity D_{gb} and the diffusivity at surfaces D_s is given below:

$$D \ll D_d \leq D_{gb} \leq D_s. \quad (2.34)$$

For the corresponding activation energies the following inequalities hold:

$$E > E_d > E_{gb} > E_s. \quad (2.35)$$

For example Sockel et al. [46] determined the lattice and the grain boundary diffusion coefficients of O^{18} in polycrystalline chromia. The resulting grain boundary diffusion coefficients are four orders of magnitude higher than those for lattice diffusion. Sabioni et al. [47] measured Cr grain boundary diffusion in the polycrystals of Cr_2O_3 . They found a difference between lattice diffusion and grain boundary diffusion coefficients of three to four orders of magnitude. Atkinson [48] measured the diffusion coefficients along dislocations. According to his calculations, diffusion of Cr in low-angle grain boundaries is about three orders of magnitude faster than lattice diffusion.

2.2.4.1 Diffusion along grain boundaries

Diffusion along grain boundaries is a transport phenomenon of fundamental and technological importance. The grain boundaries provide the most prominent high diffusivity paths. The grain boundary diffusivity usually follows an Arrhenius type of temperature dependence

$$D_{gb} = D_{gb}^0 \exp\left(\frac{-\Delta E_{gb}}{RT}\right), \quad (2.36)$$

where ΔE_{gb} is the activation energy and D_{gb}^0 the pre-exponential factor of grain boundary diffusion.

2 Technical background and literature review

Typically, grain boundary diffusion in metals is four to six orders of magnitude faster than the lattice diffusion [49]. This difference increases with decreasing temperatures due to the smaller activation energy of the grain boundary diffusion compared to lattice diffusion. The pre-exponential factors are not very much different from those of lattice diffusion. Grains in polycrystals without texture are oriented randomly. As a consequence, a wide range of different grain boundaries exists. The nature of a boundary depends on the misorientation of the two adjoining grains and on the orientation of the boundary plane relative to them. Grain boundaries are characterised by at least five microscopic parameters [50-52]: three for the rotation axis and two for the orientation of the grain boundary plane. There are two families of boundaries which are tilt boundaries and twist boundaries. Particular categories which are used to describe boundaries include:

- (1) Low angle boundaries with misorientations smaller than about 15 degrees, which consist of an array of discrete and clearly recognisable lattice dislocations
- (2) High angle boundaries with misorientations larger than 15 degrees, where a lattice dislocation structure is no longer evident
- (3) Special boundaries such as twins with particularly good lattice matching
- (4) General boundaries which rather represent the average type of grain boundaries found in the polycrystalline materials

The most simple grain boundary is a low angle symmetrically tilted grain boundary. This boundary can be considered as an array of parallel edge dislocations. The regions between the dislocations fit almost perfectly into both adjoining crystals whereas the dislocation cores are regions of poor fit in which the crystal structure is highly distorted. The energy of a low angle boundary equals the total energy of the dislocations within the unit area of the boundary. This depends on the spacing L_d of the dislocations and is given by

$$L_d \approx \frac{b}{\theta}, \quad (2.37)$$

where b is the Burgers vector of the dislocations and θ is the angle of misorientation across the boundary. At small values of θ , the dislocation spacing is large and the grain boundary energy γ is proportional to the number density of dislocations in the boundary, $\frac{1}{L_d}$, i.e.,

$$\gamma \propto \theta. \quad (2.38)$$

2 Technical background and literature review

As the misorientation between the two grains increases, the strain fields of dislocations progressively cancel each other so that γ increases slower than equation 2.38 predicts. In general when misorientation exceeds 10 to 15 degrees the dislocation spacing is so small that the dislocation cores overlap. It is then impossible to identify individual dislocations. At this stage, the grain boundary energy is almost independent of the misorientation. The high angle boundaries contain large areas of poor fit and have a relatively open structure. The bonds between the atoms are broken or highly distorted and consequently the grain boundary energy is high [52]. The grain boundary energy plays a central role in the grain boundary diffusion and segregation of foreign atoms to the boundary. As a rule of thumb, the high angle grain boundary energies are often found to be about one third of energy of the free surface. In low angle boundaries, however, most of the atoms fit very well into both lattices so that there is little free volume and the interatomic bonds are only slightly distorted. The regions of poor fit are restricted to dislocation cores.

Most of the mathematical treatment of grain boundary diffusion is based on the model first proposed by Fisher [53]. The grain boundary is represented by a semi-infinite and an isotropic slab of high diffusivity isotropic crystal. The grain boundary is described by two physical parameters: the grain boundary width δ and the grain boundary diffusivity D_{gb} which is considered to be much larger than the lattice diffusion coefficient. The grain boundary width is of the order of an interatomic distance. $\delta \approx 0.5$ nm is a widely accepted value. The schematic representation of Fisher's model is shown in Fig. 2.2.6.

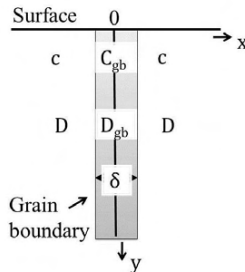


Fig. 2.2.6: Schematic geometry in the Fisher model of GB diffusion.

Atoms which diffuse along the grain boundary eventually leave it and continue their diffusion path in the grains, thus giving rise to a lattice diffusion zone around the grain boundary. The total concentration of the diffuser in the specimen is the result of two contributions: a

2 Technical background and literature review

concentration c , established either directly by in-diffusion from the source or by leaking out from the grain boundary and the concentration inside the grain boundary, c_{gb} .

Mathematically, the diffusion problem can be described by applying Fick's second law to diffusion inside the grains and inside the grain boundary slab. For composition independent diffusivities we have:

$$\frac{\partial c}{\partial t} = D \left(\frac{\partial^2 c}{\partial y^2} + \frac{\partial^2 c}{\partial x^2} \right) \quad \text{for } |x| \geq \frac{\delta}{2}, \quad (2.39)$$

$$\frac{\partial c_{gb}}{\partial t} = D_{gb} \left(\frac{\partial^2 c_{gb}}{\partial y^2} + \frac{\partial^2 c_{gb}}{\partial x^2} \right) \quad \text{for } |x| \leq \frac{\delta}{2}, \quad (2.40)$$

then the concentration field depends on the variables y and x . After suitable initial and boundary conditions have been chosen, the mathematical problem reduces to the solution as following [54]:

$$\frac{\partial c}{\partial t} = D \left(\frac{\partial^2 c}{\partial y^2} + \frac{\partial^2 c}{\partial x^2} \right) \quad \text{for } |x| \geq \frac{\delta}{2}, \quad (2.41)$$

$$\frac{\partial c_{gb}}{\partial t} = D_{gb} \left(\frac{\partial^2 c_{gb}}{\partial y^2} + \frac{2D}{\delta} \left(\frac{\partial c}{\partial x} \right)_{x=\frac{\delta}{2}} \right) \quad \text{for } |x| \leq \frac{\delta}{2}. \quad (2.42)$$

First part of the second equation of the equation 2.42 represents the concentration change due to diffusion in the grain boundary. The second term describes the concentration change due to the leakage of the diffusing species through the walls of the grain boundary slab into the grains.

Harrisons classification of the diffusion kinetics

Depending on the relative importance of the various elementary processes, different diffusion kinetics can be observed. Each regime prevails in a certain domain of annealing temperatures, annealing times, grain sizes, lattice and grain boundary parameters. According to Harrisons [55] these regimes can be divided into three regimes: type A, B and C as shown in Fig. 2.2.7.

2 Technical background and literature review

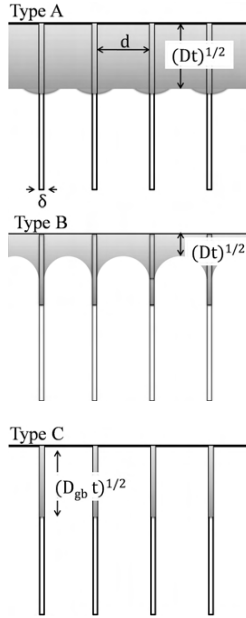


Fig. 2.2.7: Schematic illustration of type A, B and C diffusion kinetics in a polycrystal containing uniformly spaced grain boundaries [54].

Type A kinetics regime

Type A kinetics is observed after diffusion annealing at high temperatures or with longer annealing times or materials with fine grains. Monte Carlo simulation work by Belova and Murch [56] has shown that the lattice diffusion length \sqrt{Dt} , needs to be only a little larger than the spacing d between the grain boundaries.

$$\sqrt{Dt} \geq \frac{d}{0.8} \quad (2.43)$$

Then the diffusion fringes around neighbouring grain boundaries overlap and a diffusing atom may visit more grains and grain boundaries during a diffusion experiment. This results in a diffusion front almost planar with a penetration depth proportional to \sqrt{t} . From a macroscopic point of view the polycrystal obeys Fick's 2nd law for a homogenous medium with an effective diffusion coefficient D_{eff} . Hart's equation for an effective diffusion coefficient in polycrystals is given by [57].

$$D_{\text{eff}} = g D_{\text{gb}} + (1 - g)D. \quad (2.44)$$

2 Technical background and literature review

In the above equation, g is the fraction of atomic sites in the grain boundary of the polycrystal, which can be written as

$$g = \frac{q\delta}{d}, \quad (2.45)$$

where q is a numerical factor depending on the shape of the grain.

Type B kinetics regime

If the temperature is lower, and/or the diffusion anneal is shorter or the grain size is larger than in the previous case, the diffusion is dominated by the so-called B regime. The condition for this regime is

$$s\delta \ll \sqrt{Dt} \ll d. \quad (2.46)$$

Here s is the grain boundary segregation factor of the diffusing atoms. Again the grain boundary diffusion takes place simultaneously with volume diffusion around the grain boundaries, but in contrast to the A regime, the volume diffusion fields of the neighbouring grain boundaries do not overlap each other. Individual grain boundaries are thus isolated.

Type C kinetics

If starting from the B regime, going to lower temperatures or shorter annealing times, then the volume diffusion is almost frozen out and diffusion only takes place along the grain boundaries, essentially without any leakage to the volume. In this regime type C, the condition is given by

$$\sqrt{D_{gb}t} \ll s\delta. \quad (2.47)$$

2.2.4.2 Diffusion in dislocations

The diffusion of atoms is more rapid along dislocations than through the lattice. Since all crystals contain dislocations, any diffusion rate measured will also contain a contribution of dislocations. This can be negligible for low dislocation densities at higher temperatures. However, it becomes more important at low temperatures because of low activation energy for dislocation diffusion relative to the lattice diffusion. For diffusion controlled processes such as metal oxidation, diffusion along dislocations can be a dominant mode of the transport of the atoms. In general, in a heavily deformed metal the dislocation density can reach 10^{16} per

m^2 [58]. The average distance Λ between dislocations depends on the dislocation arrangement. It is given by

$$\Lambda = \frac{\mathbf{K}}{\sqrt{\rho_d}}, \quad (2.48)$$

where \mathbf{K} is of the order of unity. Following the Harrison's [55] grain boundary diffusion classification, three kinetic regimes of dislocation diffusion can be distinguished. The occurrence of a particular regime depends on the average dislocation distance and the lattice diffusion length. Type A kinetics is observed for

$$\sqrt{Dt} > \Lambda, \quad (2.49)$$

in this case, diffusion fields of neighbouring dislocations heavily overlap. Type B kinetics prevail for

$$a_r \ll \sqrt{Dt} \ll \Lambda, \quad (2.50)$$

where a_r is the dislocation pipe radius. Then, the overlap of diffusion fields from neighbouring dislocations is negligible. Type C kinetics occurs for

$$a_r > \sqrt{Dt}, \quad (2.51)$$

when diffusion is restricted to the dislocation core.

2.2.5 Plastic deformation of the surface

Materials deform in response to an externally applied stress. This deformation can be permanent or temporary. When the stress is sufficient to permanently deform the metal it is called plastic deformation. Plastic deformation can occur under tensile, compressive or torsional loads. There are two basic modes of plastic deformation called slipping and twinning. Slip is a shear deformation that moves atoms by many interatomic distances relative to their initial positions, twinning on the other hand changes the orientation of the twinned part of the crystal with respect to the untwinned parts [58]. Here, the movement of an atom relative to its neighbours is only a fraction of interatomic distance.

In order for large metal crystals to deform at their observed low shear strengths, a high density of dislocations must be present. The dislocation density increases with increased cold deformation. The exact mechanism by which the dislocation density increases by cold work is not completely understood. New dislocations are created by the cold deformation and must

interact with those already existing. As the dislocation density increases with deformation, it becomes more and more difficult for the dislocations to move through the existing forest of dislocations, and thus metal hardens with increased cold deformation. One such kind of cold deformation is shot-peening and it is discussed in detail as following.

2.2.5.1 Shot-peening

Shot-peening (SP) is a mechanical surface treatment in which small spherical peening media with sufficient hardness are accelerated in a peening device of various kinds and impact with the surface of the treated work piece with a quantity of energy able to produce surface plastic deformation. The aim of the process is the creation of compressive residual stresses close to the surface for hardening of the same layer of material. These effects are very useful in order to completely prevent or strongly retard the failure of the part [59-63]. There exists a lot of literature about the ability of SP to improve the mechanical behaviour of the materials [64-67], and most of them affirm that the effect of shot-peening is mainly related to the induced residual stresses. Miller [68] pointed out that the shot-peening effect could be related to the grain distortion and to increased microstructural barriers. He proposed that due to the multiplication of structural defects and dislocations, a crack would propagate with more difficulty in work-hardened surfaces. Recent results show that in some cases, the surface hardening can be considered as the main cause of modified behaviour of shot-peened materials [69, 70].

In general, the shot-peening treatment can be considered to obtain nano-structured materials. The concept of nano-crystallisation by the shot-peening is that during the process of the collision of high energy particles, many pits as well as extruded ridges around the edge of the pit are formed on the surface. When the ridge is hit by another particle, the contact area between sample and particle can decrease significantly, therefore the strain and strain rate can be increased. Additionally, the collision mode is also changed from single direction to multiple directions due to the ridge, which is more favorable to the accumulation of dislocations. With the proceeding of the collisions, some areas will approach the critical condition of nano-crystallisation after several suitable collisions [71]. Recent researches have successfully shown that different shot-peening processes are able to introduce the nano-structured layers with different characteristics concerning their depth, the dimension of the crystals and microstructural properties. These methods are different for the needed technological facilities

as well as for the mechanics of the treatment itself. The following gives a very brief introduction about each of these processes.

2.2.5.2 Shot-blasting

In this method, the specimen's surface is sandblasted repeatedly by high-speed sand particles. In contrast to other SP methods, in shot blasting the size and also the geometry of shots are typically random and accidental and shot sizes are in general smaller in comparison with the shots used in air blast shot-peening. The sandblasted surface layer is heavily (plastically) deformed and consequently has a high density of dislocations. After annealing, the initially formed dislocation network or fine "sub-grains" change to nano-sized grains with sharper grain boundaries. It is observed that the mechanical properties of the sandblasted surface are commonly inferior to those of a sandblast-annealed surface. This can be attributed to the different characteristics of nano-grains after annealing [72, 73].

2.2.5.3 Air blast shot-peening (ABSP)

Air blast shot-peening is a SP process through which the shots are projected by compressed air. The equipment is schematically illustrated in Fig. 2.2.8. During air blast shot-peening, when higher shot speed and larger coverage than at conventional operations is applied, the subsurface area is uniformly affected, the shot velocity has a narrow distribution and the impact direction of shot to specimen is almost perpendicular. Air pressure, shot size and shot materials are the process parameters that mainly affect the results of the treatment and the characteristic of the subsurface.

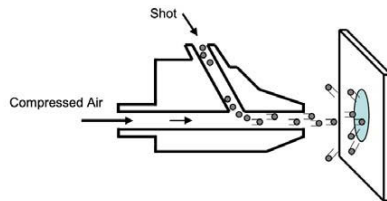


Fig. 2.2.8: Schematic representation of the equipment of ABSP [74].

2.2.5.4 Ultrasonic shot-peening (USSP)

The experimental setup of ultrasonic shot-peening is illustrated in Fig. 2.2.9. In this method the shots are resonated by vibration of an ultrasonic transducer and the impact directions of the balls onto the sample surface are rather random. Repeated multidirectional impacts at high strain rates onto the sample surface result in severe plastic deformation and grain refinement is progressively down to the nanometer regime in the entire sample surface. Obvious enhancement in the overall properties and performance of the materials is observed after the USSP treatment.

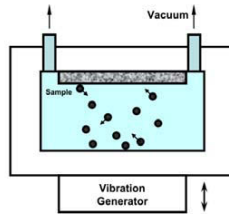


Fig. 2.2.9: Schematic representation of USSP [74].

2.3 Oxidation of Fe-Cr alloying system

2.3.1 Oxidation of iron

Most of the power plant materials are made of Fe-based alloys. The oxidation behaviour of pure iron has been extensively studied and well understood [75, 76]. Iron oxidises to form a multi-layer scale consisting of FeO (wustite), Fe₃O₄ (magnetite), and Fe₂O₃ (hematite) with FeO next to the metal [76]. The oxidation mechanism in iron is mainly controlled by the cation transport through wustite/magnetite and by anion diffusion through hematite and follows a parabolic oxidation behaviour. The phase diagram of the Fe-O system by varying the temperature and amount of oxygen is given in Fig. 2.3.1.

Paidassi [77] studied the oxidation behaviour of iron in air at temperatures between 700-1250°C and found that the scale is always composed of three continuous, compact layers of FeO, Fe₃O₄, and Fe₂O₃. The relative thicknesses of these layers were found to be in the relation 95:4:1. FeO is metal rich and requires the lowest partial pressure. Fe₂O₃ is oxygen rich and requires a higher partial pressure of oxygen to form.

2 Technical background and literature review

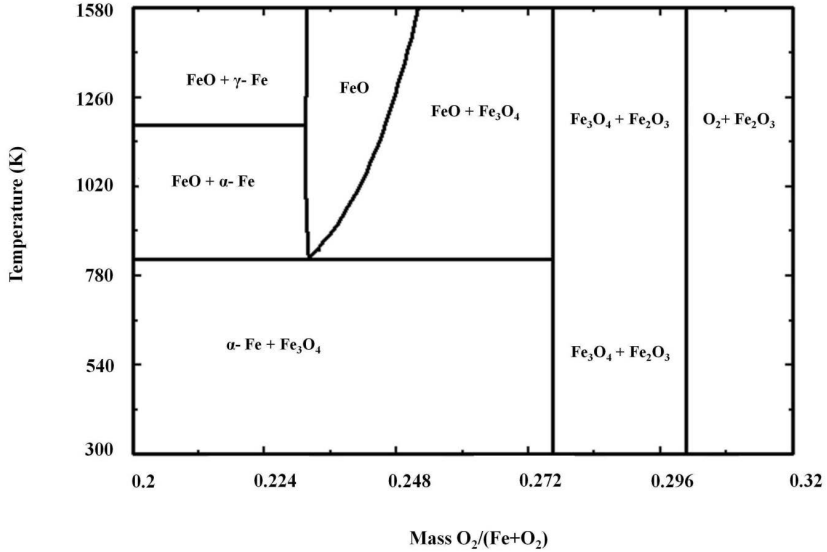


Fig. 2.3.1: Iron oxygen phase-diagram calculated using FactSage.

The wustite phase is a p-type metal deficit semiconductor which can exist over a wide range of stoichiometry, from $\text{Fe}_{0.95}\text{O}$ to $\text{Fe}_{0.88}\text{O}$ at 1000°C [23]. With such a high degree of non-stoichiometry, the mobility of the cations and the electrons via vacancies and electron holes is extremely high in wustite forming a very thick oxide layer. The wustite layer has a relatively high plasticity and poor adhesion to metal forming a porous inner layer. The formation of FeO is taken as a sign of the beginning of rapid degradation.

Magnetite has a spinel structure. As explained previously, at higher oxygen partial pressures, the oxide is metal deficient and at low oxygen partial pressures, the oxide has a cation excess, with iron ions on interstitial sites as the dominant defects. The degree of non-stoichiometry in hematite is small. The oxide has been reported to be oxygen deficient, but the non-stoichiometry was not measured with sufficient accuracy to permit any definite conclusions about the predominant defects. Hematite exists in α and β , rhombohedral and cubic crystal structure.

Generally, at $T > 400^\circ\text{C}$, Fe_3O_4 is oxidised to $\alpha\text{-Fe}_2\text{O}_3$. In the rhombohedral form, the oxygen ions exist in a close packed hexagonal arrangement with iron ions. With such a structure, it is expected that iron ions would be mobile interstitially. On the basis of the knowledge of

2 Technical background and literature review

the structure and the diffusion properties of the iron oxides, the mechanism of three layer oxide on pure iron above 570°C is shown in Fig. 2.3.2.

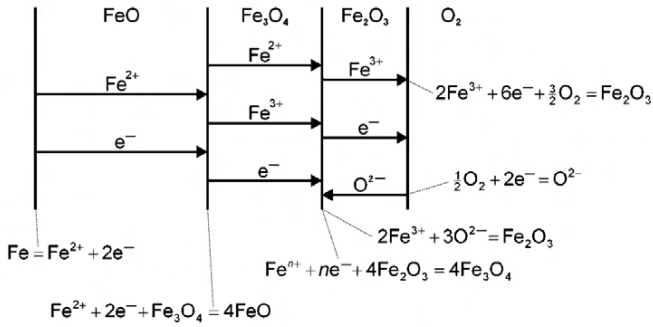


Fig. 2.3.2: Oxidation mechanism of iron to form a three-layered scale above 550°C showing diffusion steps and interfacial reactions [39].

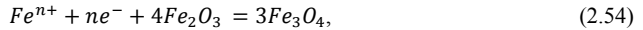
At the iron-wustite interface, iron ionises according to equation 2.52.



The iron ions and electrons migrate outwards through the wustite layer via iron vacancies and electron holes, respectively. At the FeO-Fe₃O₄ interface, the magnetite is reduced by iron ions and electrons as shown in equation 2.53.



Iron ions and electron surplus from this reaction proceed outward through the magnetite layer, and at the Fe₃O₄-Fe₂O₃ interface, magnetite is formed according to:



the value of n is 2 or 3 for Fe²⁺ and Fe³⁺ respectively.

If iron ions are mobile in Fe₂O₃ phase, they will migrate along with electrons over iron ion vacancies and new hematite will form at the Fe₂O₃/gas interface according to equation 2.55



At this interface, oxygen also ionises according to the equation 2.56.



2 Technical background and literature review

On the other hand, if oxygen ions are mobile in the hematite layer, the iron ions and electrons, in excess of requirements for reduction of hematite to magnetite, will react with oxygen ions diffusing inwards through the hematite layer via oxygen vacancies forming new Fe_2O_3 according to:



The corresponding electrons then migrate outwards through the Fe_2O_3 to take part in the ionisation at the Fe_2O_3 /gas interface.

The addition of Cr into Fe is well known for having a significant effect in improving the oxidation resistance at high temperatures. The formation of a continuous Cr_2O_3 scale on Fe-Cr alloys leads to a decrease in the oxidation rate. Though Cr_2O_3 is the most stable oxide that can form on Fe-Cr alloys, iron oxides are growing at much faster rate as discussed earlier. For protective behaviour to occur, the initially formed, faster growing oxides have to be undercut by a chromia layer. In order to produce a complete layer of Cr_2O_3 , a certain minimum volume fraction and therefore a certain minimum of chromium flux is required.

2.3.2 Oxidation of Fe-Cr alloying system

The oxidation kinetics and the morphology of the scale produced during the oxidation of Fe-Cr alloys have been the subject of numerous papers in past years [78-82]. For normal oxidation (when the partial pressure of oxygen in the system is greater than the equilibrium dissociation pressure of all possible oxides) the phase diagram has been found to give a good description of the oxidation behaviour of Fe-Cr alloys. During oxidation at 1000°C Fe-Cr alloys containing less than 13wt.% Cr produce scales which consist of outer layers of Fe_2O_3 and Fe_3O_4 and an inner layer whose composition is best described by $Fe_{(3-x)}Cr_xO_4$. Croll and Wallwork [83] constructed the iron-chromium-oxygen equilibrium diagram at 1000°C and showed that if the chromium concentration in the alloy is very low (0.2wt.% Cr), FeO doped with chromium is the stable oxide phase in contact with the alloy instead of the iron-chromium spinel. This is shown in Fig. 2.3.3.

2 Technical background and literature review

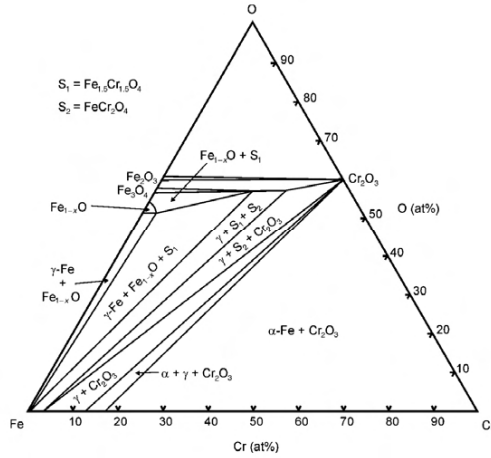


Fig. 2.3.3: Isothermal section of Fe-Cr-O phase diagram at 1000°C of several binary Fe-Cr alloys [83].

The scales formed on the alloys with chromium contents in the range 14-20wt.% are quite complex. Since the bulk concentration of chromium is in excess of the value needed for Cr_2O_3 stability as an external layer, this phase first forms overlaid with iron-rich oxides due to internal oxidation effects. The subsequent depletion of the chromium from the alloy may be sufficient to lower the chromium concentration in the alloy at the alloy-scale interface to below 13wt.%, in which case internal oxidation of chromium occurs and iron enters the scale in high quantities. The resulting stratified scale consists of outer layers of Fe_2O_3 and Fe_3O_4 with an inner layer of $FeFe_{(2-x)}Cr_xO_4$. There is a change in the kinetics from parabolic to linear growth rate. Subsequently, the kinetics may again follow a parabolic growth rate if a self-healing Cr_2O_3 layer doped with iron forms at the base of the scale [84]. A chromium oxide scale, most often overlaid with a thin iron-rich oxide layer, forms on Fe-Cr alloy containing greater than 20-25wt.% Cr with the exact composition depending on the experimental conditions. Howes [85] has obtained the direct evidence of void formation at the alloy-scale interface during oxidation of these alloys. This verifies that the outward diffusion of chromium is involved in the oxidation mechanism for Fe-Cr alloys of high Cr-content.

Footner et al. [86] examined the kinetics of oxidation of Fe-Cr alloys, in the 0-50wt.% Cr range. As shown in Fig. 2.3.4, the initial addition of Cr to iron results in a large reduction in the rate of reaction due to the elimination of the wustite phase as a scale component and the progressive appearance of chromium-rich oxides.

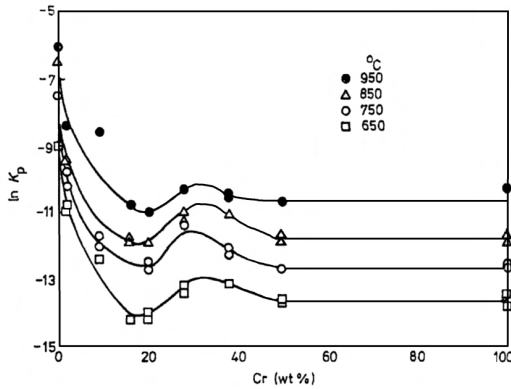


Fig. 2.3.4: Parabolic rate constants of Fe-Cr alloys at various temperatures according to Footner et al. [86].

There is a minimum oxidation rate at each temperature at about 20wt.% Cr and maximum at about 30wt.% Cr accompanied by a slight decrease in the oxidation rate as the chromium content in the alloy is further increased. The minimum oxidation rate at about 20wt.% Cr is considered to be due to the increased amount of Fe_2O_3 in the Cr_2O_3 scale decreasing the diffusion rates in the scale as the oxide is transformed from p-type Cr_2O_3 to n-type Fe_2O_3 . The iron content of the scale is measured, although no comment on the spatial distribution of the iron in the scale was made. It was shown that the minimum oxidation rate corresponded to an iron concentration in the scale sufficient to transform it from p-type to n-type semiconductor. The electron microprobe analysis of the Cr_2O_3 scale formed on the Fe-Cr alloys supports the suggestion that Fe enters the scale only in the initial stages of oxidation. It was considered near the scale-alloy interface and the concentration decreased with increasing time. It can be concluded from the existing literature that the oxidation rate decreases with increasing chromium content, and increases with increasing temperature. Together with chromium depletion underneath the alloy surface, three kinds of oxide layer growth on the specimens were observed: wustite, a spinel with composition between Fe_3O_4 and FeCr_2O_4 , and a rhombohedral solid solution with a composition between Fe_2O_3 and Cr_2O_3 . The effect of Cr in the oxidation reaction can be concluded as

- (1) Reducing the wustite growth rate by decreasing its range of stability and elimination of wustite as a reaction product if enough chromium is present

2 Technical background and literature review

- (2) Slowing the M_3O_4 growth rate by forming $FeCr_2O_4$ rather than Fe_3O_4 . This effect is smaller than the effect on FeO growth rate
- (3) Elimination of spinel as stable phase if the chromium content is high enough
- (4) When the chromium content is too high for a spinel formation, or when the spinel approaches the $FeCr_2O_4$ composition, the rhombohedral layer may exhibit a modified growth rate as a result of increasing its chromium content

Diffusion and transport mechanisms in oxide scales grown on Fe-Cr alloys

Spinel of the system Cr-Fe-O are of high technological importance in the steel industry as well as of basic scientific interest. The knowledge of the stability ranges of different phases occurring in the Fe-Cr-O system is critical for improvement of the oxidation resistance of alloys. According to the theory of oxidation of Wagner [40, 41], one would expect that diffusion rates should be low in metal oxides of low electrical conductivity. For the oxide $Fe_{3-\delta}O_4$ an end member of the solid solution $(Cr_x Fe_{1-x})_{3-\delta}O_4$, data on the deviation from the stoichiometry and on the influence of the non-stoichiometry on defect related properties such as the electrical conductivity and the diffusivities of cations are well established [87, 88]. The basic findings shown to be valid for magnetite are also expected to hold for the spinel solid solution, i.e., that the cation vacancies and the cation interstitials are the majority defects. The cation vacancies may occur on the octahedral and on the tetrahedral cation sites. Fe ions may occur as Fe^{2+} and Fe^{3+} ions while Cr ions are most likely as Cr^{3+} ions and interstitial ions may occur in three different sites, an octahedral and two tetrahedral ones, the latter different from each other with regard to the next nearest neighbor coordination. Therefore, the overall concentration of the cation vacancies consists of two terms and the concentration of the cation interstitials contains nine different terms. The nomenclature used in the following equations is given below.

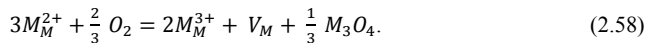
M_M M atom on M site

M_I M atom on interstitial site

V_M Vacancy on M site

V_I Vacant interstitial site

The formation of the cation vacancies may be described by the following equation



2 Technical background and literature review

Calculating the equilibrium constant for the above equation, the vacancy concentration can be expressed as

$$[V_M] = \frac{K_V}{4} \cdot a_{O_2}^{\frac{2}{3}} = [V]^0 \cdot a_{O_2}^{\frac{2}{3}}. \quad (2.59)$$

Where $[V]^0$ is a defect constant and K_V is the equilibrium constant for the vacancy formation. The rectangular brackets denote concentrations per lattice molecule. The cation interstitials are formed via Frenkel defect equilibria:

$$M_M^{n+} + V_I = M_I^{n+} + V_M. \quad (2.60)$$

Replacing the vacancy concentration in the formulation of the law of mass action for equation 2.60 by equation 2.59 leads to an oxygen activity dependence on the interstitial concentration of the form

$$[M_I^{n+}] = 4K_I \cdot a_{O_2}^{-\frac{2}{3}} = [I]^0 \cdot a_{O_2}^{-\frac{2}{3}}. \quad (2.61)$$

Where K_I is the equilibrium constant for the interstitial formation. Taking into account both defect formation reactions and neglecting the concentration of anionic defects, the deviation from stoichiometry, δ , can be written as

$$\delta = [V_M] - [M_I^{n+}]. \quad (2.62)$$

Replacing the concentrations of the cation vacancies and interstitials by equations 2.59 and 2.61 results in oxygen activity dependence of the form

$$\delta = [V]^0 \cdot a_{O_2}^{\frac{2}{3}} - [I]^0 \cdot a_{O_2}^{-\frac{2}{3}}. \quad (2.63)$$

Töpfer et al. [89] studied the influence of x on the deviation from the stoichiometry in $(Cr_x Fe_{1-x})_{3-\delta} O_4$ and showed that at higher oxygen partial pressures cation vacancies are dominant and at lower oxygen activities cation interstitials are the majority point defects. They have studied the variation in the stoichiometry at 1200°C by changing x from 0 to 0.5 and found that as the amount of Cr increases in the spinel deviation in the level of stoichiometry decreases. The diffusion coefficients of Fe, Cr were also measured in the spinels by varying the Cr concentrations in the spinel. It was found that as the Cr- concentration increases in the spinel, the diffusivity of Fe and Cr decreased.

Chromia and chromium rich oxides form protective scales on a large number of high temperature alloys. Non-stoichiometry in Cr_2O_3 is very small and no reliable data has been

2 Technical background and literature review

reported for temperatures below 1200°C [26, 90]. At high temperatures around 1000°C-1200°C depending on the purity of the chromia, the oxide is an intrinsic electronic conductor [91, 92]. At lower temperatures it is an extrinsic conductor. Self diffusion of Cr in Cr₂O₃ was studied by several authors [93-96]. The results indicate that the dominant defects in Cr₂O₃ are changed with oxygen partial pressure. At higher oxygen partial pressures chromium vacancies and at lower pressures chromium interstitials dominate. The diffusion coefficient of Cr measured at 1100°C in Cr₂O₃ is nearly 10⁻¹⁷ cm²/s. At the same time the oxygen diffusion coefficient is also found to be in the range of 10⁻¹⁷ cm²/s. The reason for the slower diffusion in Cr₂O₃ layer is due to the predominant electronic equilibrium. If predominant point defects in Cr₂O₃ are triply charged vacancies, the formation of these vacancies can be expressed by the reaction 2.64.



Taking the electroneutrality condition $h = 3[V_{Cr}''']$ into account, where brackets indicate concentration in mole fraction per mole of Cr₂O₃, the equilibrium concentration of chromium vacancies is given by

$$[V_{Cr}'''] = \left(\frac{K}{27}\right)^{\frac{1}{4}} p_{O_2}^{\frac{3}{16}}. \quad (2.65)$$

From a similar consideration for triply charged interstitial defects, the concentration of chromium interstitials $[Cr_i''']$ is proportional to $p_{O_2}^{-\frac{3}{16}}$. If the predominant defects for self diffusion of Cr is either a triply charged interstitial or a triply charged vacancy, the diffusivity at a given temperature is proportional to either $p_{O_2}^{-\frac{3}{16}}$ or $p_{O_2}^{\frac{3}{16}}$ [93]. This indicates the change of defect structure of the chromium oxide layer with changing oxygen pressure.

To understand the effect of a chromia layer on the corrosion process, not only the diffusivities of chromium and oxygen in the Cr₂O₃ layer are of interest, but also the diffusion of alien atoms is important. The outward diffusion of cations such as Fe, Ni and Mn from the alloy through the chromia layer plays a role in the growth of the outer spinel layer in the oxidation of high-alloy steels at high oxygen pressures. Lobnig et al. [97] experimentally calculated the diffusion coefficients of Fe, Ni, Cr and Mn in chromia layers grown on the model alloys Fe-20Cr and Fe-20Cr-12Ni at 900°C. They found that the lattice diffusivity of Mn is about two orders of magnitude higher than the other lattice diffusion coefficients. The diffusion coefficients for Cr, Fe, and Ni are in the same range and equal to about 10⁻¹⁶ cm²/s. Cox

et al. [98] estimated diffusivities of different metals in Cr_2O_3 assuming that the metals diffuse as ions along Cr^{3+} lattice sites. They predicted that the diffusion coefficients should decrease in the order $D_{\text{Mn}} > D_{\text{Fe}} > D_{\text{Ni}} > D_{\text{Cr}}$.

2.3.3 Oxidation in the Fe-Cr-Ni alloying system

The oxide scales formed on these commercial austenitic steels generally comprise of spinels of the general formula $\text{M}^1\text{M}_2^2\text{O}_4$, where M^1 is Fe, Ni or Mn, M^2 is Fe or Cr, and the rhombohedral oxides of the given formula M_2O_3 where $\text{M} = \text{Fe, Cr or Mn}$ [84]. Several works have shown that the inner layers of nodules and scales contain these spinels and rhombohedral oxides, rich in iron and chromium, while the outer layers are iron rich. In completely stratified scales various combinations of the chromic oxide, FeCr_2O_4 rich in chromium, FeO , Fe_3O_4 and Fe_2O_3 may appear, from the alloy to the outer surface. Wood et al. [80] proposed a mechanism for the scale growth on nickel-chromium steels as a result of electron microprobe analyses on oxidised 18-8 stainless steel. They presumed that the initially formed Cr_2O_3 layer was a p-type semiconductor which grew by cation diffusion. Fe^{2+} and Ni^{2+} ions tend to reduce the oxidation rate by reducing the number of cation vacancies per unit volume of Cr_2O_3 . Nickel enrichment to any large extent was not observed at the alloy-oxide interface. The enrichment in most cases is proportionally larger than for iron but due to their relative proportions in the bulk alloy its effect is negligible in alloys with the nickel content almost 8wt.% in common stainless steels. Hence, iron, and to a much lesser extent nickel, enter the scale by chemical solution in the Cr_2O_3 and transport along cracks and fissures in the scale, eventually emerging to form outer layers of iron-nickel-rich oxides. At this stage the oxidation rate increases markedly and continues to do so until the specimen is completely oxidised or until a healing chromic oxide layer forms again beneath the external scale layers.

Hobby and Wood [99] showed that the commercial austenitic stainless steels are similar in their oxidation behaviour to ternary Fe-Cr-Ni alloys. However, Wood et al. and Douglas and Armijo [80, 100] reported that minor alloying elements such as manganese which promotes the formation of a spinel phase and may not be protective, and silicon, which tend to form a semi-continuous layer of SiO_2 at the base of the main scale, modify the oxidation kinetics and scale morphology. Benard [101] concluded that the influence of the addition of nickel to Fe-Cr alloy is most pronounced at a concentration of about 20wt.% Ni. The effect progressively decreases as its concentration is increased over this value. Thus, depending on

2 Technical background and literature review

the specific experimental conditions, nickel addition generally improves the oxidation resistance.

3 Materials and experimental methods

3.1 Chemical composition and microstructure of the materials

The oxidation behaviour of two ferritic martensitic steels of 9 and 12wt.% Cr and one austenitic steel of 18wt.% Cr were investigated in this work. In the following these steels will be denoted as Cr-9, Cr-12 and Cr-18 throughout the thesis. Shot-peening was applied on Cr-12 and Cr-18 steel tubes by means of ABSP as shown in Fig. 2.2.8. The chemical composition of the materials is given below in Table 3.1.1. All the three samples were cut from seamless tubes. Two ferritic martensitic steels were supplied by V&M tubes, Düsseldorf and the austenitic steel was supplied by Mannesmann DMV Stainless steel. All the three steel tubes were considered to be used as super heater tubes in power plants on behalf of the project COORE-TEC.

Table 3.1.1: Chemical composition of the materials [wt.%] used for this study.

Material	C	Al	Cu	Cr	Ni	Mo	Co	W	Nb	V	Fe
9 % Cr	0.12	-	0.09	8.63	0.18	0.38	-	1.62	0.05	0.19	Bal.
(SP) 12 % Cr	0.12	-	0.08	11.27	0.24	0.27	1.52	1.46	0.05	0.23	Bal.
(SP) 18 % Cr	0.10	-	3.01	18.64	8.83	-	-	-	0.43	-	Bal.
Alloy 617	0.07	1.14	-	21.93	54.2	8.6	11.6	-	-	-	1.0

In addition to the three steels, one Ni-based alloy 617 was studied as a model alloy for the simulation of the oxide layer formation. The alloy composition is given in the Table 3.1.1. The role of alloying elements added in the alloys can be described as follows. W, Mo and Co are primarily solid solution strengtheners. V and Nb contribute to precipitate strengthening by forming fine and coherent precipitation of carbonitrides in the ferrite matrix. Vanadium also precipitates as VN during tempering or during creep. The two elements are more effective in combination at levels of about 0.25% V and 0.05% Nb [4, 102]. Chromium contributes to solid solution strengthening as well as to oxidation and corrosion resistance. Nickel improves

3 Materials and experimental methods

the toughness but on the expense of creep strength. The partial replacement of Ni by Cu helps in stabilising the creep strength which is used in the alloy Cr-18. Co is an austenite stabiliser and is known to delay recovery on tempering of martensitic steels [33, 103]. It also promotes nucleation of finer secondary carbides on tempering.

The oxidation behaviour of all three alloys was tested at 700°C and 750°C in static laboratory air. $10 \times 10 \times 4 \text{ mm}^3$ samples were cut from the tubes. A hole of 1 mm diameter was then made (near one edge) in the sample for hanging it in the thermo-balance by means of a quartz wire. All cut samples had a slight curvature. The samples were not ground before the oxidation but oxidised in ‘as-received’ condition. The reason for this is to protect the shot-peened side from the external effects which arises during grinding and polishing. The four other flat sides were ground down to 1200 grit. The typical sample shape is shown in Fig. 3.1.1.

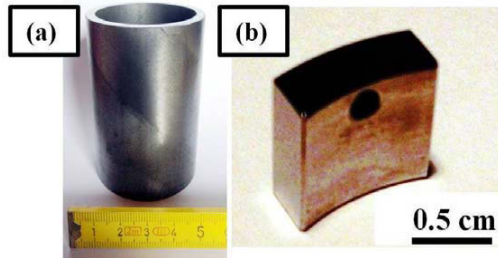


Fig. 3.1.1: Photographs of (a) boiler tube and (b) prepared sample out of the tube for thermogravimetry.

The microstructural investigation of the samples was conducted by common metallographical techniques. Firstly, the samples were ground down to 1200 grit and then subjected to polishing. Pictures taken by using the optical microscope are presented in Fig. 3.1.2.

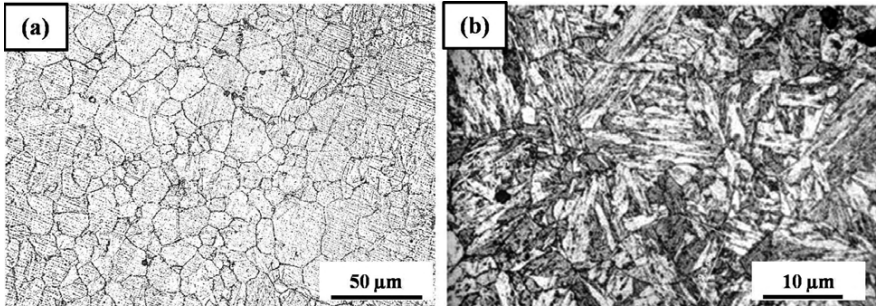


Fig. 3.1.2: Optical micrographs of the microstructures of (a) Cr-18 steel and (b) Cr-12 steel.

In Fig. 3.1.2 (a) the austenitic steel exhibits an average grain of size of $10\ \mu\text{m}$ representing the microstructure of Cr-18 and in Fig. 3.1.2 (b), martensitic Cr-12 steel with average grain sizes of $10\ \mu\text{m}$ is given.

Because of the prolonged and rather severe service conditions, it is of interest to examine the microstructural stability of power plant steels [104]. A particular important aspect of the microstructure is the presence of carbide particles. The microstructure investigation using the Transmission Electron Microscopy (TEM) was done on both steels to verify the carbides and the effect of precipitate strengthening of the two different steels. Fig. 3.1.3 (a) and (b) represent the microstructure of the Cr-12 martensitic steel in which large numbers of (Fe-Cr) carbides are present along the grain boundaries. Fig. 3.1.3 (c) and (d) shows the microstructure of the Cr-18. These micrographs show the niobium carbides precipitates on grain boundaries as identified by using EDX which drastically improves the creep strength of the austenitic stainless steel.

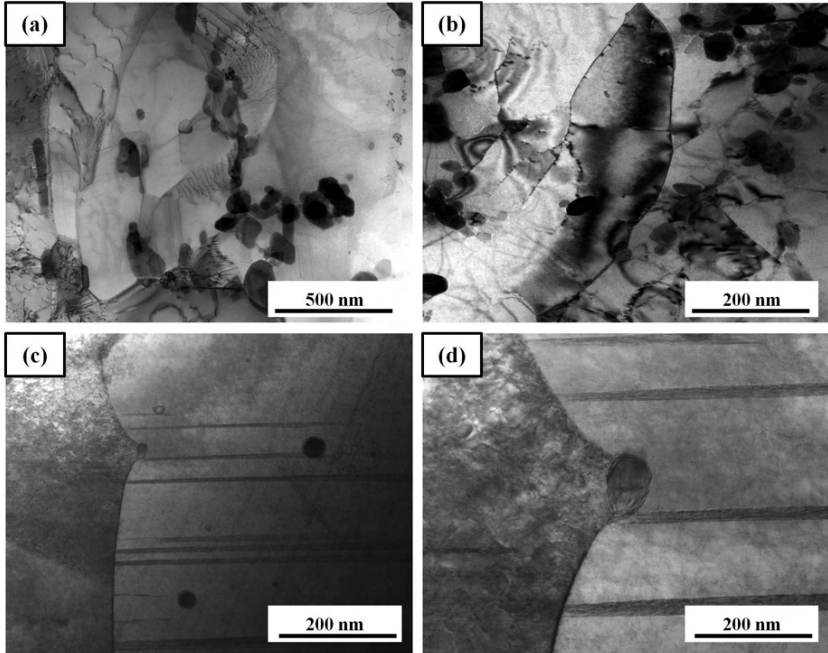


Fig. 3.1.3: Scanning Transmission Electron Microscopy (STEM) Bright Field (BF) micrographs of (a, b) Cr-12 and (c, d) Cr-18 steel.

Heat treatment

Vacuum annealing of the shot-peened samples was done in a horizontal furnace which is connected to a vacuum pump. Pre-annealing treatments were carried out in the furnace with 10^{-6} mbar vacuum at 750°C (close to working temperatures in power plants). Titanium sponges and a zirconium foil were placed near the samples during the annealing process. They are used mainly as oxygen absorbers as they have high affinity towards oxygen. During the vacuum annealing remaining oxygen in the furnace will be absorbed by these materials.

Alumina- Silica coating

Alumina-Silica paste (Ceramabond 671 consisting of 65% alumina and 35% of Potassium silicate) is mixed with diluent solution. The SP Cr-12 samples were dipped in the solution and kept in the air for drying. After the samples had been dried they were subjected to vacuum annealing. Once the annealing was finished the alumina-silica coating was removed by means of dissolving in 0.1 M NaOH solution by heating to 50°C on a heating plate. This was done at

the group of High Temperature and Functional Coatings, Deutsches Zentrum für Luft und Raumfahrt e.V, Köln.

Microhardness measurements

Microhardness measurements are required to study the influence of the shot-peening on the microstructure of the steels. A Vickers microhardness testing device (Duramin Struers) was used for all the hardness measurements in this study.

Thermogravimetry

A thermobalance consists of a sensitive balance by which a sample is hanged into a reaction chamber. Two types of thermal balances were used in this study. A SARTORIUS microbalance with a resolution of 10^{-5} g in combination with an alumina reaction tube and SiC furnace and a thermobalance of the electromagnetic type (Rubotherm) was applied in the study. The schematic of Rubotherm balance is given in Fig. 3.1.4. It works on the principle that the deflection of the permanent magnet as a result of the weight change is balanced by generating a magnetic field which in turn generates a current equivalent to the force required to bring the permanent magnet back to the original or zero position. The current required to do so is a measure of weight change and is amplified and recorded in terms of the voltage generated. The sample is located in the measuring cell and can be (un) coupled specifically (from) to the balance with a contactless magnetic suspension coupling. An electromagnet is attached to the bottom of the balance. The electromagnet, which is attached to the under floor weighing hook of the weighing cell, maintains a free suspended state of the suspension magnet via an electronic control unit. Thereby different vertical positions are possible. First the zero-point position (ZP) in which the suspension part suspends alone and contactlessly and thus represents the unburdened balance. Second measuring-point position (MP), in which the suspension part reaches a higher vertical position, thereby couples the sample to the balance and transmits the weight of the sample to balance. The principle is illustrated in Fig. 3.1.4. Prior to the thermogravimetric measurements the samples were ultrasonically cleaned in acetone, but not ground.

3 Materials and experimental methods

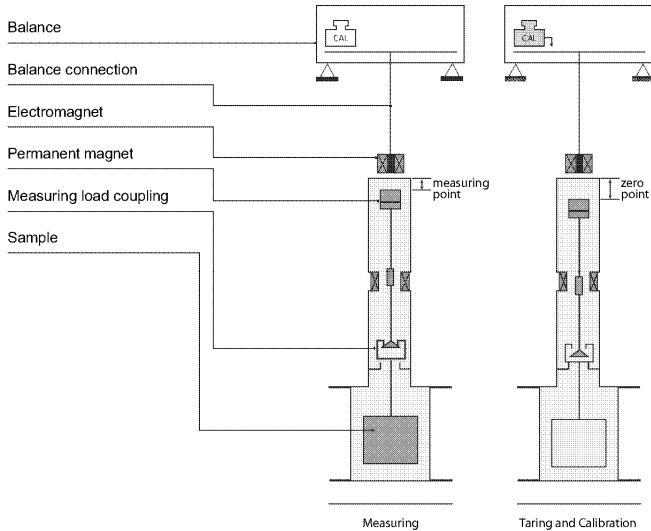


Fig. 3.1.4: Schematic representation of the Rubotherm magnetic suspension balance and the measuring principles of the balance.

For microstructural investigations of the oxidation products after oxidation exposure, the specimens were galvanically coated with Ni to protect them from oxide scale spalling during subsequent sample preparation (grinding and polishing). The specimens were embedded in epoxy and then carefully polished using diamond paste down to grit 0.3 μm .

3.2 Experimental techniques used for oxide scale characterization

In order to understand the oxidation mechanism, the following important properties of the oxide scales should be known.

- (1) Scale morphology and topography
- (2) Scale elemental composition
- (3) Identification of scale constituents
- (4) Sequence of different oxide layers formed
- (5) Segregation of oxygen or other elements at grain boundaries

All this information can be obtained by detailed analyses, using a series of optical and electron optical techniques.

3.2.1 Light microscopy

Light microscope was used in order to investigate the microstructure of the samples such as grain size and the change in the microstructure caused by shot-peening. Cr-9 and Cr-12 samples were etched using Vilella's reagent with the chemical composition of 5 ml HCl + 2 g Picric acid + 100 ml Ethyl alcohol. V₂A etchant with the composition of 100 ml water + 100 ml HCl + 100 ml of HNO₃ was used for Cr-18 samples.

3.2.2 Scanning electron microscopy

A Philips XL30 SEM instrument and an ultra-high Field Emission Scanning Electron Microscope (FESEM) by Zeiss (from the Lehrstuhl für Oberflächen- und Werkstofftechnologie, Universität Siegen) were used in this study to characterise the oxides. Both SEMs are equipped with an additional EDX detector.

3.2.3 Transmission electron microscopy

TEM is unique among all material characterisation techniques essentially enabling simultaneous examination of the microstructural features through high resolution imaging and acquisition of the chemical and the crystallographic information from a small region of the specimen. The conventional TEM operates at voltages exceeding 100-200 kV. The theoretical resolution in a TEM image approaches the wavelength of the incident electrons but it is not generally attained due to spherical and chromatic aberrations. The typical line to line resolution in a TEM is around 0.2 nm. Since the electron beam is analysed after it is transmitted through the specimen, it requires very thin substrate material. Specifically for the information on the specimens at the oxide/metal interface of a material Focused Ion Beam technique (FIB) is used to prepare the specimens. Metal/oxide interface regions were characterised using a Jeol JSM-2200FS (TEM) operated at 200 kV which is situated at the Max-Planck-Institut für Eisenforschung (MPIE), Düsseldorf.

3.2.4 Focused ion beam

The dual beam FIB/SEM system Helios Nanolab 600 (University of Siegen) and Zeiss-Crossbeam XB 1540 FIB-SEM (at Max-Planck Institute for Iron research, Düsseldorf) were used in this study to prepare the samples for the TEM investigation. These instruments are additionally equipped with an EDX detector which allowed elemental mapping on the FIB lamella which was cut from the desired sample. The Helios nanolab 600 FIB system is shown in Fig. 3.2.1.

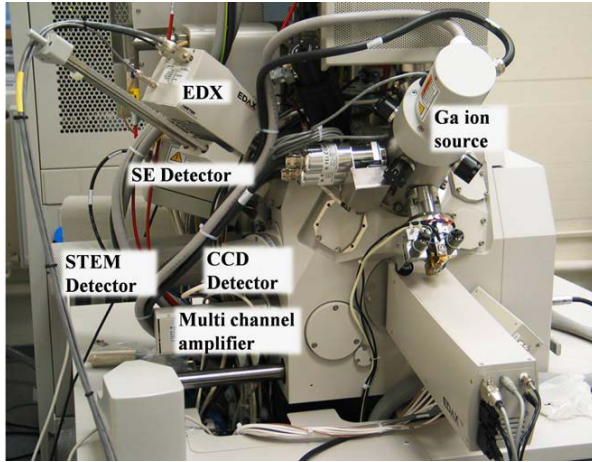


Fig. 3.2.1: Photograph of the Helios nanolab 600 FIB instrument.

3.2.5 X-ray diffraction

XRD measurements were performed in order to analyse the crystalline structure of the oxides grown on the samples upon oxidation. XRD patterns presented in this work were obtained by using a diffractometer of type PW 3040 X'Pert MPD from the company Panalytical in Bragg-Brentano geometry using Cu-K $_{\alpha}$ radiation. The working principle of a diffractometer is given by Bragg's law. In Bragg's law, the interaction between X-rays and the electrons of the atoms is visualised as a process of reflection of X-rays by atomic planes. The atomic planes are considered to be semi-transparent, allowing a part of the X-rays to pass through and reflect the other part, the incident angle θ (called Bragg angle) being equal to the reflected angle. The Bragg condition for reflection can therefore be written as

$$n\lambda = 2d \sin \theta, \quad (3.1)$$

where n is an integer and λ is the wavelength of the X- rays used.

Determination of the angles at which diffraction happens allows finding the spacing between various lattice planes and the crystal structure of the phase or phases present in a solid. Comparison of d with the experimentally obtained ICDD database for various substances (International Centre for Diffraction Data) was used to identify the phases present in the specimen.

3.2.6 Auger electron spectroscopy

Auger electrons are produced whenever incident electrons interact with an atom with an energy exceeding the energy necessary to remove an inner shell (K, L, M...) electron from an atom. The interaction or scattering process leaves the atom in an excited state with a core hole, which is a missing inner shell electron. These excited atoms are unstable and the de-excitation occurs immediately, resulting in the emission of an electron from the valance band, termed as Auger electron. Although primary excitation can be achieved by various energetic particles, most commercial equipment is made with electrons as the excitation source. Electrons with energy in the range 1-30 keV are generally used. Generation of an Auger electron requires the participation of at least 3 electrons, which therefore excludes the detection of hydrogen and helium. Auger electrons are emitted from the top 100-300 pm of the surface of the specimen. These signals are used to develop information on chemical composition from the top surface layers of the specimen. Auger electron microscope of type ErLEED 150 system from the company Omicron at the Institute für Festkörperphysik / Grenzflächen, University of Siegen, was used in this study. A maximum of 10^{-11} mbar vacuum was achieved in the system.

4 Experimental results and discussion

From the existing literature which was discussed in section 2.3, it has already been shown that at moderate temperatures the oxide scale morphology of a Fe-Cr alloying system resembles a four layer structure in which an outer oxide of Fe_2O_3 formed by the outward diffusion of Fe ions and inner layers consisting of Fe_3O_4 , FeCr_2O_4 , as well as little amounts of Cr_2O_3 due to the inner diffusion of oxygen. Adding Cr in an appropriate amount to the alloy helps in forming protective Cr_2O_3 or FeCr_2O_4 on the surface [23]. The condition of oxidation protection is fulfilled, when a compact protective oxide layer forms on the surface. Further oxidation is governed by the growth of this protective layer caused by the diffusion of ions through this layer. The protective oxides should be close to the stoichiometric composition and should have low defect concentration. One of such oxides is Cr_2O_3 , which provides the oxidation resistance to many uncoated alloys. In the following chapter the effect of Cr content on the protective nature of the oxide layers formed is studied based on the alloy compositions given in Table 3.1.1. Furthermore the oxidation mechanisms of these alloying systems will be understood and implemented in the modelling and simulation of the oxide layer growth on the boiler steels.

4.1 Influence of Cr content on the oxidation behavior

4.1.1 Results on the influence of Cr content on the oxidation behaviour

The phase diagram of the Fe-Cr-O system with varying Cr content at 750°C is illustrated in Fig. 4.1.1. The partial pressure of oxygen is varied on the ordinate and the amount of Cr is varied along the abscissa starting from 0 to 18wt.%. At higher partial pressures of oxygen, formation of Fe_2O_3 and Cr_2O_3 is possible according to thermodynamics. As the oxygen partial pressure is further decreased, a mixed oxide scale consisting of Fe_3O_4 , FeCr_2O_4 and Fe_2O_3 is formed. The formation of a Cr rich Fe-Cr spinel is observed when the oxygen partial pressure is further decreased, and at very low partial pressure of oxygen around 10^{-24} bar. Cr_2O_3 formation is again possible.

4 Experimental results and discussion

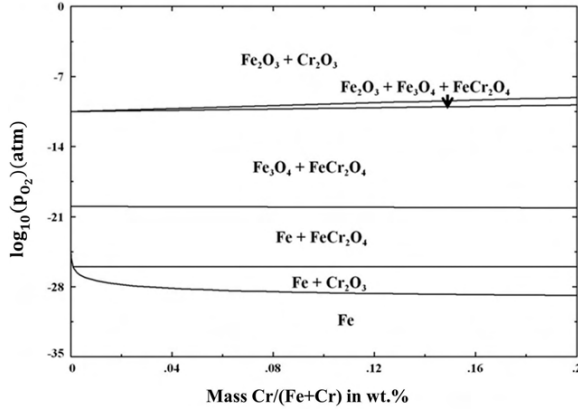


Fig. 4.1.1: Influence of Cr concentration on the phase stabilities in the Fe-Cr-O system at 750°C (calculated using FactSage).

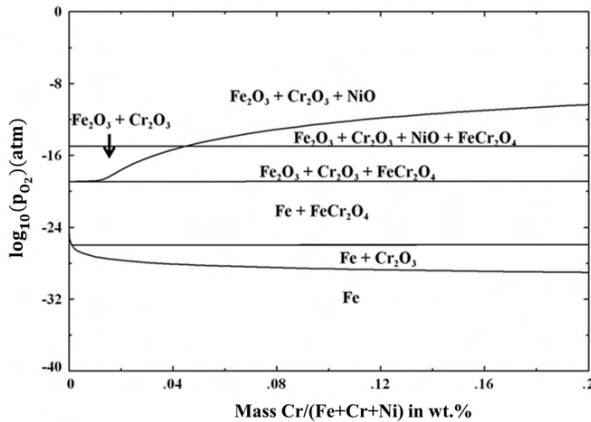


Fig. 4.1.2: Influence of Cr concentration on the phase stabilities in the Fe-Cr-Ni-O system with 8wt.% of Ni at 750°C (calculated using FactSage).

Fig. 4.1.2 represents the phase diagram of the Fe-Cr-Ni-O system at 750°C. At 18wt.% of Cr the phase composition nearly equals to the composition of the 18-8 austenitic steels. At higher partial pressures of oxygen, in addition to the Fe_2O_3 and Cr_2O_3 , NiO is also stable at this temperature according to thermodynamics. As the partial pressure is decreased, a mixture of several Fe-Ni and Fe-Cr mixed oxides forms according to the above phase diagram.

4 Experimental results and discussion

Gold marker experiments were carried out to obtain a better understanding of the mechanisms of the oxidation. Inert gold was deposited on the original metal surface of the Cr-9 sample prior to the oxidation. In case of the mechanism being dominated by inward diffusion, the marker after oxidation is located at the oxide/gas interface. It is located at the metal/oxide interface, if the scale grows by outward movement of metal ions. After oxidising the sample for 75 h at 750°C, the gold marker was found within the oxide scale. The position of the gold marker within the oxide scale as shown in Fig. 4.1.3 (a) confirms both inward diffusion of oxygen and outer diffusion of Fe, and Cr. Furthermore XRD was applied on the sample in order to analyse the oxide layer. The results are shown in Fig. 4.1.3 (b). As the depth of the X-rays for diffraction is not more than 15 μm the outer scales were analysed and found as Fe_2O_3 and Fe_3O_4 . EDX is also applied on the oxide layers of Fig. 4.1.3 (a). Combining the EDX and the XRD results, the oxide layer structure can be identified as shown in Fig. 4.1.3 (a).

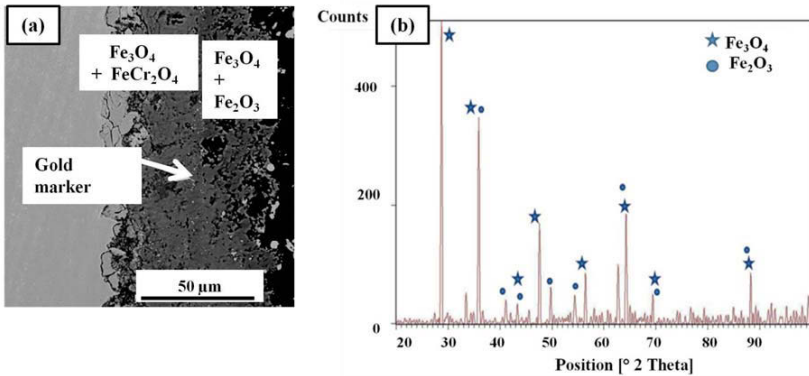


Fig. 4.1.3: (a) SEM cross-sectional morphology of gold-sputtered Cr-9 steel after oxidation at 750°C for 75 h and (b) XRD spectrum of the oxide layers formed.

After combining both EDX and XRD results of the oxide layers formed on this steel, the oxide structure can be identified as an outer layer consisting of Fe_2O_3 and Fe_3O_4 and an inner layer which consists of Fe_3O_4 and FeCr_2O_4 . Comparing the phase diagram shown in Fig. 4.1.1, the formation of oxide phases is following the thermodynamic prediction of phase stabilities, i.e., the oxide formed on the oxide/gas interface is Fe_2O_3 at higher oxygen partial pressures, and the formation of Fe-spinel and Fe-Cr spinel internally indicates the decrease of partial pressure of oxygen. However, the thermodynamic prediction of Cr_2O_3 formation at higher partial pressure, in this case at the oxide/gas interface, was not confirmed because of kinetic reasons. The kinetic aspects of oxidation could be explained on the basis of the diffu-

4 Experimental results and discussion

sion of Cr to the oxidation front to form chromium oxide on the surface which was not possible in this steel due to the little amount of Cr in the alloy matrix. From previous research it is known that adding Cr in an appropriate amount to the alloy helps in forming protective Cr_2O_3 or FeCr_2O_4 on the surface [23].

Isothermal oxidation tests were carried out for all the three alloys for 120 h at 750°C . Fig. 4.1.4 illustrates the weight change data of the steels during the oxidation tests which are used to discuss the kinetics of oxidation. The data can be fitted into the relationship $\Delta m = kt^a$, where Δm is the specific mass gain [mg/cm^2] and t is the oxidation time while k and a are constants.

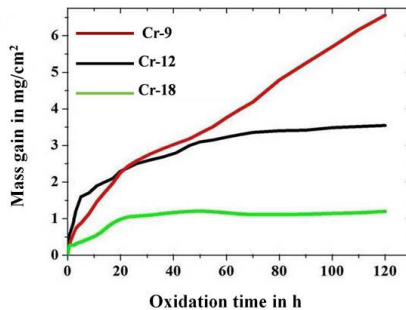


Fig. 4.1.4: Mass gain versus oxidation time for alloys studied at 750°C for 120 h.

From the Fig. 4.1.4, it is evident that the mass gain for the Cr-9 steel is higher than the mass gain for the Cr-12 steel. The Cr-18 steel exhibited the slowest oxidation kinetics. The oxidation kinetics of Cr-12 and Cr-18 steels found to be parabolic, whereas Cr-9 is exhibiting para-linear behaviour. The improvement in the oxidation behaviour increases as the Cr-content in the alloy content increases. Investigation of the oxide surfaces formed on these alloys was done by SEM. The corresponding microstructures are presented in Fig. 4.1.5.

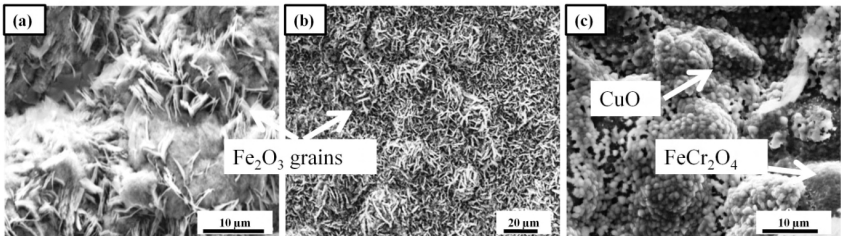


Fig. 4.1.5: SEM surface analysis of the oxides formed on (a) Cr-9, (b) Cr-12 and (c) Cr-18 steels oxidised at 750°C for 120 h.

4 Experimental results and discussion

Fig. 4.1.5 (a) and (b) document a similar oxide morphology. Some outwardly grown oxide grains (marked by arrow marks) are present on the surface. EDX spot analysis confirms that the oxide formed on the surface of both Cr-9 and Cr-12 exhibits similar oxide composition. It is confirmed as Fe_2O_3 by XRD. Phase analysis of the multiple-scale layers was done by carefully removing the layers in steps and performing separate diffraction measurements. The X-ray spectrum obtained on the surface of oxidised Cr-12 at 750°C is given in Fig. 4.1.6. The two patterns shown in Fig. 4.1.6 resemble the outer scale which comprises of Fe_2O_3 and the scale underneath the outer scale which was analysed by removing the outer scale by polishing consists of Fe_3O_4 , FeCr_2O_4 and traces of Fe_2O_3 .

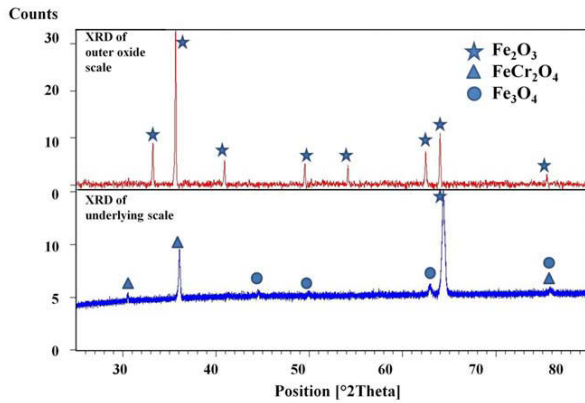


Fig. 4.1.6: XRD spectra taken on the surface of oxidised Cr-12 at 750°C . The spectrum shown on top was taken on the outer layer and the spectrum shown below was taken on the layer beneath the outer layer.

Fig. 4.1.5 shows different oxide morphologies of Cr-9, Cr-12 and Cr-18. A non-uniform porous white oxide formed at the surface on a rather continuous dark oxide. The white oxide formed on Cr-18 is confirmed as CuO whereas the dark oxide comprises FeCr_2O_4 which was confirmed by XRD. The cross-sectional analysis of all oxides formed on the three alloys was done by SEM and is presented in Fig. 4.1.7.

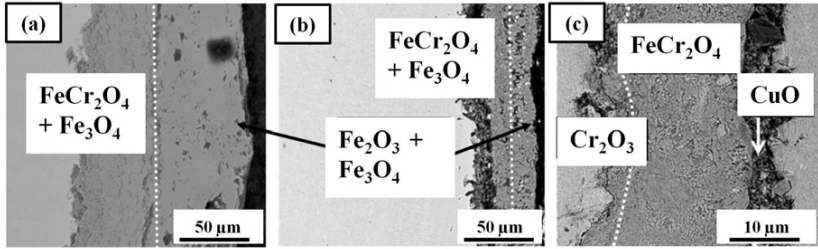


Fig. 4.1.7: SEM Cross-sectional morphologies of (a) Cr-9, (b) Cr-12 and (c) Cr-18 oxidised at 750°C for 120 h.

From Fig. 4.1.7, it is observed that the thickness of the oxide scales formed on the steels is decreasing with increasing amount of Cr in the alloy. The oxide scale morphology near the oxide/metal interface is also found to be different in the three alloys. In case of Cr-9 the total thickness of the oxide scale is about 125 μm . The thickness of the outer scale is about 70 μm which formed due to the outer diffusion of Fe. The oxide scales formed on Cr-12 is around 50 μm . In case of Cr-18 steel the thickness of the scale is found to be about 16 μm . The quantification of the elemental composition present in the oxide scales was done by using EDX line scan measurements and the results are presented in Fig. 4.1.8.

The line scans start from the innermost point where the metal/oxide interface is present and ends at the oxide/air interface. Negative x values indicate positions in the metal matrix. The results from the scans explain the enrichment or depletion of Cr near the oxide/metal interface and give direct information about the Fe/Cr ratio in the inner scales.

4 Experimental results and discussion

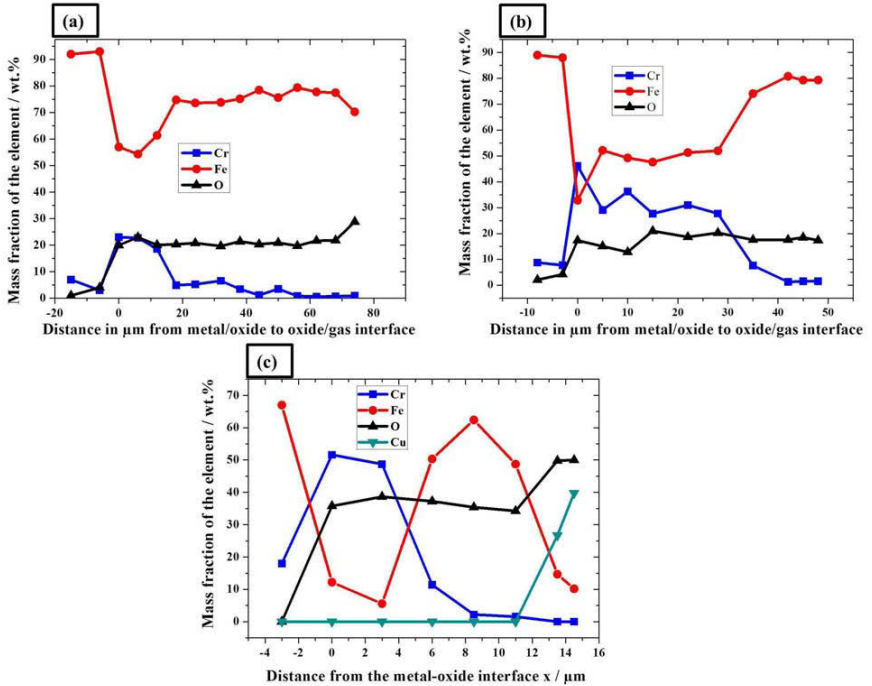


Fig. 4.1.8: EDX line scans of three different iron-chromium alloys oxidised at 750°C for 120 h. (a) Cr-9, (b) Cr-12 and (c) Cr-18.

Fig. 4.1.8 (a) gives the elemental composition of the oxide scale grown on Cr-9. Throughout the oxide scale the Fe/Cr ratio is high indicating a higher presence of Fe than Cr in the scale. The presence of Cr near the subsurface zone, i.e., in the metal matrix next to the oxidation front, indicates possible depletion of Cr near the oxidation front. The amount of Cr present in the alloy decreases to 5wt.% from the actual composition of the alloy (9wt.%) indicating that the Cr is depleted during the oxidation. The Cr presence in the outer part of the scale is almost zero. These line scan results lead to the confirmation that the outer scale is predominantly Fe-oxide and inner layer is a mixture of Fe rich Fe-Cr spinel and Fe_3O_4 .

In case of Cr-12 as shown in Fig. 4.1.8 (b), the situation is quite different. The oxide scale is grown externally as well as internally, but the presence of Cr in the internal scale is slightly higher than in the case of Cr-9. The thickness of the external scale is comparatively less than on Cr-9. This gives a significant indication that the higher presence of Cr in internally grow-

ing Fe-Cr spinel reduced the outward diffusion of Fe through the scale and resulted in a thinner outer scale. The depletion of Cr near the subsurface zone is also observed for this steel.

Fig. 4.1.8 (c) represents the line scan on Cr-18. Here, the oxide scale is thin as can be seen from Fig. 4.1.7 (c) and the scale at the oxide/gas interface consists of a Cu-rich oxide which was confirmed as CuO by XRD. Next to the CuO, an iron rich oxide is formed along with a Cr-rich Fe-Cr spinel. At the oxide/metal interface Cr is present in a very high amount possibly showing the Cr_2O_3 formation. At the subsurface zone, not much depletion in Cr is seen. At exactly the oxide/metal interface traces of Fe show possible diffusion of Fe-through the scale for the formation of the external oxide layer.

4.1.2 Discussion on the effect of Cr content on the oxidation behaviour

From the above results, it can be seen that as the Cr concentration in the alloy increases the oxidation kinetics of the alloy decreases and the amount of Cr in the Fe-Cr spinel increases. The Fe-Cr spinel formed in all these three alloys experienced a change in its composition from a Fe rich Fe-Cr spinel to Cr-rich Fe-Cr spinel. From a thermodynamical point of view of the Fe-Cr alloying system the critical Cr-concentration required to stabilise Cr_2O_3 is 0.04 at.% [23]. However, the experimental observations showed that the critical concentration is much higher [105-107]. According to a kinetic point of view, Cr at the surface tries to form a continuous protective Cr_2O_3 scale, but as it begins to form Cr_2O_3 , the surface region gets depleted of Cr at the surface [108]. If the Cr from inside does not diffuse fast enough to the surface compared to the rate of oxidation, then the oxide becomes rich in Fe. As the scale-metal interface advances, Cr_2O_3 is incorporated in the scale and transforms into spinel [84, 86]. In case of Cr-9 and Cr-12 the depletion of Cr can be explicitly seen as the outer scales are iron rich and the inner scales comprise of Fe_3O_4 and an iron rich Fe-Cr spinel. Comparing to Cr-9, Cr-12 exhibits better oxidation resistance as the Cr concentration in $(\text{Fe}_x\text{Cr}_{2-x})_{1-\delta}\text{O}_4$ is present in higher amounts. From the literature it is known that as the Cr concentration in $(\text{Fe}_x\text{Cr}_{2-x})_{1-\delta}\text{O}_4$ increases, the diffusivities of Fe and O decreases in the spinel and hence the oxide scale growth is decreased [89]. The thickness of the outer and inner scale is further reduced. The scale which is formed on Cr-18 is stoichiometric FeCr_2O_4 which is more protective as compared to $(\text{Fe}_x\text{Cr}_{2-x})_{1-\delta}\text{O}_4$. In this case the depletion of Cr is not so high but still high enough to decrease the concentration of Cr near the subsurface area suppressing a continuous Cr_2O_3 layer on the surface. From the EDX line scan shown in Fig. 4.1.8 (c) it can be stated that FeCr_2O_4

4 Experimental results and discussion

grows on top of the Cr_2O_3 layer due to the high solubility of iron in chromia permitting its outward diffusion and formation of spinel on the surface.

Concluding the above results, it can be said that when the alloys investigated form a scale under steady-state conditions, the identity of the oxide in contact with the alloy is determined by the metal composition at this interface. This composition is related to the original alloy composition and found to be critical in determining the concentration of Cr at the interface to sustain the exclusive growth of its oxide scale. The higher the concentration of Cr in the base alloy, the higher the protective nature of the oxide scales formed on these alloys. Even though the oxidation kinetics decreased with the increase of Cr in the alloy, the formation of continuous Cr_2O_3 on the surface of the alloy was not possible for the three alloys studied. However, the formation of this protective layer depends on the supply of Cr from the alloy matrix to the oxidation front. If matrix Cr does not diffuse fast enough to the surface compared to the rate of oxidation, then the oxide begins to be enriched in Fe. In the next section the main emphasis is kept on improving the diffusion behaviour of Cr to the oxidation front to form a continuous Cr_2O_3 on the surface of the alloy.

4.2 Effect of shot-peening on the oxidation behaviour

The surface finish applied to the alloys before placing them into service can affect the diffusion mechanisms of the diffusive elements and, hence, can change the oxidation kinetics of these alloys [23]. Any low temperature cold work of the surface such as machining, grinding, blast cleaning and shot-peening deforms the substrate material and introduces a large number of dislocations. As the alloy is heated, the deformed metal may recrystallise, forming a generally finer grain and a sub-grain structure. These defects are present during the transient stage of oxidation and persist for long time at low temperatures. Cr-12 and Cr-18 steels were shot-peened and the effect of shot-peening on the oxidation behaviour is studied in this section. These steels are denoted as SPCr-12 and SPCr-18 from now onwards.

4.2.1 Effect of shot-peening on the microstructure of the sample

Shot-peening causes defects and deformation near the surface hence it changes the microstructure. The dislocation density in the surface layer of shot-peened materials changes in a characteristic way with the distance from the surface and the hardness of the material [109]. However, the determination of dislocation density by means of TEM is extremely difficult.

4 Experimental results and discussion

Hardness was used as a measure of the dislocation density in this study. The hardness values of SPCr-12 and SPCr-18 are presented in Table 4.2.1. The hardness values were considerably higher near the shot-peened surface (10 μm from the surface) compared to the bulk of the alloy. The hardness values presented in Table 4.2.1 were the average values of three individual measurements taken on each side of the tube. It can be seen from Table 4.2.1, that the hardness value of SPCr-12 increases by 55 HV0.1 whereas in the case of SPCr-18 the increase is 220 HV0.1. This hardness clearly indicates the presence of dislocations near the shot-peened side [109].

Table 4.2.1: Vickers microhardness values measured on the shot-peened side and in the middle of the considered steels.

Material	Hardness (HV0.1)	Hardness (HV0.1)
	SP side	Sample core
SPCr-12 (BCC)	313	258
SPCr-18 (FCC)	420	200

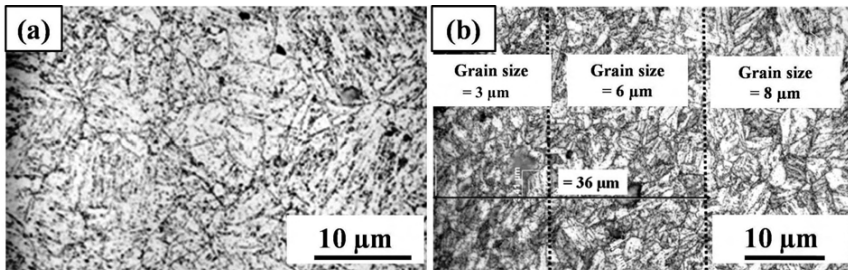


Fig. 4.2.1: Optical micrograph of the Cr-12 sample. (a) Grain structure of the core material and (b) grain structure of the SP side.

Microstructural investigation of the SP side of SPCr-12 steel was performed by using optical microscopy. Fig. 4.2.1 represents the effect of shot-peening on the grain structure. The grain size in the core of the material is found to be about 8-10 μm as can be seen in Fig. 4.2.1 (a). The presence of smaller grains near to the shot-peened side and a gradual increase of the grain size towards the bulk material validates the assumed shot-peening effect. This can be seen in Fig. 4.2.1 (b), where dotted lines are dividing the cross-section into three parts. The first part consists of grains of sizes nearly equal to 3 μm , the second part consists of grain size

4 Experimental results and discussion

of an average of $6\ \mu\text{m}$ and the third part consists of grain size nearly equal to $8\ \mu\text{m}$. The width of the first two parts is observed to be equal to $36\ \mu\text{m}$ where the effect of shot-peening is considerably effective and resulted in changing the grain size to a large extent.

The sub-surface area of the non-shot-peened side of SPCr-12 and the shot-peened side of SPCr-18 was investigated by TEM to investigate the influence of shot-peening on the oxidation behaviour. The obtained images are presented in Fig. 4.2.2. A close observation of TEM images in Fig. 4.2.2 reveals information about the presence of dislocations in non-SPCr-12 and SPCr-18, respectively. The non-SPCr-12 sample in Fig. 4.2.2 (a) shows a small dislocation density near the metal subsurface (area next to the surface). It is known that the shot-peening influences the microstructure by introducing dislocations in the affected area. TEM studies showed the high dislocation density at the subsurface of SPCr-18 as shown in Fig. 4.2.2 (b). However, quantitative data on dislocation density cannot be obtained by this measurement.

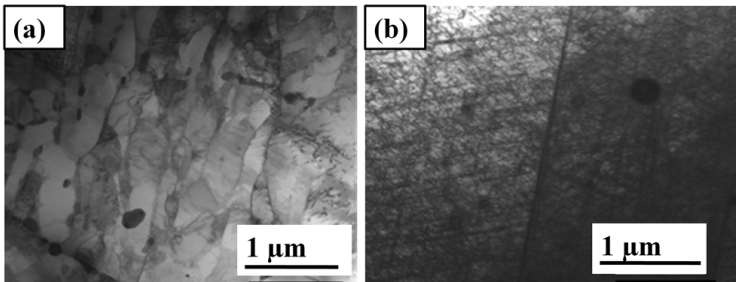


Fig. 4.2.2: STEM BF micrographs of the (a) non-SP side of SPCr-12 and (b) SP side of SPCr-18.

4.2.2 Effect of shot-peening on the oxidation behaviour of Cr-12 martensitic steel at 700°C and 750°C

4.2.2.1 Results

The SPCr-12 and non-SPCr-12 samples were oxidised at 750°C and 700°C for 75 h. The mass gains of both shot-peened and non-shot-peened steel are plotted in Fig. 4.2.3. Fig. 4.2.3 illustrates the weight change data of the steel during the oxidation test and represents the oxidation kinetics which is observed to be parabolic in nature. The parabolic rate constants calculated from the kinetic curves shown in Fig. 4.2.3 are summarised in Table 4.2.2.

4 Experimental results and discussion

In addition to the 75 h continuous isothermal oxidation tests, SPCr-12 was isothermally oxidised at 750°C for different oxidising times (20 min, 1 h, 5 h, 25 h, and 72 h) in a furnace in order to carry out time-dependent microstructure investigations. Also the non-SPCr-12 steel was oxidised at 750°C for the same oxidising times in the same furnace. The weights of the samples were measured by means of a microbalance before and after the oxidation. Discontinuous sample weight gains of both SP and non-SP samples are additionally shown as black spots on the plotted curves as given in Fig. 4.2.3.

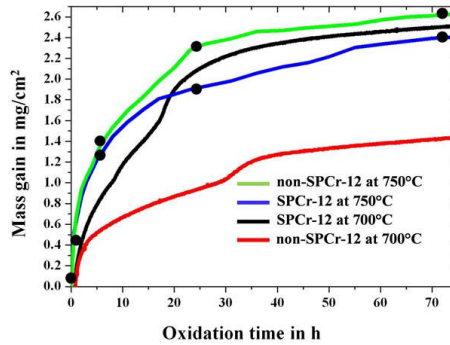


Fig. 4.2.3: Mass gain versus oxidation time for SPCr-12 and non-SPCr-12 studied at 700°C and 750°C for 75 h. Black spots on the isothermal curves indicate the superimposition of the specific mass gains of the respected samples measured after oxidising at 750°C for 20 min, 1 h, 5 h, 25 h and 72 h separately in a furnace.

Table 4.2.2: Parabolic rate constants calculated for non-SPCr-12 and SPCr-12 at both temperatures.

Material	k_p at 700°C ($\text{g}^2 \text{cm}^{-4} \text{s}^{-1}$)	k_p at 750°C ($\text{g}^2 \text{cm}^{-4} \text{s}^{-1}$)
non-SPCr-12	7.89×10^{-12}	2.64×10^{-11}
SPCr-12	2.43×10^{-11}	2.22×10^{-11}

When considering mass gain, it should be noted that this measurement is from the whole six sided sample and not just the inner shot peened surface. However, all the four flat sides were subjected to grinding prior to the oxidation procedure. Grabke et al. [110, 111], have shown that the surface finish plays an important role in the oxidation behaviour of steels. They have shown that the mass gain of the steel samples which are subjected to the surface polishing and grinding was very low compared to the non-ground and unpolished (or untreated

4 Experimental results and discussion

ed) samples. In the present experiment, it was also noticed that the oxide layer developed on the ground sides was very thin. The mass gain of these sides can be neglected in calculating the mass gain of pure shot-peened surface in extracting the shot peening effect on oxidation. The mass gain of the shot-peened surface is calculated as below. Fig. 3.1.1 shows the photograph of a sample used for the oxidation studies. The total area of the sample A was calculated by adding the areas of all the six sides. This value is used for calculating the specific mass gain of the oxidised samples and is equal to 3.55 cm^2 .

If $\left(\frac{\Delta m_{\text{non-SP}}}{A}\right)$ is the specific mass gain of the non-SP sample, then total mass gain of the non-SP sample $\Delta m_{\text{non-SP}}$ is given by equation 4.1

$$\Delta m_{\text{non-SP}} = \left(\frac{\Delta m_{\text{non-SP}}}{A}\right) \times A. \quad (4.1)$$

As per the above assumption that the mass gains of all the four flat sides is neglected, then the mass gain of a single non-SP side, $\Delta m'$, can be obtained from equation 4.2

$$\Delta m' = \left(\frac{\Delta m_{\text{non-SP}}}{2}\right). \quad (4.2)$$

If $\left(\frac{\Delta m_{\text{SP}}}{A}\right)$ is the specific mass gain of the SP sample, then total mass gain of the SP sample Δm_{SP} is given by equation 4.3

$$\Delta m_{\text{SP}} = \left(\frac{\Delta m_{\text{SP}}}{A}\right) \times A. \quad (4.3)$$

SP sample has one non-SP surface and one SP surface. Mass gain of the SP side of SP sample $\Delta m''$ is calculated in equation 4.4

$$\Delta m'' = \Delta m_{\text{SP}} - \Delta m'. \quad (4.4)$$

Specific area of the SP side and non-SP side is 1 cm^2 as these sides are 10 mm in length and 10 mm in breadth. Specific mass gains of SP side and non-SP sides are calculated in equation 4.5

$$\left(\frac{\Delta m}{A}\right)_{\text{non-SP}} = \frac{\Delta m'}{1 \text{ cm}^2} \text{ and } \left(\frac{\Delta m}{A}\right)_{\text{SP}} = \frac{\Delta m''}{1 \text{ cm}^2}. \quad (4.5)$$

Specific mass gains of the SP and non-SP sides of the SP and non-SPCr-12 samples (which are oxidised at 750°C for 75 h) from Fig. 4.2.3 are calculated using the above equations and presented below.

Total mass gain of the non-SP sample $\Delta m_{\text{non-SP}} = 2.6 \times 3.55 = 9.23 \text{ mg}$.

4 Experimental results and discussion

The mass gain of a single non-SP side, $\Delta m' = 9.23/2 = 4.61$ mg.

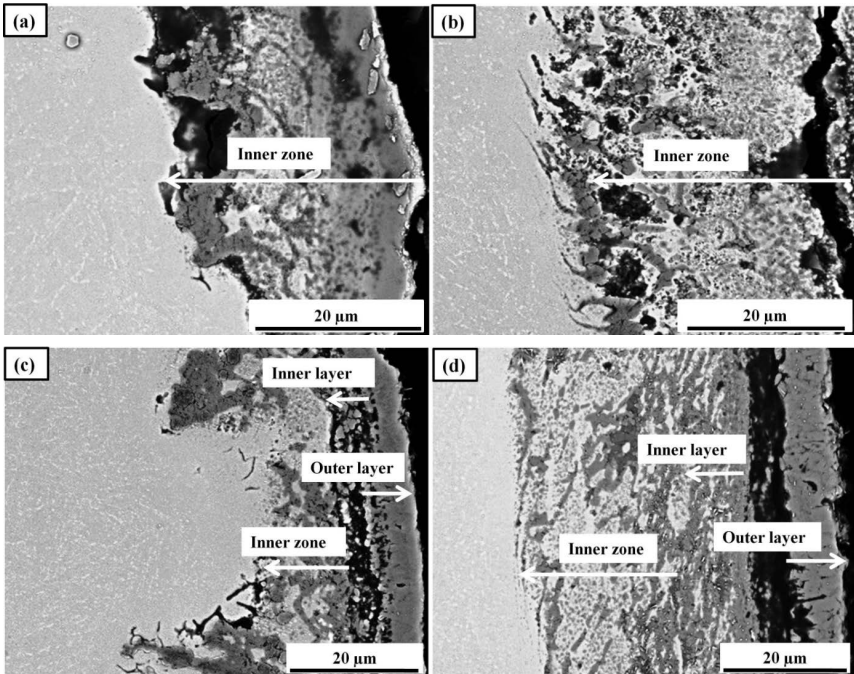
Total mass gain of the SP sample $\Delta m_{SP} = 2.4 \times 3.55 = 8.52$ mg.

Mass gain of the SP side of SP sample $\Delta m'' = 8.52 - 4.61 = 3.91$ mg.

Specific mass gain of SP side $\left(\frac{\Delta m}{A}\right)_{SP} = 3.91 \text{ mg} / 1 \text{ cm}^2 = 3.91 \text{ mg/cm}^2$.

Specific mass gain of non-SP side $\left(\frac{\Delta m}{A}\right)_{\text{non-SP}} = 4.61 \text{ mg} / 1 \text{ cm}^2 = 4.61 \text{ mg/cm}^2$.

At 700°C, values of mass gain of SP side and non-SP side are found to be 6.3 and 2.6 mg respectively. From Fig. 4.2.3, there exists clear evidence that, in the case of SPCr-12 the mass gain is low compared to non-SPCr-12 at 750°C. SEM micrographs presented in Fig. 4.2.4 (a-f) show the oxide layers formed on the SPCr-12 oxidised at 750°C for different times. The oxide layer structure formed consists mainly of three main oxides: Outwardly grown Fe_2O_3 , Fe_3O_4 and inwardly grown Fe_3O_4 , FeCr_2O_4 . Also the presence of traces of Cr_2O_3 in the case of shot-peened sample was confirmed.



4 Experimental results and discussion

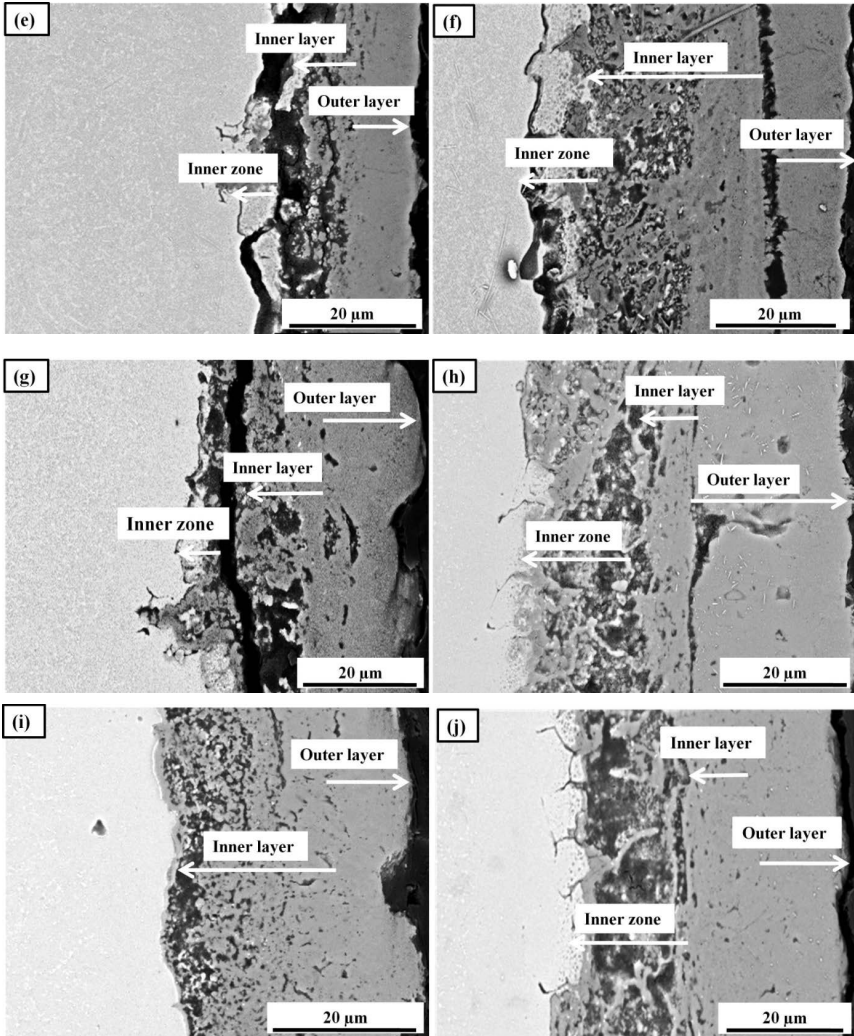


Fig. 4.2.4: Micrographs of the oxidised samples oxidised at different times of heating at 750°C (shown as black spots in Fig. 4.2.3) showing the difference in the thickness of the oxide layers between shot-peened and non-shot-peened sides, (a) SP side after 20 mins, (b) non-SP side after 20 mins, (c) SP side after 1 h, (d) non-SP side after 1 h, (e) SP side after 5 h, (f) non-SP side after 5 h, (g) SP side after 25 h, (h) non-SP side after 25 h, (i) SP side after 72 h and (j) non-SP side after 72 h. Grain boundary oxidation can also be seen in (g), (h), and (j).

4 Experimental results and discussion

An even more interesting difference between the shot-peened and non-shot-peened side is the thickness change of the oxide layers with respect to time. The corresponding results are shown in Fig. 4.2.5 (a), (b) and (c). In both cases a considerable change in the thickness of the inner zone is observed. Depending upon the oxide scale morphology the inner scale and inner zone was differentiated. The inner zone is considered when the oxide scale is not continuous and consists of uniform islands of oxide precipitates, and inner scale is considered when the oxide scale is more continuous and without any precipitates. In case of shot-peening the inner zone is present up to 25 h and from then it is gradually decreasing until it becomes very thin after 72 h. In case of the non-SP side the thickness of the inner zone is around 17 μm even after 72 h. For all oxidising times the thickness of the inner layers and inner zones is less at the SP side compared to the non-SP side. During the initial stages of oxidation, the outer scale growth in case of the non-SP side is very rapid and then the thickness of the outer scale did not change considerably. In case of the SP side the thickness of the outer scale is higher than that of the non-shot-peened one and continues to follow the parabolic growth. In non-SP side, internal layer growth is observed to be of parabolic nature.

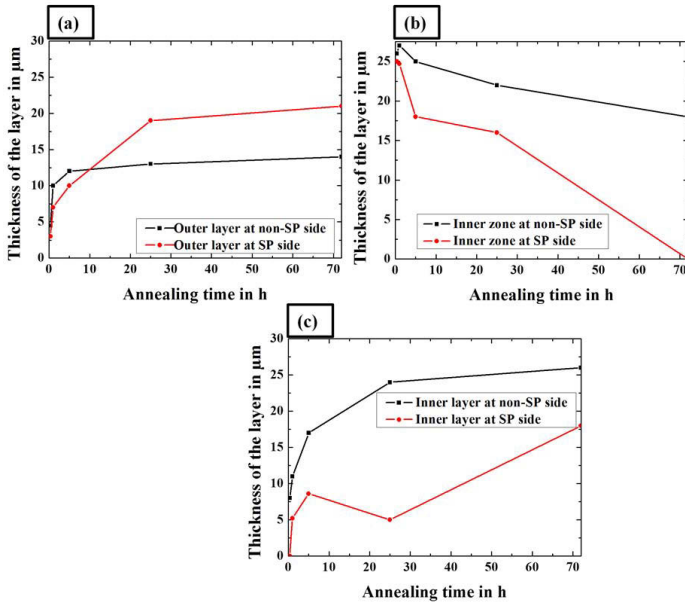


Fig. 4.2.5: Comparison of the thickness of the oxide layers of the samples at different oxidising times oxidised at 750°C. (a) comparison of outer layers, (b) comparison of inner zones and (c) comparison of inner layers.

4 Experimental results and discussion

Using FIB, the oxide layers formed on the SP side of SPCr-12 (oxidised for 75 h at 750°C) were milled layer by layer. This process is shown in Fig. 4.2.6 (a) in which different levels of oxide layers are shown. The oxide surface is shown on the right side. After removing the upper layer (consisting of hematite and magnetite), then internal layer (consisting of magnetite and Fe-Cr spinel) the situation is shown as within the oxide scale and finally the process has reached the metal interface. Fig. 4.2.6 (b) shows the oxide scale morphology of the complete oxide layers. It can be easily differentiated from the oxide grain morphology that the outer oxide contains a lamellar grain structure whereas the inner oxide exhibits equiaxial grains. A white line is drawn between the outer and inner scales as shown in Fig. 4.2.6 (b). The oxide grain morphology in the inner most and inner layers is presented in Fig. 4.2.6 (c) and (d). Presence of uniform equiaxial grains mixed with few rod-shaped grains can be pointed out in Fig. 4.2.6 (c). EDX measurements on these grains revealed that these grains are FeCr_2O_4 grains and the rod shaped grains are chromium oxide grains.

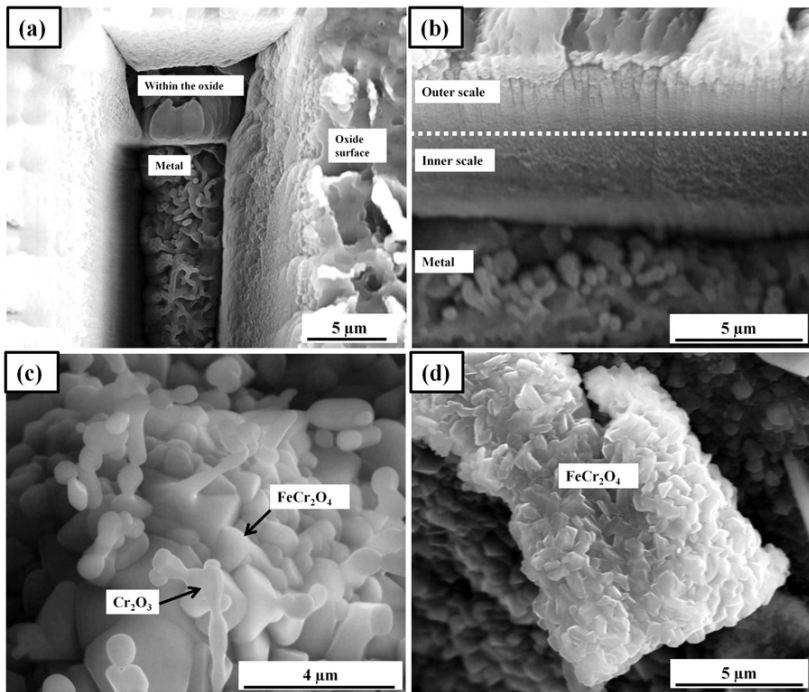


Fig. 4.2.6: (a) The surface of the oxidised SPCr-12 at 750°C, (b) cross section of the oxide layer obtained by using FIB, (c) FeCr_2O_4 mixed with small Cr_2O_3 particles inside the marked area and (d) FeCr_2O_4 .

4 Experimental results and discussion

In order to configure the presence of Cr in the FeCr_2O_4 spinel, EDX is applied on each point along a line (of SPCr-12 after 5 h of oxidation). Points and the lines are shown in Fig. 4.2.7 (c) and Fig. 4.2.7 (d), i.e., at each point, the element concentration is calculated on both SP and non-SP sides. The elemental concentration (wt.%) is plotted against the position of the points. Fig. 4.2.7 (a) and Fig. 4.2.7 (b) gives the graphical representation of the elemental distribution in the oxide scales. In Fig. 4.2.7 (a) and Fig. 4.2.7 (b) the area between the arrow marks represents the presence of FeCr_2O_4 spinel. From Fig. 4.2.7, it can be noticed that the Fe-Cr spinel formed on the SP side is rich in Cr and the spinel formed on non-SP side is rich in Fe.

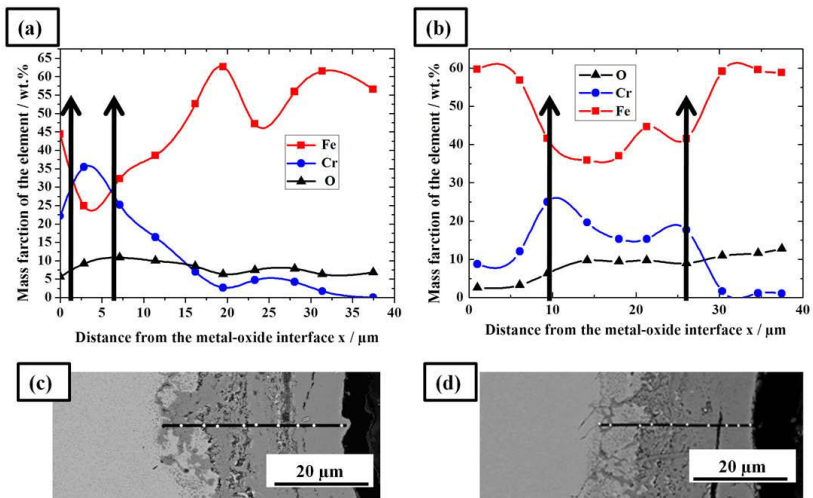


Fig. 4.2.7: Point to point EDX analysis taken on both sides of the SPCr-12 which is oxidised at 750°C for 5 h. (a) and (b) graphical representation of the analyses results (wt.%), (c) EDX point measure locations on the SP side, (d) EDX locations on the non-SP side. The area between the arrows in (a) and (b) represents Fe-Cr spinel.

The oxide scale morphology of non-SPCr-12 which was oxidised for 72 h is presented in Fig. 4.2.8. Fig. 4.2.8 (a) shows the oxide cross-section of the concave side of the sample and Fig. 4.2.8 (b) shows the oxide morphology of the convex side. Both sides were not shot-peened. The thickness of the oxide scales on the both sides is almost equal. Furthermore, the morphology is almost identical excluding some positions where localised shape effects come into act.

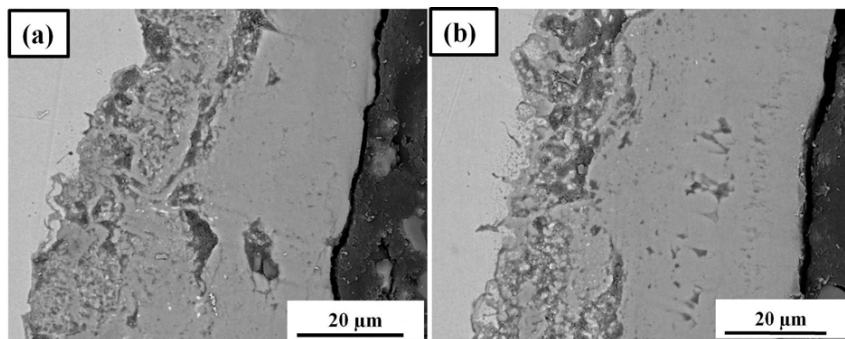


Fig. 4.2.8: SEM cross-sections of non-SPCr-12 oxidised for 72 h at 750°C, (a) concave side, (b) convex side.

By comparing the thickness of the oxide scale grown on the SP side of SPCr-12 (concave side as shown in Fig. 4.2.4 (i)) with the concave side of the non-SPCr-12 sample (see Fig. 4.2.8 (a)), a difference in the thickness of the oxide scale can be pointed out. This difference is certainly due to the effect of shot-peening on the oxidation kinetics. The higher mass gain for the non-SPCr-12, which is shown in Fig. 4.2.3 is due to the equal contribution of both convex and concave sides of the sample, whereas the low mass gain in case of SPCr-12 is due to the decrease in the oxide scale thickness on the concave side due to the effect of shot-peening.

Fig. 4.2.9 represents the oxide morphology of all oxidised specimens of Cr-12 oxidised for 75 h. From the oxide morphology, which is shown in the above Fig. 4.2.9, it is evident that the total oxide thickness in the untreated non-SP case is thicker than the oxide thickness in case of the SP sample oxidised at 750°C. Moreover, the outer oxide scale is thicker and more uniform in the non-SP case. The oxide scale in the SP case is not uniform. At some places oxide scale is thinner as shown in Fig. 4.2.9 (b) within the arrow marks. EDX line scans were taken on the oxide scales formed to quantify the composition and the presence of different species in the oxide layers that might exist due to possible differences in their diffusion behaviour. The results are presented in Fig. 4.2.10 and refer to the cross sections given in Fig. 4.2.9(b).

4 Experimental results and discussion

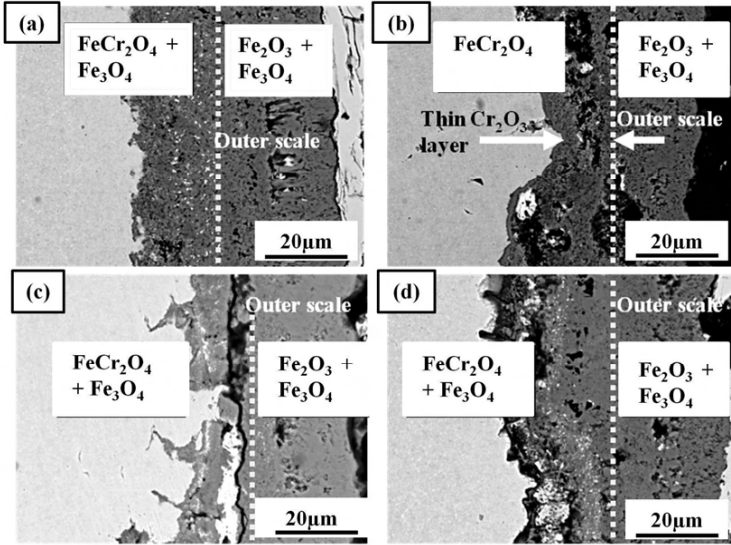


Fig. 4.2.9: SEM micrographs of the Cr-12 samples oxidised for 75 h at different temperatures showing the difference in the thickness of the oxide layers between shot-peened and non-shot-peened samples: (a) non-SP at 750°C, (b) SP at 750°C, (c) non-SP at 700°C and (d) SP at 700°C.

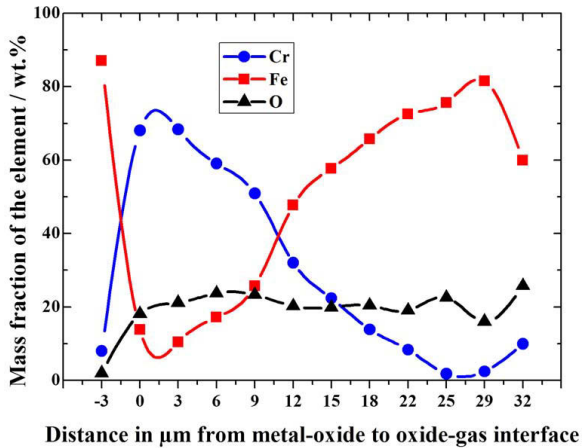


Fig. 4.2.10: Elemental line scans on the oxide scales formed at 750°C on SPCr-12 after 75 h of oxidation.

The line scan ranges from the metal/oxide interface to the oxide/air interface. In Fig. 4.2.10 the high Cr/Fe ratio in the innermost oxide scale indicates a possible Cr_2O_3 formation

4 Experimental results and discussion

on the metal/oxide interface or higher concentrations of Cr in FeCr_2O_4 . The Cr concentration decreases towards the oxide/air interface indicating the formation of Fe oxides. In Fig. 4.1.8 (b) which is the EDX scan of the oxide scale formed on non-SPCr-12, Fe is always present in higher amounts than Cr indicating that the oxide scales are rich in Fe and only small contents of Cr are present in the scale.

From the calculation shown according to equation 4.2.5, the effect of shot-peening on the oxidation behaviour of 12wt.% Cr steel was observed to be different at 700°C and 750°C. The oxide cross section morphology in case of SPCr-12 at 700°C seems to be different to the morphology of non-SPCr-12. The thickness of the oxide scale in SPCr-12 is higher than that of the non-SP case (see Fig. 4.2.9(c) & (d)).

4.2.2.2 Discussion

From the thickness measurements of the oxide scales as shown in Fig. 4.2.5, it is clear that the inner zone has considerable influence on the oxidation behaviour of non-SPCr-12 and SPCr-12. In both cases during the initial stages of oxidation the internal zone is almost of the same thickness. However, after 1 h and up to 5 h of oxidation there is a considerable drop in the thickness in case of SPCr-12. This behaviour is expected to be due to the shot-peening. Shot-peening is changing the diffusion mechanism, i.e., in case of non-SP this zone is formed due to the inner diffusion of oxygen. The solubility of oxygen in the matrix yields the formation of a precipitation zone. As the oxidation front progresses, Fe and Cr which were readily available at the oxidation front oxidise to form a continuous oxide layer. If the oxygen diffusion is faster than the oxide formation then this oxidation zone prevails for longer periods. In case of SPCr-12 the diffusion of Cr towards the oxidation front is influenced by the presence of dislocations and starts to form a Cr-rich oxide scale which prevents the internal oxidation by acting as a barrier for the oxygen diffusion. Shot-peening creates easy diffusion paths such as dislocations for Cr which in turn enhances the Cr diffusion to the metal/oxide surface [112, 113]. During heating in the initial hours, the dislocations introduced by shot-peening can serve as fast-diffusion paths, and later on grain boundaries are important for the supply of Cr and the formation of a protective oxide layer. It has already been shown by [110, 114, 115] that the use of shot-blasting on the inner surfaces of the tubes improved corrosion resistance. A network of regions created by shot-peening near the surface is supplied directly by chromium which is causing a dense and compact FeCr_2O_4 layer at the metal/oxide interface. The experimental EDX line scan results shown in Fig. 4.2.7 (a) and (b) quantify the higher presence of

4 Experimental results and discussion

Cr in the innermost oxide layer which is next to metal/oxide interface of the 5 h oxidised SPCr-12 specimen. In contrast, the oxide layers grown on non-SPCr-12 are having the high portions of iron content in the oxide scales. Accordingly to thermodynamics, an alloy consisting of 12wt.% Cr can form a Cr_2O_3 scale on the surface, but iron oxides are more stable in these atmospheres due to kinetic reasons as explained above (i.e., high availability of oxygen) and grow faster than Cr_2O_3 and $(\text{Mn, Fe})\text{Cr}_2\text{O}_4$ [110, 111]. This layer is less protective and still allows oxygen diffusion inwards and Fe cation flux outwards resulting in a Fe-rich Fe-Cr spinel next to the metal. This is reduced by shot-peening causing Cr diffusion through dislocations into the spinel and making the layer more protective against oxidation by reducing the oxygen inward diffusion and Fe-outward diffusion hindering the oxidation kinetics. However, it is known that plastic deformation causes an increase in the volume, which may also enhance the volume diffusion process. As shot-peening simultaneously increases the grain boundary density and dislocation density in the surface layer of the steel, it is not possible to identify which effect is the rate determining factor contributing to the enhancement of the Cr diffusion [112, 113, 116]. From Fig. 4.2.5, it is noticed that, as the oxidising time increases, the thickness of the oxide layers increases as well allowing establishing a clear boundary between internal and external layer. The EDX results show that the thickness of the Cr-rich Fe-Cr spinel also increases with respect to time as compared to the thickness of the spinel shown in Fig. 4.2.7 (a) and Fig. 4.2.10. That means the enhanced diffusion of Cr along dislocations continues and a Cr-rich Fe-Cr spinel continuously forms by reducing the oxidation kinetics, whereas for the non-SPCr-12 (see in Fig. 4.1.8 (b)) the Fe rich Fe-Cr spinel and a thicker outer scale formed of pure iron oxides are still being actively oxidised by allowing oxygen diffusion.

Based on the experimental observations it is clear that shot-peening the surface is changing the oxidation behaviour of the steels. However, this effect is not similar under all conditions applied. In case of martensitic Cr-12, the effect of shot-peening is observed to be different at the two temperatures studied as will be discussed in the following paragraph.

At 700°C the SP effect is found to be increasing the oxidation kinetics rather than decreasing as in case of 750°C, i.e., the SP steel is exhibiting a higher mass gain than under the non-SP condition. From Fig. 4.2.9 (c) and (d) it can be deduced that the oxide scale grown on the non-SP surface is smaller than that of the SP sample side. The morphology of the scale near the metal/oxide interface also seems to be very different. The presence of lamellar oxide grains in the SPCr-12 steel indicates the outward diffusion of Fe (see Fig. 4.2.9 (d)). This ob-

4 Experimental results and discussion

servation is in agreement with the weight gain. The thick outer scale showing lamellar Fe_2O_3 grains in case of the SP surface enable enhanced Fe diffusion causing faster scale growth. According to the kinetic point of view, Cr at the surface tries to form a continuous protective Cr_2O_3 scale, but as it begins to form Cr_2O_3 , the surface region gets depleted of Cr. If the Cr from inside does not diffuse fast enough to the surface compared to the rate of oxidation, then the oxide will begins to be rich in Fe. With an increase in temperature, diffusion and oxidation rate both increase. Depending on the activation energies, one of them shows faster kinetics than the other. The activation energy for oxidation cannot be changed easily. But the activation energy for diffusion can be decreased by adding dislocations to the surface region [117]. It can be stated that at 700°C for Cr-12 steel the thermal activation of Cr diffusion to form a subsequent Cr-rich scale, even in the presence of a dislocation density is insufficient. This means that the flux of Cr at 700°C is below the threshold which is needed to provide a sufficient Cr supply for the Cr_2O_3 formation.

4.2.3 Effect of shot-peening on Cr-18 at 700°C and 750°C

4.2.3.1 Results

The oxidation kinetics of the SP and non-SPCr-18 steel at 700°C and 750°C is presented in Fig. 4.2.11. The parabolic rate constants calculated from the kinetic curves shown in Fig. 4.2.11 are reported in Table 4.2.3. Unlike in Cr-12 steels, the shot-peening effect is found to be similar at both temperatures in case of Cr-18 steels.

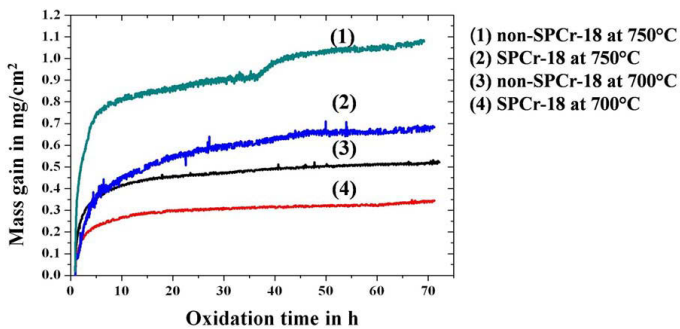


Fig. 4.2.11: Mass gain versus oxidation time for Cr-18 steel at two different temperatures.

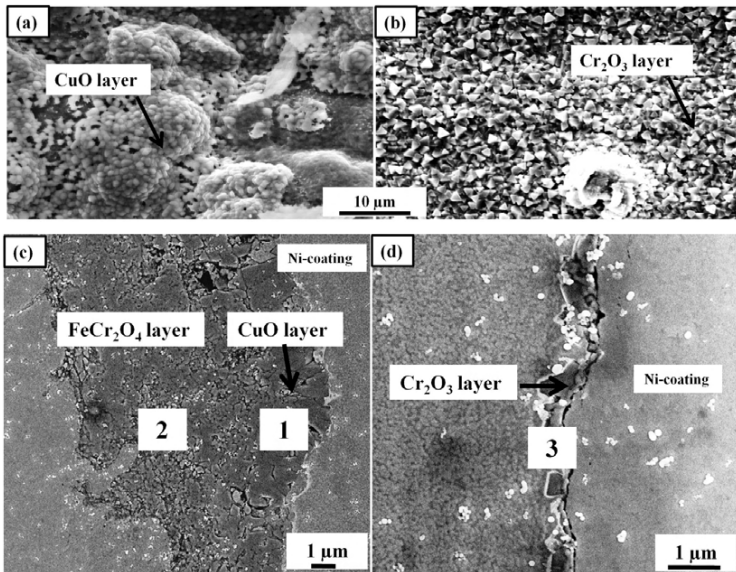
4 Experimental results and discussion

Table 4.2.3: Parabolic rate constants calculated for non-SPCr-18 and SPCr-18 at 700 and 750°C.

Material	k_p at 700°C ($\text{g}^2 \text{cm}^{-4} \text{s}^{-1}$)	k_p at 750°C ($\text{g}^2 \text{cm}^{-4} \text{s}^{-1}$)
non-SPCr-18	1×10^{-12}	4.25×10^{-12}
SPCr-18	4.29×10^{-13}	1.71×10^{-12}

Using the equations 4.1 to 4.5, the mass gains of SP and non-SP sides of Cr-18 samples are calculated. At 700°C, mass gains of SP side and non-SP sides of SPCr-18 are calculated as 0.3 mg and 0.94 mg respectively. At 750°C these values are 0.55 mg and 1.93 mg.

The parabolic rate constants shown in Table 4.2.3 indicate the decrease of the oxidation kinetics in case of shot-peened steels compared to non shot-peened steels at 700°C and 750°C, i.e., SP samples show less mass gain than the non-SP ones at both temperatures and therefore shot-peening improves the oxidation resistance. The surfaces of the oxide scales developed on both samples are shown in the SEM micrographs of Fig. 4.2.12 (a) and (b). It is clearly seen that the outer oxide scales which are formed on SP and non-SP samples are completely different. On the non-SP side non-uniform white oxide is formed on a dark oxide scale. In contrast, on the SP side uniform oxide grains are formed. Cross sectional pictures of all samples are presented in Fig. 4.2.12 (c)-(h).



4 Experimental results and discussion

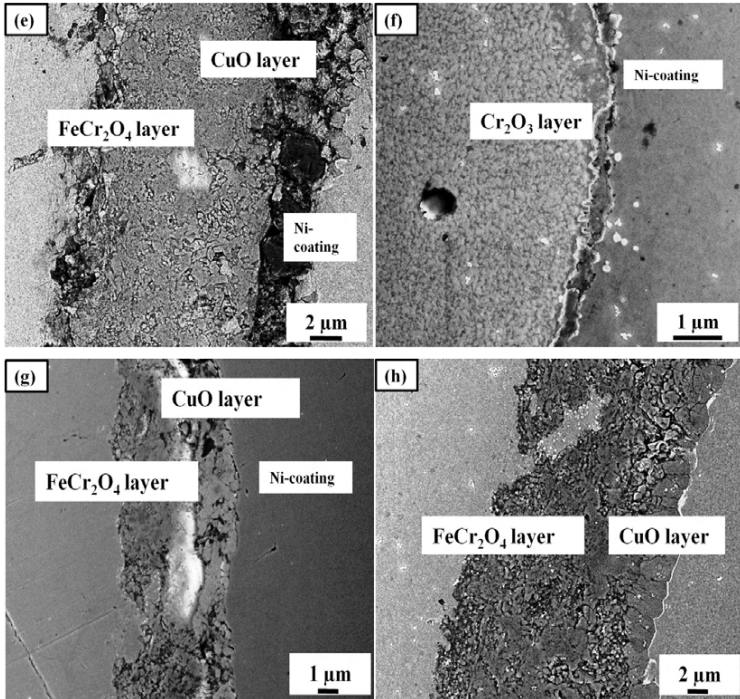


Fig. 4.2.12: The oxide scale morphology of the austenitic steel studied: (a) oxide surface of the non-SP side of SPCr-18 oxidised at 750°C for 72 h, (b) oxide surface of the SP side of SPCr-18 oxidised at 750°C for 72 h, (c) cross-section of the non-SP side of SPCr-18 oxidised at 700°C, (d) cross-section of the SP side of SPCr-18 oxidised at 700°C, (e) cross-section of the non-SP side of SPCr-18 oxidised at 750°C, (f) cross-section of the SP side of SPCr-18 oxidised at 750°C, (g) cross-section of the non-SP side of SPCr-18 oxidised at 700°C and (h) cross-section of the non-SP side of SPCr-18 oxidised at 750°C.

EDX spot analyses were carried out on the oxide scales formed. The results are presented in Fig. 4.2.13. The EDX spectra reveal that the oxide which formed on the non-SP sample contains Cu, whereas on the SP samples it is Cr-rich.

4 Experimental results and discussion

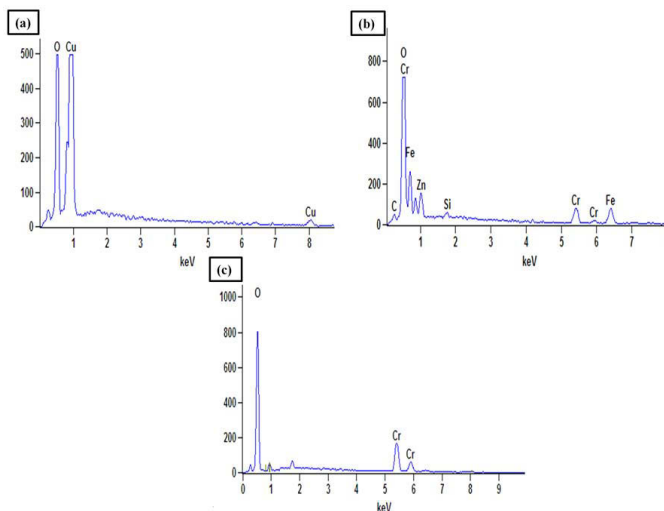


Fig. 4.2.13: EDX spot analyses (a) at point 1 in Fig. 4.2.12 (c), (b) point 2 of Fig. 4.2.12 (c) and (c) point 3 on Fig. 4.2.12 (d).

4.2.3.2 Discussion

The SPCr-18 steels exhibited a similar behaviour at both, 750°C and 700°C after shot-peening. The mass gain in both cases was smaller than that in the non-SP case. The oxide scale morphology shown in Fig. 4.2.13 (a) and (b) clearly explains the situation. A thin and almost uniform CuO layer is formed on the surface in the case of the non-SP and faceted Cr₂O₃ grains formed on the surface of the SP specimen. The cross section of the oxide layer on SPCr-18 oxidised at 700°C is shown in Fig. 4.2.12 (c) and (d). A very thin Cr₂O₃ oxide layer of about 500 nm is formed on the SP side of the SP specimen. A dual layer consisting of an outer CuO layer and an inner FeCr₂O₄ spinel layer is formed on the non-SP side of the same specimen as confirmed by the EDX spot analyses shown in Fig. 4.2.13. This spinel formation is in agreement with the literature suggested by Wallwork [84]. The difference in the oxide structure on both sides confirms the difference in the diffusion mechanisms. The enhanced Cr diffusion through dislocations introduced by the shot-peening resulted in uniform Cr₂O₃ oxide on the surface on the SP side. On the other side this enhancement is absent and instead a thicker scale grows. At 750°C similar effects are observed. The thickness of the oxide scale on the SP side was found to be about 1 μm, but on the non-SP side it is 22 μm. The

temperature increase did not influence much on the oxide thickness on the SP side, but on the non-SP side the oxide scale exhibits almost twice the thickness. The reason for this behaviour can be explained as follows. Once Cr_2O_3 is formed, then the diffusion of oxygen through this layer is very slow, and the growth of this layer depends mainly on solid state diffusion through this layer [94, 95]. This faster formation of Cr_2O_3 is promoted by the presence of dislocations [118]. Earlier studies on Fe-Cr-Ni alloy indicated that Cr leads to positive segregation with high concentrations in the grain boundaries [20, 118]. Shot-blasting also leads to a fine grain of oxide [64-66]. Moreover the large interface area and low effective activation energy of diffusion enhance Cr diffusion outwards and the oxides grow preferentially at the outer surfaces [45]. However, after longer annealing time the dislocation density can be drastically reduced by recovery or recrystallization [110], but the presence of a Cr_2O_3 layer ensures the oxidation protection.

4.3 Dislocation engineering on the shot-peened steels

4.3.1 Results

It was shown in the previous sections that shot-peening of steel prior to the oxidation does have a beneficial effect. This effect is unlikely to arise from residual stresses. Instead this effect is most likely due to the introduction of a localised plastic deformation in the near-surface region resulting in an increase of the dislocation density as shown in Fig. 4.2.2 (b). These dislocations can act as fast diffusion paths for Cr in Cr-containing steels promoting the formation of protective Cr-oxides. However, the effect of shot-peening strongly depends on factors such as working temperature and microstructure. It promotes different effects on austenitic steels and ferritic martensitic steels as shown in the previous section. The effect of shot-peening can be reversed by the annihilation of dislocations during recovery and recrystallisation of the alloy when subjected to high temperatures for long periods. Experiments presented in this section focus on the type of dislocation arrangement promoting the positive effect on the oxidation behaviour. From the previous result sections, it is known that shot-peening martensitic steels improved the oxidation behaviour at 750°C , but this improvement is not yet sufficient to replace austenitic steels [119]. The main intention of this chapter is to verify the effect of a ‘dislocation arrangement and density evolution’ on the oxidation behaviour of a low Cr martensitic steel and that of a high Cr austenitic steel. It is known that the arrangement of the dislocations evolve during recovery, polygonisation and recrystallisation processes, which take

4 Experimental results and discussion

place during annealing after plastic deformation [58]. Thus in this work the modification of the dislocation structure is controlled by an annealing treatment in vacuum after shot-peening the steel.

Hardness was used as a measure of the dislocation density in this study. The hardness values of the as-received SP steel were measured near the shot-peened surface (10 μm from the surface) and in the bulk of the material matrix. At lower temperatures and times the shot-peened samples undergo recovery. If the annealing time or temperature increases, the material recrystallises and forms new grains. These changes can be identified by the variation of the hardness values in the plastically deformed region. In order to identify the recrystallisation times for SPCr-12, the samples were pre-annealed in vacuum for 1 h, 24 h, and 62 h at a temperature of 750°C. The SPCr-18 steel samples were pre-annealed for 1 h and 24 h at the same temperature. The hardness values measured near the shot-peened surface and in the bulk of the material after annealing at 750°C for various times are given in Table 4.3.1. The increase in hardness due to shot-peening in as-received SPCr-12 steel is about 55 HV0.1. In case of SPCr-18 the hardness change is about 200 HV0.1 as can be seen from Table 4.3.1. After 24 h of pre-annealing, the samples showed a considerable decrease in hardness near the shot-peened surface. The decrease in hardness can be attributed to the recovery and recrystallisation of the previously deformed sample. In order to employ the dislocation engineering for improved oxidation resistance, the samples ideally should be in a state of recovery and should not yet be recrystallised. From Table 4.3.1, it is evident that the SPCr-12 has undergone recrystallisation after 24 h (lower hardness values than the core hardness). The oxidation studies which were planned on steels were in the state of recovery. For this reason annealing times were chosen in between 1 h and 16 h. The shot-peened Cr-12 steels were pre-annealed (before oxidation tests) for 1 h, 2 h, 3 h, 5 h and 16 h at 750°C and SPCr-18 steels were pre-annealed for 1 h, 2 h, 3 h, 4 h and 5 h.

4 Experimental results and discussion

Table 4.3.1: Hardness measurements taken on the materials studied.

Material vacuum annealed at 750°C	Time of annealing in h	Core hardness (HV0.1)	Hardness on SP edge (HV0.1)
SPCr-18 (as-received)	0	200	400
SPCr-18	1	200	355
SPCr-18	24	200	270
SPCr-12 (as-received)	0	258	313
SPCr-12	1	258	303
SPCr-12	24	258	240
SPCr-12	62	258	240

All the samples were studied regarding their oxidation resistance by continuously measuring the mass gains during oxidation annealing at 750°C. The specific mass gains of the different pre-annealed shot-peened steels are presented in Fig. 4.3.1. Pre-annealed SPCr-18 steels were oxidised for 120 h and pre-annealed SPCr-12 samples were subsequently oxidised at 750°C for 92 h. The mass gain of annealed and oxidised SPCr-18 is shown in Fig. 4.3.1 (a) and for SPCr-12 is presented in Fig. 4.3.1 (b). For comparison, the mass gains of samples in as-received condition without shot-peening (non-SP) of only Cr-12 steels are presented in Fig. 4.3.1 (b). The mass gains of non-SPCr-18 and SPCr-18 are not shown in the Fig. 4.3.1 (a) as these samples were machined in a different batch where all the other pre-annealed samples were machined in another batch. Different techniques were used in cutting, i.e., erosion cutting was used in the first batch while milling was used for the second batch. In addition to the shot-peening, these cutting methods will have an additional influence on the oxidation behaviour [110, 111]. In order to eliminate the effects due to the different preparation methods, the results from the two different batches are not shown in Fig. 4.3.1 (a).

From Fig. 4.3.1 (b) and Fig. 4.2.11 it can be noticed that shot-peening decreases the mass gain during the oxidation. In case of SPCr-18 the shot-peening decreases the mass gain almost by half while the shot-peening effect in case of SPCr-12 is considerably small. The effect of pre-annealing on SPCr-12 steels is obvious as can be seen from Fig. 4.3.1 (b). The decrease in the mass gain due to 1 h pre-annealing on SPCr-12 is almost 50% compared to the non-annealed SPCr-12. In the case of both shot-peened steels according to Fig. 4.3.1 the pre-annealing exhibits the same trends with annealing periods. Short annealing times result in

4 Experimental results and discussion

lower mass gain while longer time results in an increase in the mass gain. In case of both samples, the 1h pre-annealed SP sample has the lowest mass gain.

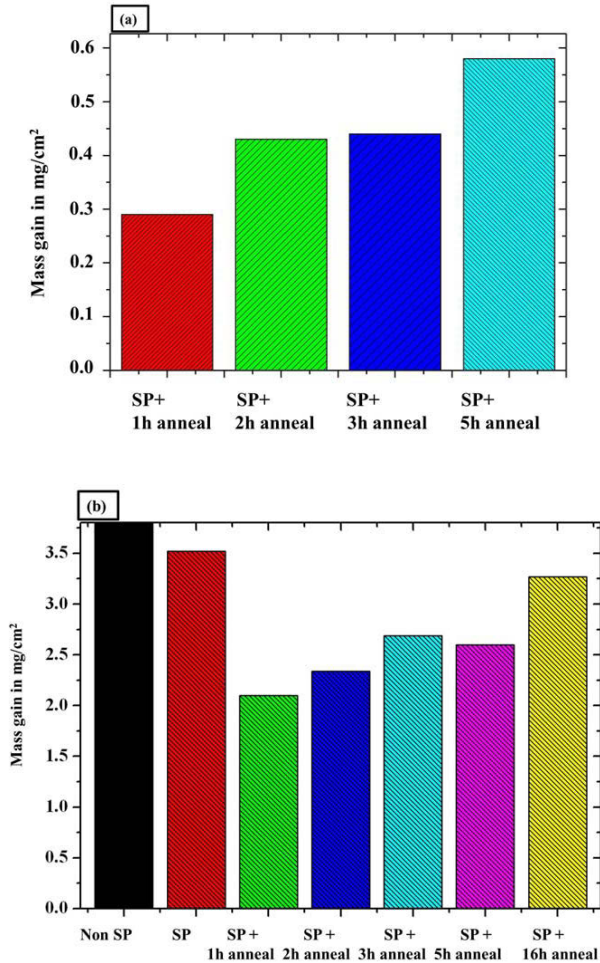


Fig. 4.3.1: Mass gain of samples exposed to shot-peening and subsequent pre-annealing treatment of (a) SPCr-18 oxidised for 120 h and (b) SPCr-12 oxidised for 92 h at 750°C.

From the mass gain values shown in Fig. 4.3.1 (b), the change in the mass gain of shot-peened surface versus pre-annealing time of SPCr-12 is calculated according to equations 4.1 to 4.5. Mass gains of the pure non-SP surface and SP surface after oxidation at 750°C for 92 h

4 Experimental results and discussion

are determined to be 6.74 mg and 6.03 mg, respectively. Table 4.3.2 shows the remaining mass gain values for all the pre-annealed samples.

Table 4.3.2: Mass gain values of SP side of SPCr-12 oxidised at 750°C for 95 h for different pre-annealing times.

Pre-annealing time, h	Total mass gain of the sample, mg	Mass gain of the pure SP side, mg
1	7.45	0.70
2	8.34	1.60
3	9.58	2.84
5	9.23	2.49
16	11.53	4.79

Even though the pre-annealing procedure was performed under high vacuum conditions, a possible pre-oxidation of the samples cannot be ruled out. In order to verify this effect, SPCr-12 samples were coated with alumina-silica mixture (a protective oxide against oxidation) and the samples were annealed for 1, 2, 3, 5 and 16 h under similar conditions. After the annealing the coating was removed and the samples were again oxidised at 750°C for 92 h. The resulting mass gains are plotted in Fig. 4.3.2.

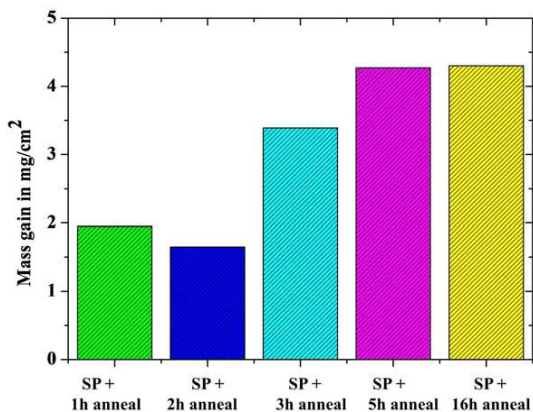


Fig. 4.3.2: Mass gains of SPCr-12 oxidised at 750°C for 92 h subjected to different pre-annealing times.

4 Experimental results and discussion

By comparing Fig. 4.3.1 (b) and Fig. 4.3.2, it can be seen that the change in the mass gain versus pre-annealing times follows similar trend, i.e., pre-annealing with and without a protective coating demonstrates the similar oxidation behaviour at the same temperature. Mass gain increases with the pre-annealing time. This behaviour once again proves that the mass change due to change in the pre-annealing times is clearly coming from the microstructural change in the subsurface of the shot-peened area but not from the pre-oxidation effects. The only difference in both cases is the least mass gain observed in case of 2 h pre-annealed SPCr-12 in the coated sample. However the values are still within the measurement error.

Another interesting observation from Fig. 4.3.1 is that the mass gain in case of SPCr-18 is lower than that of SPCr-12 under identical annealing conditions. The following micrographs were taken on the oxidised SPCr-18 which was pre-annealed for 1 h, 2 h and 5 h at 750°C. Fig. 4.3.3 shows that the oxide layer formed is chromia in all cases. The thickness is below 1 μm and varies very little. The effect of shot-peening on this steel was extensively discussed in section 4.2.3. It was shown that after oxidising non-SPCr-18 at 750°C, it acquired higher mass gain than that of SPCr-18 steel. Fig. 4.2.12 (e) shows the oxide morphology of non-SPCr-18 oxidised at 750°C and consists of an outer layer of CuO and a mixed Fe-Cr spinel. After shot-peening this steel, the oxide morphology is seen to have changed to a thin and continuous Cr_2O_3 layer formed on the surface which is shown in Fig. 4.2.12 (f). In case of pre-annealed and oxidised SPCr-18, the oxide that formed on the SP side is again Cr_2O_3 layer but the thickness varies very little as shown in Fig. 4.3.3. The pre-annealing in this case is not causing a significant change in the thickness of the oxide scale formed on the alloy, because shot-peening itself is able to change the oxide structure from Fe-Cr spinel to a continuous Cr_2O_3 layer. Pre-annealing in this case helps in a quick formation of a Cr_2O_3 layer which further reduces the oxidation kinetics.

4 Experimental results and discussion

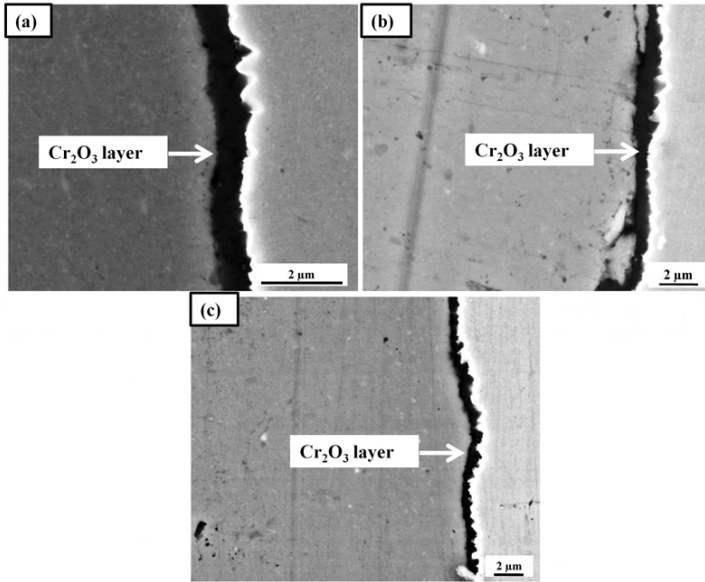


Fig. 4.3.3: SEM cross sectional images of the oxide formed on the SP sides of (a) SPCr-18 + 1 h pre-annealed, (b) SPCr-18 + 2 h pre-annealed and (c) SPCr-18 + 5 h pre-annealed, after oxidising at 750°C for 120 h.

The chemical composition at the surface of the material is very important as this determines the early oxidation mechanisms. The compositional change that occurs over a few atomic layers from the surface of the sample during the pre-annealing treatment in high vacuum was experimentally studied by using AES. The SPCr-18 sample was introduced into an ultra-high vacuum chamber which contains a pressure of 1×10^{-10} mbar. The surface chemical composition was determined by retrieving AES spectra and the results are presented in Fig. 4.3.4 (a). From the spectra it can be noticed that all the main peaks are identified as Fe and C and traces of oxygen. In a second step, the sample was heated in this chamber at 750°C for 1 h under high vacuum. The AES spectra were obtained and are presented in Fig. 4.3.4 (b). The chemical composition changed and presence of Cr can be observed on the surface. The sample was further annealed at the same temperature for 2 h and 5 h. The corresponding spectra are illustrated in Fig. 4.3.4 (c) and (d). Cr is present on the surface for both annealing times. Small impurity elements in the alloy like sulphur and potassium are also observed on the surface. The presence of Cr on the surface after 1 h pre-annealing is expected due to the diffusion of Cr towards the surface, i.e., in this case Cr is using the dislocations as fast diffusion paths.

4 Experimental results and discussion

These dislocations were present in the subsurface region of the material due to the shot-peening treatment. They provide a short circuit path for Cr to diffuse to the surface quickly by increasing the Cr content of the surface region. This enables the quick formation of Cr_2O_3 on the surface instead of Fe-oxides upon oxidation. In the SPCr-18 sample, during the initial stages of oxidation the higher concentration of Fe on the surface first allows formation of Fe-oxide and then the shot-peening effect comes into act by enhancing the Cr-diffusion to the surface, changing the oxide formation from Fe-oxides to the chromia scale.

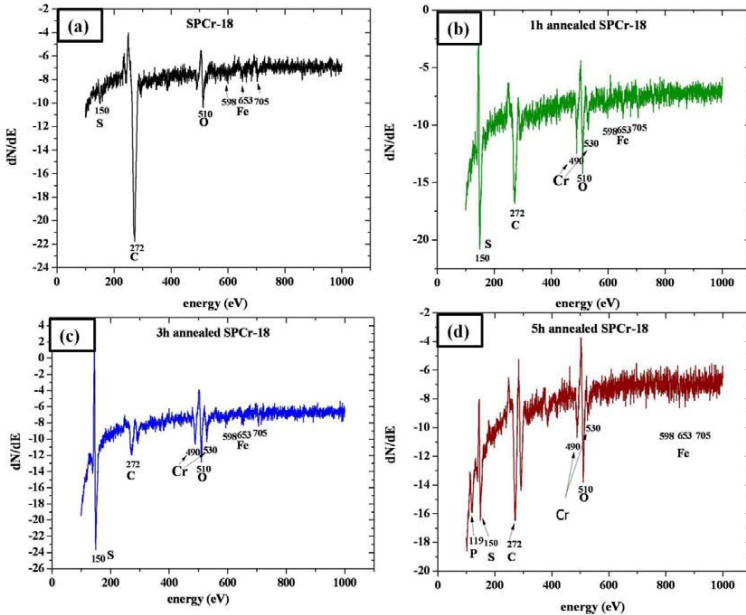


Fig. 4.3.4: Auger electron spectra on (a) surface of SPCr-18, (b) surface of SPCr-18 + 1 h pre-annealed, (c) surface of SPCr-18 + 3 h pre-annealed and (d) surface of SPCr-18 + 5 h pre-annealed.

Optical micrographs of the oxidised non-SPCr-18, SPCr-18 + 1 h pre-annealed, SPCr-18 + 2 h pre-annealed and SPCr-18 + 5 h pre-annealed specimens are presented in Fig. 4.3.5. The most important observation is the presence of a zone (shown by red arrow marks) in which grains are mixed with some dark unidentified spots. The thickness of this zone is different for the different pre-annealing conditions. In Fig. 4.3.5 (b), the thickness of the disturbed zone in case of 1h pre-annealed + SPCr-18 is higher compared to the zones present in all the other micrographs. Fig. 4.3.5 (a) is showing the SP side of SPCr-18 steel in which the thickness of

4 Experimental results and discussion

this zone is very thin. In SPCr-18 + 2 h pre-annealed and SPCr-18 + 5 h pre-annealed specimens, the thickness of this zone varies as shown in Fig. 4.3.5 (c) and (d). These black spots are not present on non- SPCr-18 as shown in Fig. 4.3.5 (e). This observation may lead to the conclusion that these black spots are present due to the microstructural change caused by the shot-peening, i.e.; the disturbed zone which thickness is changing with respect to the pre-annealing time can be linked to the change in the dislocation arrangements due to the pre-annealing times. TEM investigation is required for clarification.

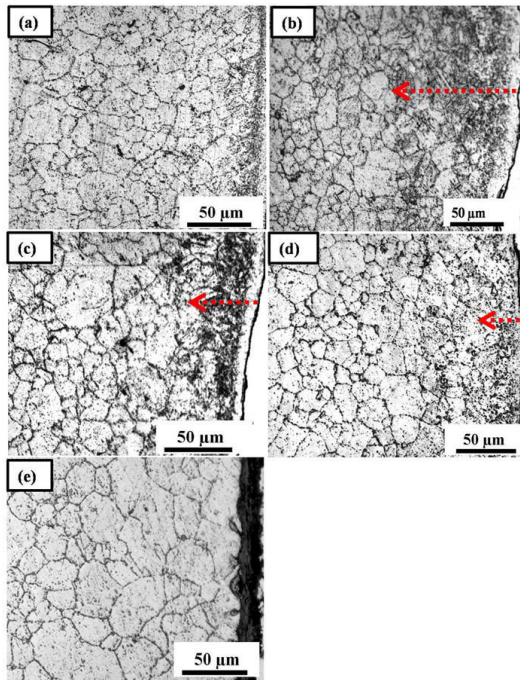


Fig. 4.3.5: Optical micrographs taken from the oxidised SPCr-18 after 120 h at 750°C: (a) SP side of SPCr-18, (b) SP side of SPCr-18 + 1 h pre-annealed, (c) SP side of SPCr-18 + 2 h pre-annealed, (d) SP side of SPCr-18 + 5 h pre-annealed and (e) non-SP side of SPCr-18.

A close investigation of the SP side of oxidised SPCr-12 + pre-annealed for different pre-annealing times was done by using SEM. The results are presented in Fig. 4.3.6. The thickness of the oxide layers formed on the SP side of the annealed SPCr-12 is smaller compared to the non-annealed SPCr-12 steel which is shown in Fig. 4.2.9 (b). Especially the thickness of the outer scale is drastically reduced. The total thickness of the oxide layers formed on

4 Experimental results and discussion

SPCr-12 + 1 h pre-annealed, SPCr-12 + 2 h pre-annealed and SPCr-12 + 5 h changed after oxidation. The smallest thickness was found in case of the 1 h pre-annealed sample with thickness gradually increasing with the pre-annealing time. This behaviour justifies the change in the total mass gain of these samples which was shown in Fig. 4.3.1 (b).

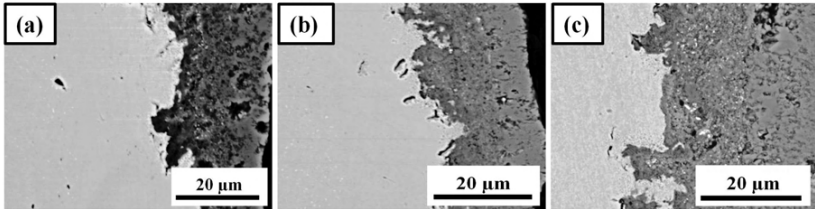


Fig. 4.3.6: SEM cross-sectional micrographs of the SP sides of (a) SPCr-12 + 1 h pre-annealed, (b) SPCr-12 + 2 h pre-annealed and (c) SPCr-12 + 5 h pre-annealed, after oxidising at 750°C for 92 h.

EDX elemental mapping was carried out on the oxide which was formed on SPCr-12 + 1 h pre-annealed after oxidising for 92 h at 750°C and results are presented in Fig. 4.3.7. The higher presence of Cr compared to Fe in the inner oxide scale can be pointed out from Fig. 4.3.7. At the positions where Cr is present in higher concentrations, almost no iron can be detected.

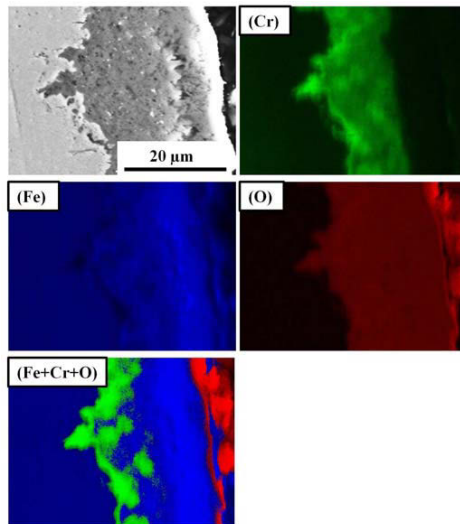


Fig. 4.3.7: EDX elemental mapping on the oxide layer formed on SPCr-12 + 1 h pre-annealed after oxidising for 92 h at 750°C.

4 Experimental results and discussion

SEM micrographs of the surface of the oxide layers formed on SPCr-12 + 5 h pre-annealed are presented in Fig. 4.3.8 (a) and (b). The observed oxide grains which grow perpendicularly to the surface represent Fe_2O_3 grains (as concluded from EDX and XRD analysis). The density of these grains is very high at the non-SP side of the specimen, while on the SP side the specimen exhibits a very small density of such grains.

The oxide scale thicknesses on both the SP and the non-SP side of the SPCr-12 + 5 h pre-annealed sample also differed as shown in Fig. 4.3.8 (c) and (d). The thickness on the SP side is smaller than that of the non-SP side.

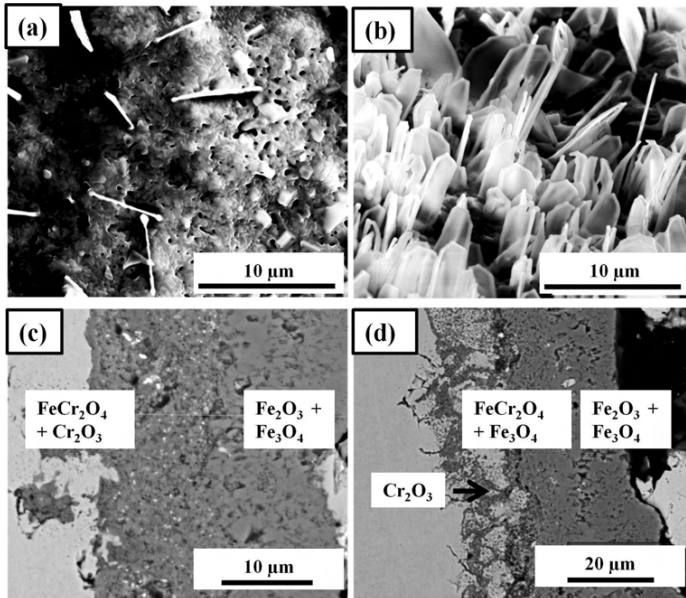


Fig. 4.3.8: SEM analysis of SPCr-12 + 5 h pre-annealed and oxidised for 92 h at 750°C showing (a) the oxide surface on SP side, (b) on the non-SP side, (c) cross-section of the SP side and (d) of the non-SP side.

In the following a detailed and more thorough analysis of the oxide/metal regimes of three example cases, namely (1) the SP region of SPCr-12 after oxidation, (2) the SP region of SPCr-12 + 5 h pre-annealed after oxidation, and (3) the non-SP region of SPCr-12 + 5 h pre-annealed after oxidation, by TEM allows better understanding of the influence of the subsurface microstructure on the oxidation behaviour of Cr-12 alloy. The samples from the region of interest were cut by using FIB and the corresponding lamellae are shown in Fig. 4.3.9.

4 Experimental results and discussion

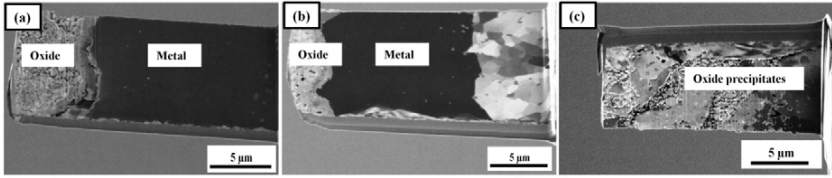


Fig. 4.3.9: FIB lamellae of (a) SP side of SPCr-12, (b) SP side of SPCr-12 + 5 h pre-annealed and (c) non-SP side of SPCr-12 + 5 h pre-annealed, which are oxidised for 92 h at 750°C.

The obvious microstructural difference of the three different lamellae is shown in the Fig. 4.3.9. Fig. 4.3.9 (a) represents the microstructure of the subsurface of the SP side of SPCr-12 after oxidation for 92 h at 750°C. The oxide layer is present on the left side of the lamella, in the centre the metal matrix is present and the right side of the lamella a light coloured cloud is present. Fig. 4.3.9 (b) illustrates the lamella of the SP side of SPCr-12 + 5 h pre-annealed sample. This lamella shows a clear difference between the oxide and the metal matrix. Fig. 4.3.9 (c) represents the lamella of the non-SP side of the SPCr-12 + 5 h pre-annealed sample. In this lamella the oxide precipitates are present throughout the metal matrix.

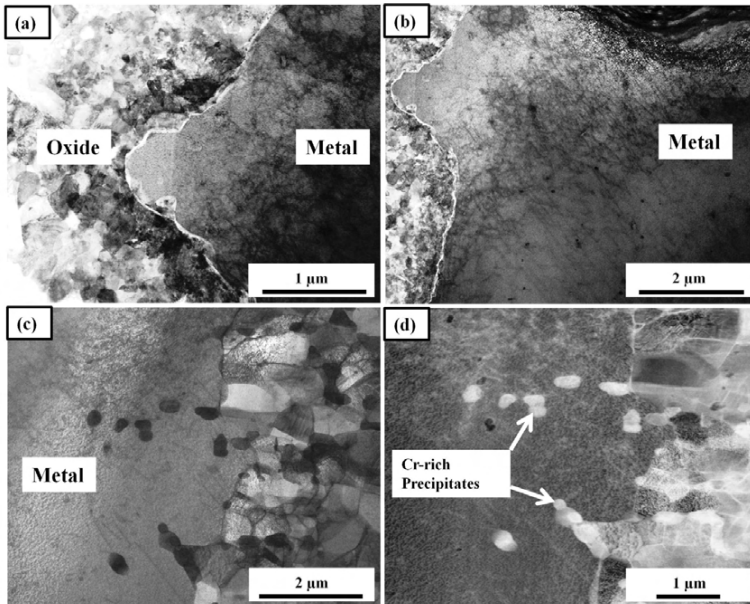


Fig. 4.3.10: STEM BF micrographs of the oxide/metal regime on (a), (b) and (c) SP side of oxidised SPCr-12 and (d) Dark Field (DF) micrograph of the interior of the SP side of oxidised SPCr-12.

4 Experimental results and discussion

TEM analysis of the three different zones of the lamella from the SP side of SPCr-12 was carried out as next step. The corresponding micrographs are presented in Fig. 4.3.10. The TEM images in Fig. 4.3.10 reveal some important observations on the sample. Fig. 4.3.10 (a) and (b) show the oxide/metal interface of the SP side of the oxidised SPCr-12 sample. The oxide is identified as a mixture of Cr-rich FeCr_2O_4 and Cr_2O_3 . The subsurface is found to be having a very small dislocation density. Fig. 4.3.10 (c) and (d) show the matrix that was not oxidised during the oxidation. The dislocation density is also very low here and the Cr-rich precipitates over the metal can also be seen as indicated by arrows in Fig. 4.3.10 (d). For more information EDX was obtained on two important regions of the oxidised SPCr-12 sample. The elemental compositions at the metal/oxide interface as shown in Fig. 4.3.11 (a) and at the interior region where some white spots were seen on the lamella as shown in Fig. 4.3.11 (b) are presented in Table 4.3.3.

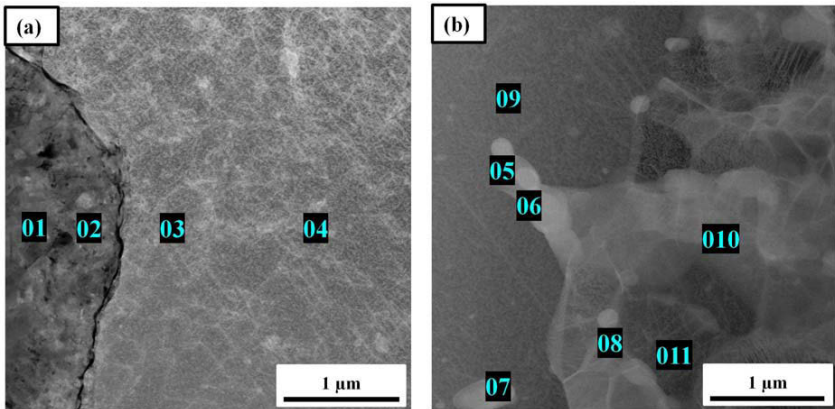


Fig. 4.3.11: EDX spot analyses of the SP side of SPCr-12 oxidised at 750°C for 120 h on (a) the oxide/metal interface and (b) on the metal far from the oxide/metal interface.

4 Experimental results and discussion

Table 4.3.3: Elemental composition acquired in at.% on Fig. 4.3.11 (a) and (b) by using EDX.

Position	O	Fe	Cr	Total
01	52.97	2.37	32.04	100
02	55.64	2.17	41.94	100
03	0.58	88.28	8.28	100
04	1.40	87.13	8.35	100
05	0	63.17	36.82	100
06	0	31.34	68.58	100
07	0	60.64	39.36	100
08	0	74	26.00	100
09	0	89.39	10.61	100
10	0	89.25	10.75	100
11	0	89.14	10.86	100

From the Table 4.3.3, it can be said that the oxide which is formed on the SP side of SPCr-12 is mainly Cr-rich Fe-Cr spinel or some discontinuous local Cr_2O_3 . A small depletion of Cr in the alloy, a few microns below the oxide scale, namely at points 03 and 04, was found. The minimum Cr content detected was 8.02wt.% reduced from the starting content of 12wt.%. The points 05 to 11 show the elemental compositions of the species within the cloud and the surrounding metal area. Point 06 represents the thickest particle in the cloud and point 09 represents the metal next to this region. The chemical composition at these points is very different from each other. The Cr concentration at point 06 is around 69% and at point 09 it is 10.61%. The Cr concentrations along the rest of the positions scatter between 10 to 40%. This means the whole subsurface can be divided into two zones where Cr is slightly depleted at the oxide/metal interface and high Cr presence is observed at the interior of the metal.

4 Experimental results and discussion

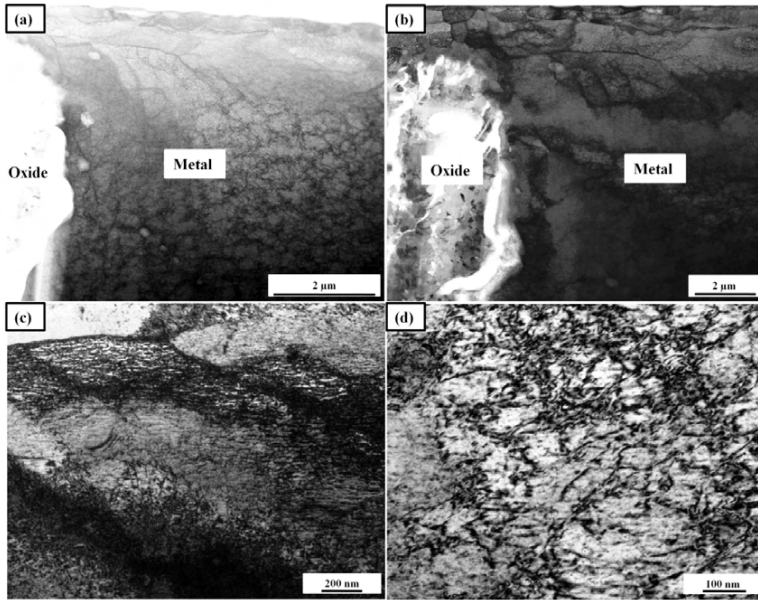


Fig. 4.3.12: STEM BF micrographs of the oxide/metal regime on (a), (b) the SP side of oxidised SPCr-12 + 5 h pre-annealed, (c) & (d) TEM micrographs of the subsurface of the SP side of oxidised SPCr-12 + 5 h pre-annealed.

The TEM investigation of the metal/oxide interface on the SP side of SPCr-12 + 5 h pre-annealed sample after 92 h of oxidation at 750°C is illustrated in Fig. 4.3.12. The left side of Fig. 4.3.12 (a) represents the oxide which is confirmed as Cr_2O_3 by diffraction measurements and elemental mapping. The subsurface consists of pure metal. From the micrographs given in Fig. 4.3.12, two major findings can be pointed out:

- (1) A high dislocation density at the oxide/ metal regime is present
- (2) The dislocations form complex networks, blocking and interacting with each other

The area in which the clusters of dislocations are present was investigated by STEM in both BF and DF, micrographs are presented in in Fig. 4.3.13.

4 Experimental results and discussion

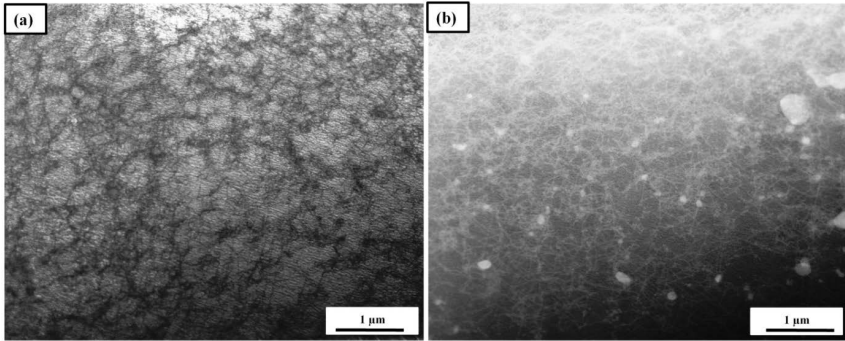


Fig. 4.3.13: (a) STEM BF micrographs of the subsurface and (b) DF images of the subsurface of the SP side of SPCr-12 + 5 h pre-annealed (oxidised for 92 h at 750°C).

Fig. 4.3.13 (a) shows the BF image of the subsurface of the SP side of oxidised SPCr-12 + 5 h pre-annealed. The DF image of the same area is shown in Fig. 4.3.13 (b). The important observation from this investigation is the uniform presence of white spots over the cluster of dislocations or a group of subboundaries. These white spots are characterised as Cr using EDX elemental analysis. These spots appear to follow a certain order through the cluster.

The TEM investigation of the metal/oxide interface on the SP side of SPCr-12 is presented in Fig. 4.3.10. After comparing this area to the SP side of the oxidised SPCr-12 + 5 h pre-annealed (see Fig. 4.3.12) a significant difference in the dislocation arrangement can be observed: the dislocation density is very low and only individual dislocations are pinned by the second phase precipitates in the matrix.

The TEM investigation on the non-SP side of the oxidised SPCr-12 + 5 h pre-annealed is illustrated in Fig. 4.3.14.

4 Experimental results and discussion

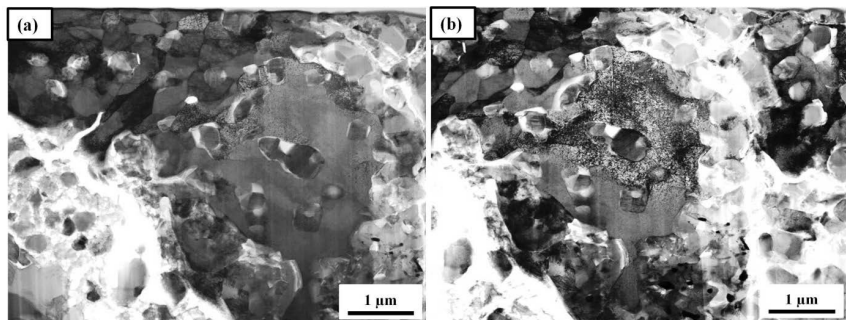


Fig. 4.3.14: (a), (b) STEM BF micrographs of the oxide/metal regime on the non-SP side of SPCr-12 + 5 h pre-annealed (oxidised for 92 h at 750°C).

The oxide scale morphology at the oxide/metal interface of the non-SP side is different from the SP side and pre-annealed SP side as shown in Fig. 4.3.14 (a) and (b). A non-uniform distribution of the oxidation front at the oxide /metal interface is observed. The interface is having some internally oxidised precipitates. These precipitates were found to be FeCr_2O_4 by EDX. EDX elemental maps at the oxidation front of the non-SP side of the oxidised SPCr-12 + 5 h pre-annealed are presented in Fig. 4.3.15. The corresponding elemental compositions are tabulated in Table 4.3.4.

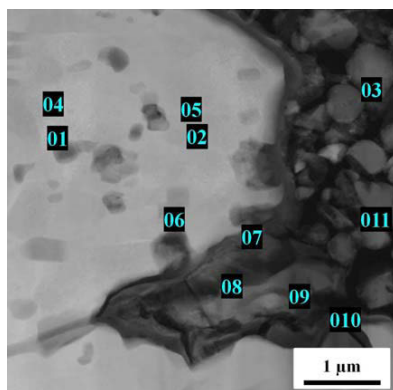


Fig. 4.3.15: EDX analyses positions of the non-SP side of the 5 h preannealed + SPCr-12 oxidised at 750°C for 92 h on the oxide/metal interface.

4 Experimental results and discussion

Table 4.3.4: Elemental compositions obtained from the EDX analysis carried out at the positions shown in Fig. 4.3.15 in at.%.

Position	O	Fe	Cr	Total
01	0.31	92.64	4.02	100
02	0.72	92.23	4.04	100
03	58.69	15.14	25.76	100
04	0.26	92.84	3.88	100
05	0.19	92.75	3.98	100
06	0.66	92.30	3.87	100
07	68.79	17.44	12.43	100
08	82.80	0.91	16.27	100
09	62.55	20.52	15.29	100
10	4.91	88.10	4.17	100
11	63.82	23.17	12.27	100

The elemental composition on the subsurface at positions 01, 02, 04, 05 and 06 shows that the Cr concentration has been reduced to around 3 to 4wt.% (recalculated from the Table 4.3.4) which is far below the original concentration of the alloy. The points in the oxide scale show that the oxide scale is mainly comprised of Fe-Cr spinel. Comparing the subsurface composition of the non-SP side to the composition on the SP side which is shown in Fig. 4.3.11, drastic decrease in the Cr concentration can be observed. The depletion of Cr is high in case of the non-SP side which is more than 8 to 9wt.% whereas in the SP case the depletion of Cr is less, which is around 4wt.% from the original alloy concentration.

4.3.2 Discussion

Based on the experimental results shown above, the difference between the oxidation kinetics of non-SP, SP and SPCr-12 + pre-annealed in summary can be attributed to the change in the subsurface diffusion mechanisms, which are mainly assumed to be caused by the change in dislocation structure and density during different annealing times. In case of non-SPCr-12,

4 Experimental results and discussion

oxidation kinetics is mainly governed by the internal diffusion of O and its solubility in the metal matrix. At the same time the metal at the subsurface region is being depleted in Cr and a formation of Fe-rich oxide scales is more favoured. In turn, these oxides are highly non-stoichiometric in nature.[88, 120-122] This allows further oxygen diffusion into the metal and the oxidation kinetics are drastically increased [84].

This diffusion mechanism is changed in case of SPCr-12, as discussed in the previous section 4.2. The dislocations introduced by the shot-peening treatment were acting as fast diffusion paths for Cr and supplying Cr to the oxidation front continuously maintaining a sufficient amount of Cr at the interface to form Cr-rich Fe-Cr spinel or Cr_2O_3 . Hence, the spinel phase, which is more protective against internal diffusion of oxygen, reduces the rate of oxidation [25, 123]. Due to recovery and recrystallisation, after a few hours of oxidation, dislocations are annealed and rearrange into cell walls, or form grain boundaries, leaving dislocation-free regions [58]. Then the oxidation kinetics depends on the competition between the oxidation rates and the rate of Cr diffusion to the oxidation front. This can be seen in Fig. 4.3.11. There exist two regions; one is slightly Cr-depleted and another one with high Cr-content towards the oxidation front. When the internal oxidation front is moving faster than the external diffusion of Cr then the rate of oxidation is faster and vice versa.

The situation at the subsurface region entirely changes when the SP steel is subjected to a pre-annealing treatment at higher temperature such as 750°C . The elemental mapping on the SP side of SPCr-12 + 1 h pre-annealed clearly shows an enhanced Cr diffusion probably due to the prevalent dislocation arrangement and formation of a Cr_2O_3 layer which in case of the as-received condition would not have been formed (see Fig. 4.3.7). This explains smaller mass gains and thinner oxide scale. The difference in the oxidation behaviour due to pre-annealing the SP sample can be attributed to the difference in the dislocation arrangements.

The surface analysis of the oxide layers formed on SPCr-12 + 5 h pre-annealed sample was presented in Fig. 4.3.8. The difference between the density of the Fe-oxide grains on non-SP side and SP side can be explained as follows. In general, the outer scale formation is favoured by outward diffusion of Fe-ions through the oxide scales. If the internal scale is rich in Cr then the diffusion of the Fe-ions is very slow in this oxide scale and, hence, the growth rate of the outer scale slows down. The presence of a Cr_2O_3 scale at the metal/oxide interface on the SP side makes the inner oxide layer more protective resulting in a reduction of Fe-ion transport (which was already shown in Fig. 4.3.7), whereas in the case of the non-SP conditions the inner layer is less protective, allowing Fe transport through the layer.

4 Experimental results and discussion

The subsurface region undergoes microstructural changes like a deformed material does during recovery. Polygonisation by dislocation climb is possible in all materials, where the dislocations are not too widely split, but only at higher temperatures, where self-diffusion can occur [124]. During this process dislocations undergo transformations, which are accompanied by a decrease of energy and considerably affect the diffusion process. Dislocation climbing requires mass transport by diffusion of vacancies or interstitial atoms. A lattice vacancy can diffuse to the dislocation and similarly interstitial atoms can also diffuse to the dislocation, i.e., atoms from the surrounding crystal could join the extra half-plane leaving vacancies to diffuse away. Thus a dislocation is both a source and sink for vacancies as well as interstitial atoms [125]. Therefore the process of climb and annihilation of such dislocations accompanied by vacancy emission is the characteristic of the relaxation process.

The dislocations are dispersed randomly after shot-peening that some annihilate each other. Those which remain rearrange into walls of dislocations, thus forming small energy 'sub-boundaries' between rather perfect but misoriented 'sub-grains'. Sub-boundaries can be seen as regrouping of infinitesimal dislocations into a finite number of dislocations of the lattice separated by zones of perfect matching [124]. This process is schematically shown in Fig. 4.3.16.

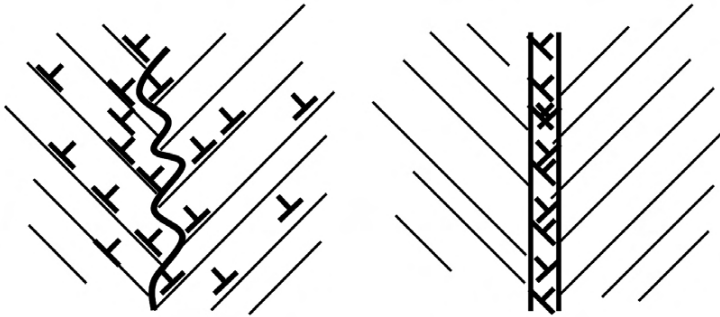


Fig. 4.3.16: Schematic representation showing dislocations before and after climbing and formation of subboundaries.

It is known that diffusivity in these sub-boundaries is proportional to the density of dislocations. The dislocation lines contribute as tubes with a diameter of $5 \cdot 10^{-8}$ cm for diffusion, with diffusion coefficients near to the grain boundary diffusion coefficient [44, 45]. The material is transported along the dislocation line in such a way that the total number of excess vacancies corresponding to the initial area of dipole is kept constant [126]. Sub-boundaries with

4 Experimental results and discussion

dislocations which do not have a common glide direction can only move by diffusion. As for annealing, this process will be regulated by the emission or absorption rate of vacancies on the dislocation jogs, or by the diffusion velocity of vacancies [45].

Diffusion coefficients controlled via the vacancy mechanism (which is usually the most efficient mechanism) is given by the relation

$$D = D_0 \exp(-E_v^m/kT) \exp(-E_v^f/kT), \quad (4.6)$$

where k is the Boltzmann constant, T is the absolute temperature, D_0 is a constant, and E_v^m is the activation energy for the vacancy migration. The factor $\exp(-E_v^f/kT)$ characterises the equilibrium concentration of vacancies in a solid. In the vicinity of climbing dislocations the vacancy concentration exceeds the equilibrium concentration as explained above. This effect is characterised quantitatively by the change in energy for the vacancy formation E_v^f into E_v^{*f} expressed in equation 4.7.

$$E_v^{*f} = E_v^f - W_v(\lambda), \quad (4.7)$$

where λ is the screening radius of the stress fields of the dislocations and $W_v(\lambda)$ is the decrease in the dislocation dipole energy caused by the emission of one vacancy. Applying the linear theory of dislocation density according to Ovid'ko and Reizis [127] gives:

$$W_v(\lambda) = \frac{a}{2d_l} (\lambda = 2a) = \mathbf{G}b^2 aZ/\pi(1 - \nu), \quad (4.8)$$

where a is the average interatomic distance, d_l is the dislocation length, \mathbf{G} is the shear modulus, ν is the Poisson ratio, b is the Burgers vector of the dislocations and Z is a factor taking into account the contribution of the dislocation core to the dislocation energy.

The change in the corresponding diffusion coefficient D^* in the vicinity of climbing grain boundary is calculated as D^* value near to $3 \times 10^5 D$, where D is the diffusion coefficient in the pure crystal. The average diffusion coefficient in a solid with climbing dislocations is $D^\sim = fD^*$, where f is the fraction of the regions of climbing. The shot-peened region (which is strongly in non-equilibrium state) during the relaxation period practically contains excess dislocations, whose climbing process enhances diffusion. In this case f can be approximated to the volume fraction of the subboundaries; i.e., it is assumed to be 0.1-0.5 depending on the average grain size. Hence average diffusion coefficient can be calculated as is $D^\sim = (0.1-0.5) \times 3 \times 10^5 D$ which is approximately to $(3-15) \times 10^4 D$. Hence, during the rearrangement of the dislocations, the climb of dislocations substantially enhances the diffusion process, which

4 Experimental results and discussion

manifests itself in the average diffusion coefficient changing by four to five orders of magnitude.

As discussed above this enhancement of Cr in these dislocation networks can be seen as Cr-rich precipitates in Fig. 4.3.13. This indicates possible enhancement in the Cr diffusion through this dislocation network and supplying enough Cr to the metal/oxide interface and forming Cr_2O_3 at the interface without being depleted in Cr at the surface.

From the experimental results and hardness profiles shown in Table 4.3.1, it is evident that the annealing times for the SP steels are not sufficient to undergo recrystallisation, rather going through the recovery state in which dislocations try to annihilate and form small angle grain boundaries which can be regarded as a series of dislocations. These patterns or arrangements are different for different annealing times. The main question is, if the dislocations arrange in a random manner or in some specific patterns (which would be best for an oxidation resistance). During the polygonisation process, Cr diffusion is enhanced by an order of 4 or 5 compared to the lattice diffusion through the walls of dislocations to the metal/oxide regime and forms a rather continuous Cr_2O_3 layer which protects the alloy against further oxidation. The highest protective nature is obtained in case of smaller annealing times and gradually decreases as the annealing time increases. This can be attributed to the fact that the dislocation arrangement changes during the annealing times and best oxidation resistance is achieved by the higher density of these walls which happened in case of SPCr-12 + 1 h pre-annealed sample. At the same time shot-peening this alloy is attaining good oxidation resistance by enhancing the Cr diffusion through the randomly distributed dislocations and forming a high Cr-rich Fe-Cr spinel and Cr_2O_3 formation at some sites. Pre-annealing the shot-peened steel showed better oxidation resistance by forming a continuous Cr_2O_3 layer all over the metal/oxide regime promoted by the Cr diffusion through the dislocation network. In case of non- SP sample, a continuous oxide layer is not formed over the region thus allowing more oxygen getting soluble in the metal matrix and forming an oxidation zone. Comparing Fig. 4.3.10 and Fig. 4.3.14 it can be stated that shot-peening has changed the oxide nucleation mechanism near the oxide/metal regime by supplying Cr to the oxidation front and forming a rather continuous oxide.

In the case of SPCr-18 the shot-peening itself has proven to be very effective in protecting the alloy by forming a very thin chromia scale on the surface. Shot-peening here comple-

4 Experimental results and discussion

tely changed the diffusion mechanism by promoting Cr to the surface to form a stable layer. Although the oxidation kinetics showed a considerable change in the mass gain due to the annealing process, this effect is not as strong as in SPCr-12. The dislocations introduced by the shot-peening were promoting enough enhancement in Cr diffusion thus changing the oxide scale morphology from dual layer of external CuO and internal FeCr_2O_4 into an external single Cr_2O_3 layer, and the annealing process enabled a very quick formation of Cr_2O_3 layer on the surface.

5 Modelling and simulation

5.1 Background

For a long time simulation of the oxidation processes has been a challenging task for the researchers. The reason is that the effects of thermodynamics of the system and kinetic aspects of oxidation play important roles in defining the final oxidation products. A major initial step was taken in simulating the carburisation behaviour of steels by solving Fick's second law using the solubility product by applying the finite difference method and successfully simulating the thickness of the carburised zones [128]. The most realistic approach for a simulation of high-temperature corrosion processes under near-service conditions was obtained by a mathematical description of the diffusion kinetics in combination with thermodynamic equilibrium calculations to predict phase stabilities for given conditions. The technique was firstly applied to internal nitridation processes of Ni-based alloys [129]. Later on, the model was further developed as to combine a two-dimensional approach of the solution of Fick's law using Matlab and the chemical equilibrium calculator ChemApp. This allowed for successful simulation of internal oxidation phenomena [129-132]. The approach used in the programme InCorr is presented as follows [133].

The commonly used equation to describe the time- and location-dependent change in concentration is the diffusion differential equation known as Fick's 2nd law, which is given in its one-dimensional form in equation 2.31, with D being the diffusion coefficient and c the concentration of a diffusing species. For two-dimensional problems and concentration-independent diffusion coefficients D_x and D_y in x and y direction, equation 2.31 can be simplified as:

$$\frac{\partial c}{\partial t} = D_x \frac{\partial^2 c}{\partial x^2} + D_y \frac{\partial^2 c}{\partial y^2} \quad (5.1)$$

In the program **InCorr** equation 5.1 is solved numerically for all relevant species (metallic and non-metallic solutes) taking into account that the diffusion coefficient may vary within the microstructure, i.e., $D = f(x, y)$. Since analytical methods and solutions to treat solid state diffusion are generally restricted to simple geometries [134], a numerical approach was chosen to treat complex high-temperature corrosion phenomena. With the further development of high speed computers, the chances to get very close to flexible experimental and practical situations have been improved dramatically. As a first step to transform the differen-

tial equation 5.1 into a difference equation, the first derivative of the concentration c after the time t at the location x and y can be approximated as to be the difference quotient of the concentrations at t and $t + \Delta t$. The second derivatives of the right-hand side of equation 5.1 are replaced by the mean values of the second derivatives at the time t and the time $t + \Delta t$.

$$\left(\frac{\partial c}{\partial t}\right)_{x,y} = \frac{c(x,y,t+\Delta t) - c(x,y,t)}{\Delta t} = \frac{1}{2} \left\{ D_x \left(\frac{\partial^2 c}{\partial x^2} \right)_{y,t} + D_y \left(\frac{\partial^2 c}{\partial y^2} \right)_{x,t} + D_x \left(\frac{\partial^2 c}{\partial x^2} \right)_{y,t+\Delta t} + D_y \left(\frac{\partial^2 c}{\partial y^2} \right)_{x,t+\Delta t} \right\}. \quad (5.2)$$

By substituting the second derivatives in equation 5.2 by the corresponding difference quotients of the concentrations at the positions $x - \Delta x_l$, x , and $x + \Delta x_r$, as well as at $y - \Delta y_l$, y , and $y + \Delta y_r$, respectively, at the times t and $t + \Delta t$ one obtains the implicit Crank-Nicolson scheme [134] of the finite difference approach for two-dimensional diffusion.

$$\begin{aligned} \frac{c(x,y,t+\Delta t) - c(x,y,t)}{\Delta t} = & \frac{D_x(x,y)}{2} \cdot \frac{c(x-\Delta x_l,y,t) - 2c(x,y,t) + c(x+\Delta x_r,y,t)}{\Delta x_l(x,y) \cdot \Delta x_r(x,y)} + \\ & \frac{D_x(x,y)}{2} \cdot \frac{c(x-\Delta x_l,y,t+\Delta t) - 2c(x,y,t+\Delta t) + c(x+\Delta x_r,y,t+\Delta t)}{\Delta x_l(x,y) \cdot \Delta x_r(x,y)} + \\ & \frac{D_y(x,y)}{2} \cdot \frac{c(x,y-\Delta y_l,t) - 2c(x,y,t) + c(x,y+\Delta y_r,t)}{\Delta y_l(x,y) \cdot \Delta y_r(x,y)} + \\ & \frac{D_y(x,y)}{2} \cdot \frac{c(x,y-\Delta y_l,t+\Delta t) - 2c(x,y,t+\Delta t) + c(x,y+\Delta y_r,t+\Delta t)}{\Delta y_l(x,y) \cdot \Delta y_r(x,y)} \end{aligned} \quad (5.3)$$

The concept of the finite difference equation 5.3 with locations of variable step widths Δx_l and Δx_r at the left- and right-hand side of x and Δy_l and Δy_r at the left- and right-hand side of y is illustrated schematically in Fig. 5.1.1.

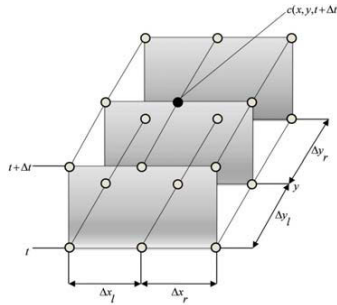


Fig. 5.1.1: Schematic representation of the two-dimensional finite difference mesh applied within the implicit Crank-Nicolson approach.

If applied to an area of the size $n \times \Delta x \times m \times \Delta y$ equation 5.3 can be rewritten as a matrix equation, valid for the concentrations $c(x, y)$ at each location, which can be expressed as concentration vectors $c(t)$ and $c(t + \Delta t)$ for successive time steps t and $t + \Delta t$. Since the right-hand side of equation 5.3 consists of elements of the concentration vectors at different locations according to Fig. 5.1.1, it can be expressed by using the complete concentration vectors $c(t)$ and $c(t + \Delta t)$ multiplied with the corresponding matrices \mathbf{M}_x and \mathbf{M}_y . The product of the matrix \mathbf{B}_x and \mathbf{B}_y with the boundary concentration vectors $c_b(t)$ and $c_b(t + \Delta t)$ is required to establish the boundary conditions in equation 5.3, e.g., at locations ahead of the boundary x_1 no valid concentration value for $x_1 - \Delta x$ within the finite difference mesh does exist, therefore, it has to be defined by $c_b(x_1 - \Delta x, y, t)$. Finally, the location-dependent diffusion coefficients $D(x, y)$ and the flexible step widths Δx_l and Δx_r , and Δy_l and Δy_r are expressed by the matrices \mathbf{R}_x and \mathbf{R}_y , respectively:

$$\mathbf{R}_x = \text{diag} \left[\frac{D_x(x,y)}{2\Delta x_l \Delta x_r} \right] \text{ and } \mathbf{R}_y = \text{diag} \left[\frac{D_y(x,y)}{2\Delta y_l \Delta y_r} \right]. \quad (5.4)$$

Then, the matrix equation representing equation 5.3 for each location step of the finite difference mesh can be written as follows:

$$\frac{1}{\Delta t} [c(t + \Delta t) - c(t)] = \mathbf{R}_x [\mathbf{M}_x c(t) + \mathbf{B}_x c_b(t)] + \mathbf{R}_x [\mathbf{M}_x c(t + \Delta t) + \mathbf{B}_x c_b(t + \Delta t)] + \mathbf{R}_y [\mathbf{M}_y c(t) + \mathbf{B}_y c_b(t)] + \mathbf{R}_y [\mathbf{M}_y c(t + \Delta t) + \mathbf{B}_y c_b(t + \Delta t)]. \quad (5.5)$$

When the boundary concentrations are assumed as (i) to be homogeneous and (ii) to experience only small changes, i.e., $c_b(t) \approx c_b(t + \Delta t)$, and the matrices in equation (5.5) are multiplied according to $\mathbf{M} = \mathbf{R}_x \mathbf{M}_x + \mathbf{R}_y \mathbf{M}_y$ and $\mathbf{B} = 2(\mathbf{R}_x \mathbf{B}_x + \mathbf{R}_y \mathbf{B}_y)$ one obtains the following governing equation for the concentration vector $c(t + \Delta t)$ as a function of the concentration vector at the preceding time step $c_b(t)$ and $c(t)$:

$$[1/\Delta t \mathbf{E}_u - \mathbf{M}]c(t + \Delta t) = \left[\frac{1}{\Delta t} \mathbf{E}_u + \mathbf{M} \right]c(t) + \mathbf{B}c_b(t) \quad (5.6)$$

with the unit matrix \mathbf{E}_u .

Implemented in the commercial simulation design environment MatLab, equation 5.6 is solved for all species participating in the corrosion reaction and stepwise for the complete reaction time $p \times \Delta t$ according to the schematic representation in Fig. 5.1.2 (simplified for one-dimensional diffusion).

5 Modelling and simulation

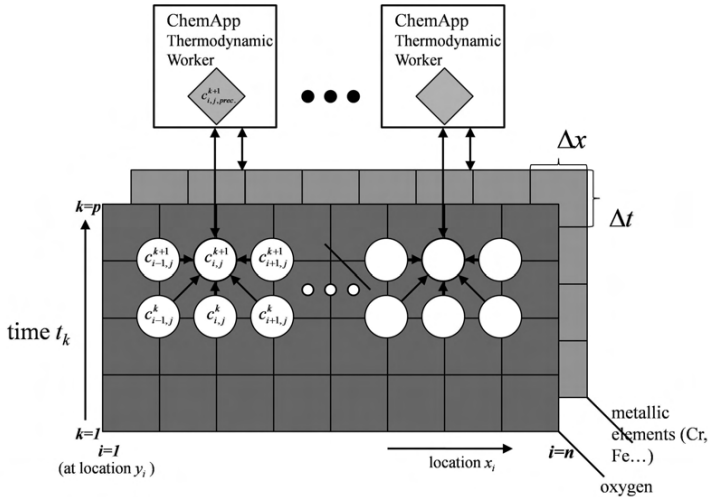


Fig. 5.1.2: Schematic representation of the implicit finite difference technique in combination with the thermodynamic program ChemApp.

To accommodate for the possible chemical reactions of the ongoing corrosion process, the calculated concentrations $c_{i,j}(t + \Delta t)$ ($c_{i,j}^{k+1}$ in Fig. 5.1.2) must be corrected according to the local thermodynamic equilibrium. This is done by means of the thermodynamic subroutine ChemApp as integral part of **InCorr**. More details of on **InCorr** can be found [135]. The biggest advantage of **InCorr** is, that the programme includes the grain boundary diffusion of the corrosive species, as the effect of grain boundary diffusion is a very important factor in determining the final thicknesses of the oxidation products. As discussed earlier in section 2.2.4.1, the grain boundaries are considered as fast diffusion paths for elements such as oxygen and chromium. Schematic representations of the enhanced diffusion coefficient were already shown in Fig. 2.2.6 and Fig. 2.2.7. In the program the grain boundaries were considered as fast diffusion paths in which the diffusion coefficients along grain boundaries can be separately given in addition to the volume diffusion coefficients. The geometry of the desired alloy can be distributed along both X and Y axis, the spacing between the two nodes can be freely chosen accordingly to the desired accuracy. Total length of the mesh is considered in μm . If two grains are considered in the mesh for simulation, one grain boundary can be introduced in between these grains as shown in Fig. 5.1.3.

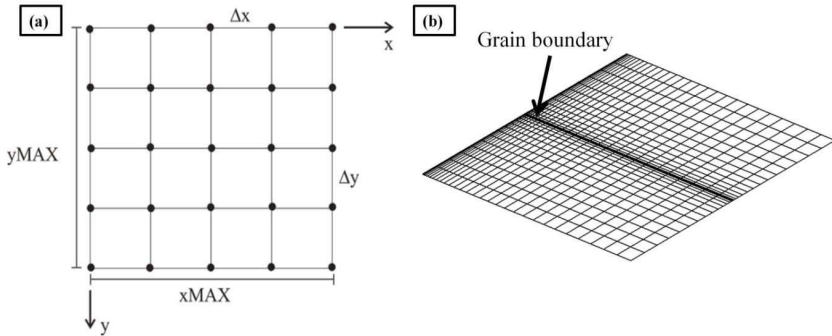


Fig. 5.1.3: (a) Geometry of the discretised mesh, (b) example of a mesh point distribution with variable spacing between the nodes. Close to the surface and along the grain boundary, a fine mesh can be used, in order to get a more accurate representation of the diffusion behaviour.

5.2 Physical modelling of the effect of shot-peening on the oxidation behaviour of steels

The effect of shot-peening on the oxidation behaviour was discussed in detail in section 4.2. From the experimental results shown, it can be emphasised that the dislocations introduced due to the shot-peening, act as fast diffusion paths for Cr to enhance its diffusion coefficient. This results in the formation of a Cr-rich Fe-Cr spinel internally in case of SPCr-12 and a thin Cr_2O_3 scale on the surface of SPCr-18 steel. A schematic representation of the effect of shot-peening on the microstructure of the alloy is shown in Fig. 5.2.1.

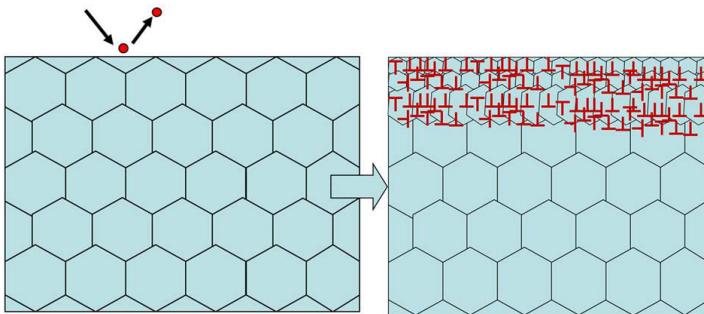


Fig. 5.2.1: Schematic representation of the effect of shot-peening on the microstructure of the steel.

Fig. 5.2.1 illustrates that the bombardment of the surface of the material with a high speed steel ball eventually changes the subsurface microstructure by introducing defects such as dislocations. There can be even grain refinement which was already shown in Fig. 4.2.1 (b). From the experimental section it is known that SPCr-12 contains one non-SP side and one SP side. The oxidation mechanism on the non-SP side can be modeled as follows. When the oxidation starts, the inward diffusion of oxygen and then outward diffusion of Fe and Cr initiates the oxide layer formation. Later the external scale formation is mainly governed by the outer diffusion of Fe whereas internal scale formation is governed by the internal diffusion of oxygen and the diffusion of Cr towards the oxidation front. This process is shown schematically in Fig. 5.2.2.

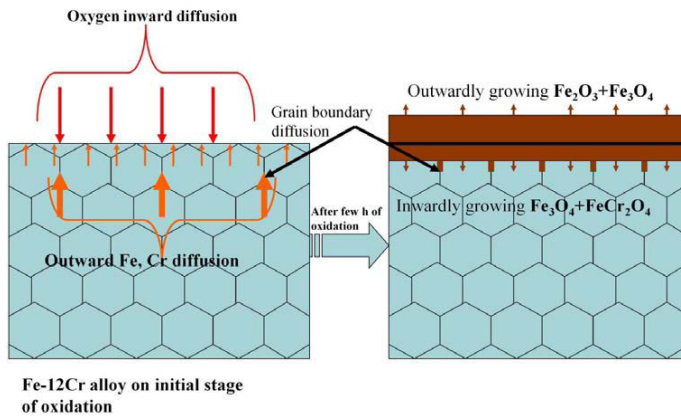


Fig. 5.2.2: Physical model of the oxidation process of the non-SP side of SPCr-12.

Fig. 5.2.2 shows the oxide scale grown on the surface and underneath the original surface. The black line is separating the outer and the inner scale. The diffusion along grain boundaries in addition to the bulk diffusion is also shown in Fig. 5.2.2 (oxide formed along grain boundaries internally). At the oxide/metal interface no continuous oxide layer formed rather discontinuous oxide along grain boundaries can be seen.

The oxidation mechanism on the SP side is schematically shown in Fig. 5.2.3. Note that the dislocations introduced by shot-peening are uniformly distributed over the microstructure of the material down to a certain depth which is defined by the extent of shot-peening. These dislocations are not aligned in one direction, rather they are aligned randomly. As the oxidation progresses, the diffusion of Cr along dislocations comes into act in addition to usual bulk

and grain boundary diffusion. With the internal oxidation, the area which contains initially dislocations will also be oxidised. The dislocations present in the rest of the area which is not yet oxidised will annihilate and climb. The enhanced Cr diffusion due to the presence of these dislocations help to form a thin Cr_2O_3 layer at the oxidation front.

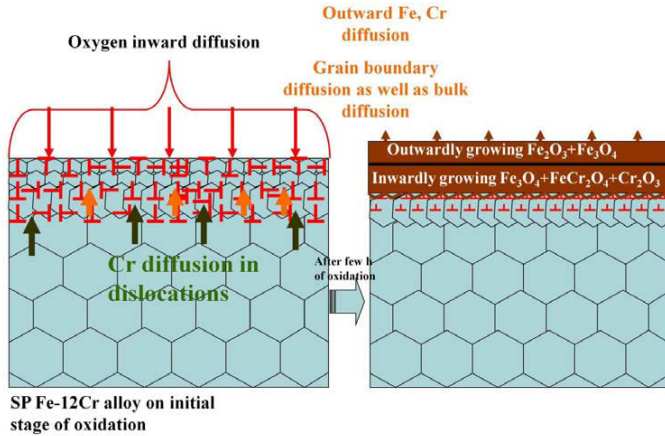


Fig. 5.2.3: Physical model of the oxidation process of the SP side of SPCr-12.

The size of these dislocations are of orders of atomic displacements. It is very difficult to construct a mesh with both nano-sized dislocations and grains of micrometer range due to the mathematical uncertainty with this method and the time consumption for the simulation. So in the simulation individual dislocations were not considered. Rather for a certain depth of the material a high dislocation density is assumed, and in this zone the diffusion coefficient of Cr is enhanced by a factor which is taken from the literature.

5.3 Physical modelling for the simulation of external scale formation

Simulation of the internal corrosion phenomenon was successfully performed by using **In-Corr**. Based on the experimental results by Trindade et al. [132, 136], the internal oxide scale growth was modeled by using following assumptions.

- (1) The inward oxide growth itself is governed by an intercrystalline oxidation mechanism

5 Modelling and simulation

- (2) Oxygen atoms that have reached the scale/substrate interface by short-circuit diffusion through cracks, pores or O anion transport, penetrate along the substrate grain boundaries leading to the formation of Cr_2O_3 and consequently FeCr_2O_4
- (3) The model does not consider the individual diffusion of Cr and Fe in the alloy rather than the effective diffusion coefficient of oxygen calculated on the base of experimental results by using Wagner's theory of scale growth
- (4) The self diffusion of Fe and diffusion of Cr in the alloy does not play any role in defining the final oxide thicknesses as this model mainly dealt with the internal oxidation phenomenon

In the presented simulation work, the whole mesh is divided into two parts as shown in Fig. 5.3.1.

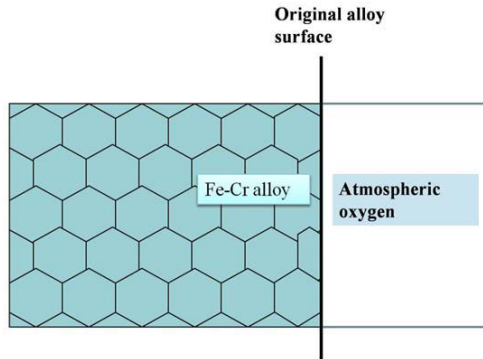
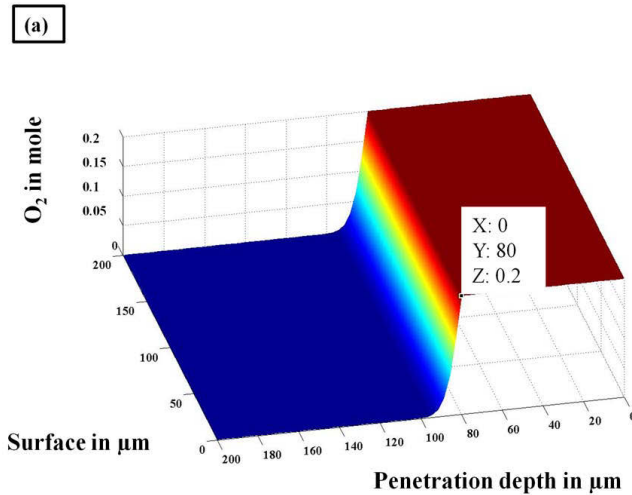


Fig. 5.3.1: The distribution of alloy and atmosphere into a mesh.

The black line which is dividing the atmosphere from the material matrix is drawn at the alloy original surface. The honey comb grain structure shown in Fig. 5.3.1 refers to the ideal grain structure which is very difficult to establish by using finite difference method due to mathematical stability restrictions. This problem was solved by creating a mesh with honey comb grain microstructure by using a more advanced finite element method, which will be discussed in the next section. In fact, the grain microstructure was considered as rectangular grains as shown in Fig. 5.1.3. Then the diffusion equations for the elements diffusing outwards such as Cr, Fe and elements diffusing inwards such as O are solved by using the finite difference method as explained above. Parts of Fe and Cr reach the outer atmospheric region depending on their diffusion coefficients and meet the oxygen which is already present. They

form the stable phase accordingly to the thermodynamics predicted by ChemApp. The simulation of the diffusing species without thermodynamic calculations using the mesh divided into two parts in which the outer part contains oxygen and the inner part is Fe-Cr metal was also done and is presented in Fig. 5.3.2. The simulation results are plotted three dimensionally in which the X-axis represents the total length of the available surface, the Y-axis is the penetration depth of the oxidising species and the Z-axis is the amount of species formed in mole. From Fig. 5.3.2 (a), at position $Y = 80 \mu\text{m}$ the separation of the metal and atmosphere can be seen. The outer area in which the oxygen value is 0.2 bar refers to the atmospheric pressure of oxygen. Then a gradual decrease in the oxygen value refers to the diffusion of oxygen into the metal. Fig. 5.3.2 (b) and (c) show the iron and chromium profiles which they have higher amounts inside the metal and a gradual decrease in their amounts towards the atmosphere indicates the outward diffusion of these species. The simulations were performed for 50 h using arbitrary diffusion coefficients of the species to illustrate the simulation scheme used for the outward scale growth. It should be noted that the simulation profiles presented in Fig. 5.3.2 are only diffusion profiles of individual elements without any thermodynamic calculations. This simulation was performed only to demonstrate the mesh division into metal and atmosphere part and the possible internal and external diffusion. Consideration of thermodynamical calculations along with diffusion calculations will be present in the next section.



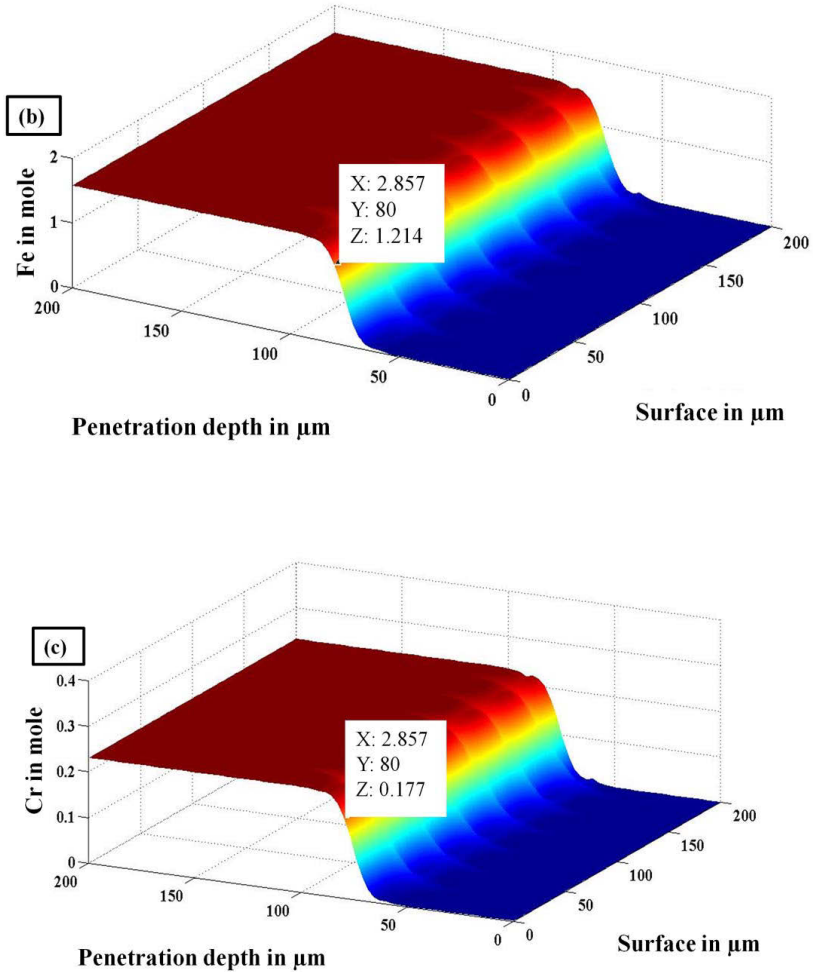


Fig. 5.3.2: Diffusion profiles of (a) oxygen, (b) iron and (c) chromium in a Cr-12 steel at 750°C without equilibrium calculations.

From the gold marker experiment in section 4.1.1, it is known that the outer oxide scale grows by the outward diffusion of Fe leading to the formation of hematite (outermost) and magnetite and that the inward transport of O leads to $(\text{Fe,Cr})_3\text{O}_4$ formation. As a consequence of the Cr content in the substrate, a gradient in the Cr concentrations establishes reaching

from the outer/inner scale interface ($c_{Cr} = 0$) to the inner scale/substrate surface, where the Cr concentration corresponds to the formation of the spinel phase $FeCr_2O_4$ or Cr_2O_3 . Hence, it is proposed that the internal oxide scale growth is mainly due to the oxygen transport via pores, cracks and anion diffusion through the hematite/magnetite, establishing an oxygen concentration at the scale-substrate interface that corresponds to the Fe_3O_4 equilibrium partial pressure. The situation after few minutes of oxidation is drawn schematically in Fig. 5.3.3 in which an outer scale of hematite is growing on the original surface, grain boundary oxidation leads to formation of a Cr_2O_3 on the grain boundaries and an inner layer consisting of magnetite and $FeCr_2O_4$ is formed.

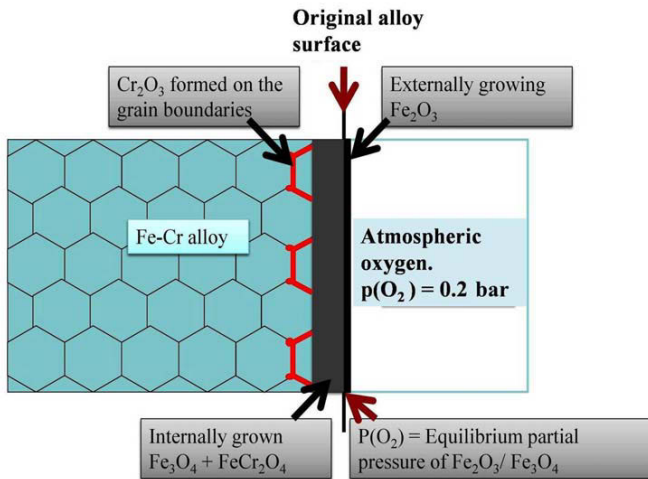


Fig. 5.3.3: Schematic representation of the oxide scale evolution after a few minutes of oxidation.

The following assumptions are made for the simulation of oxide growth:

- (1) A thin Fe_2O_3 oxide layer is already present on the alloy surface as an external scale
- (2) The oxygen partial pressure at the original alloy surface is fixed to the equilibrium partial pressure of Fe_2O_3/Fe_3O_4
- (3) The partial pressure of the oxygen in the atmosphere is kept constant
- (4) The maximum amount of Fe_2O_3 (thermodynamical equilibrium calculations performed by FactSage) formed as a result of alloy composition and oxygen partial

pressure for a particular alloy is used as a threshold for the amount of Fe_2O_3 which could be formed on the surface as an external layer

- (5) Moving boundary condition is applied here not from the mathematical rather the thermodynamical point of view, i.e., when Fe, which diffuses outwards, reaches the point, where it meets oxygen, Fe and O may react forming hematite (According to Fig. 4.1.1, at higher partial pressures of oxygen hematite is the thermodynamically more stable phase). Once the amount of hematite formed equals the threshold amount of hematite for that alloy composition, then the reaction at that point stops and Fe diffuses through the hematite layer

5.4 Simulation results

5.4.1 Simulation of external scale formation

Diffusion coefficients of the diffusing species in the alloys or in the oxide scales are very important for the simulation of the oxidation product formation kinetics of the alloys. The frequency factors and activation energies of the mobile species were taken from the published literature and are presented in Table 5.4.1.

Table 5.4.1: Diffusion data of the species in oxide scales as well as in the alloying systems taken from literature.

Bulk diffusion	$D_0(\text{m}^2/\text{sec})$	T [°C]	E(kJ/mol)	Source
Fe in Fe_3O_4	$5.2 \cdot 10^{-4}$	750-1100	230.11	[137]
Fe in Fe_2O_3	4.0	940-1270	469	[138]
Fe in FeO	$1.18 \cdot 10^{-5}$	750-1100	124.3	[137]
O in Fe_3O_4	10^{-5}	480-1100	264	[139]
O in Fe_2O_3	10^{-7}	1150-1250	611	[138]
O in FeO	0.117	720-1180	375	[140]
O in $\alpha\text{-Fe}$	$2.8 \cdot 10^{-4}$	750-850	92.1	[141]
Fe in $\alpha\text{-Fe}$	$3.78 \cdot 10^{-7}$	500-900	251	[25]
Cr in $\alpha\text{-Fe}$	$3.59 \cdot 10^{-6}$	500-800	179	[142, 143]
O in $\gamma\text{-Fe}$	$5.8 \cdot 10^{-4}$	1173-1573	168.8	[141]

5 Modelling and simulation

Fe in γ -Fe	$7.1 \cdot 10^{-3}$	500-1160	311	[144]
Cr in γ -Fe	0.17	1110-1344	263.90	[145]
Cr in 12CrMoV steel	$1.5 \cdot 10^{-1}$	870-1078	301	[146]
Cr in 18-8 steel	5.38	881-1277	230.4	[146]
O in Ni	$4.9 \cdot 10^{-6}$	800-1100	164	[147]
Ni in Ni	$1.9 \cdot 10^{-4}$	700-950	284.5	[148]
Al in Ni	$1.85 \cdot 10^{-4}$	800-1100	260.78	[149]
Cr in Ni	$5.2 \cdot 10^{-4}$	1050-1375	289	[148]
Fe in Cr_2O_3	$4.95 \cdot 10^{-6}$	1000-1200	44	[150]
Cr in Cr_2O_3	$5 \cdot 10^{-7}$	1100-1700	245	[150]
O in Cr_2O_3	$1.59 \cdot 10^{-3}$	1100-1450	422.6	[150]
O in Al_2O_3	$6.3 \cdot 10^{-12}$	1200-1600	57.6	[25]

The simulation of the external scale formation is complex and gets more complicated when the oxide scales are multi-layered, where the diffusion coefficients of the species have to be changed in every oxide layer due to different phases in different layers. To avoid more complications from multi-oxide layers, the simplest case of a Ni-based alloy which was oxidised at 900°C for 100 h (as a model alloy for the simulation) was chosen for the simulation. The SEM micrograph of the oxidised Ni-base alloy is presented in Fig. 5.4.1. From the XRD and EDX analysis, it was confirmed that a thin continuous Cr_2O_3 oxide layer was formed on the surface which is a result of external diffusion of Cr. Internal precipitates of Al_2O_3 are formed due to the inward diffusion of oxygen into the alloy. Fig. 5.4.1 (a) shows the surface of the oxidised specimen, in which grain boundary oxidation can be explicitly seen, where Cr_2O_3 (arrow marks) formed on the surface and as well as on the grain boundaries.

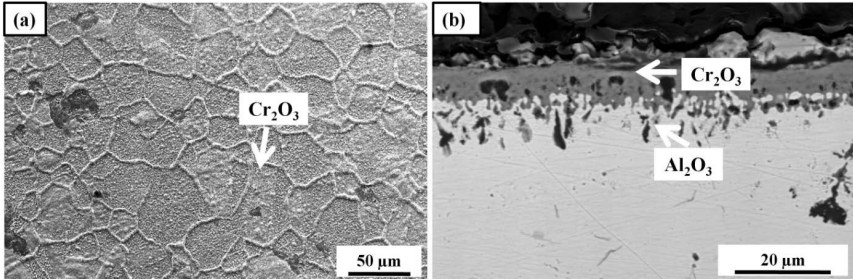


Fig. 5.4.1: SEM micrographs of the Ni-based alloy which is oxidised for 100 h at 750°C: (a) oxidised surface and (b) cross-section.

To simulate the oxide layer growth which is shown in Fig. 5.4.1, two basic diffusion processes should be considered in the simulation. They are the outward diffusion of Cr and inward diffusion of O. As alumina formation is mainly due to the inward diffusion of oxygen there is no need to consider the diffusion of Al in the simulation. In addition to this, the diffusion coefficients of Cr and O have to be changed in metal and formed oxides accordingly. One more important thing is the difference between the densities of the formed oxides. However, the density of an oxide also defines the thickness of that oxide layer, densities of the oxide layers could not be implemented in this simulation as the considered mesh parameters are constant. If the densities of the oxides have to be included in the simulation, mesh should be refined after each iteration step. This increases the complexity of the problem.

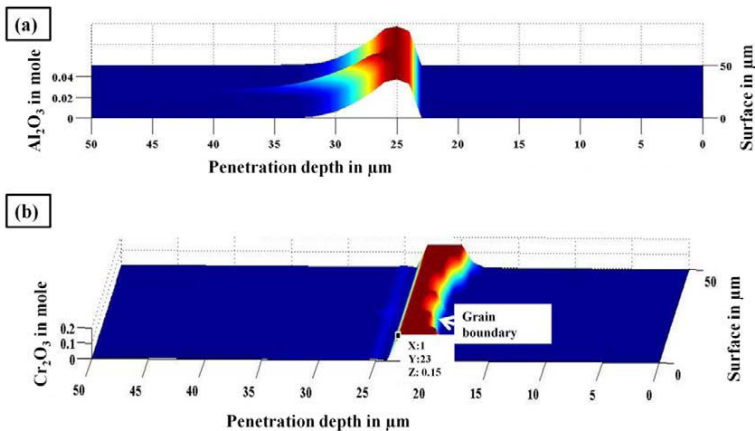


Fig. 5.4.2: Simulated concentration profiles of the oxide layer formed on the Ni-based alloy after oxidising for 100 h at 900°C (a) internally formed Al_2O_3 and (b) externally grown Cr_2O_3 layer.

5 Modelling and simulation

The simulation of the external layer and internal oxide formation on the Ni-based alloy was performed accordingly to the previously explained model. Before starting the simulation a very thin Cr_2O_3 layer is assumed to be initially present on the metal surface instead of Fe_2O_3 as in the case of steel. The diffusion coefficients were used from Table 5.4.1: Diffusion data of the species in oxide scales as well as in the alloying systems taken from literature., and the resulted simulation profiles are presented in Fig. 5.4.2. The original metal surface is chosen at position $Y = 23$ at the initial state of the simulation and then four to five μm thick Cr_2O_3 scale has grown after 100 h of oxidation time externally (see Fig. 5.4.2 (b)). Internally grown Al_2O_3 oxide of thickness three to five μm is shown in Fig. 5.4.2 (a). The amount of Al_2O_3 in mole which is formed internally is found to be very small compared to the externally grown chromia scale, which indicates the possible precipitation of alumina internally. The simulated and experimental thicknesses of the formed oxide layers are found to be in reasonable agreement accordingly to Fig. 5.4.1 and Fig. 5.4.2.

Complications involved in the simulation of multi-layered oxide scale growth on Fe-Cr steels are discussed here. Three diffusing elements such as Fe, Cr and O should be considered in the simulation unlike as two elements in the Ni-based alloy. In addition, the oxides which usually grow on Fe-Cr steels such as FeO, Fe_3O_4 , and FeCr_2O_4 have variable stoichiometric compositions [23, 83]. As discussed in section 2, when Cr starts dissolving in Fe_3O_4 a big change occurs in the stoichiometry of Fe_3O_4 towards FeCr_2O_4 [87-89]. Furthermore, the phase changes from Fe_2O_3 to Fe_3O_4 and vice versa was discussed in the literature [151]. The thicker the oxide scale grows on the surface the longer the distance for Fe to diffuse for the formation of oxides, meanwhile the Fe_3O_4 which was already formed on the surface transforms into Fe_2O_3 . This makes simulation more complicated as both Fe_3O_4 and Fe_2O_3 were found to be externally formed according to the gold marker experiments shown in section 4.1.1. From the existing literature, diffusion coefficients of the mobile species in FeCr_2O_4 are not available. Thus, the difference in the diffusion coefficients of the mobile species (Fe, O and Cr) in magnetite and Fe-Cr spinel can be negligible as spinel type magnetite and Fe-Cr spinel possess the same crystal structure [89].

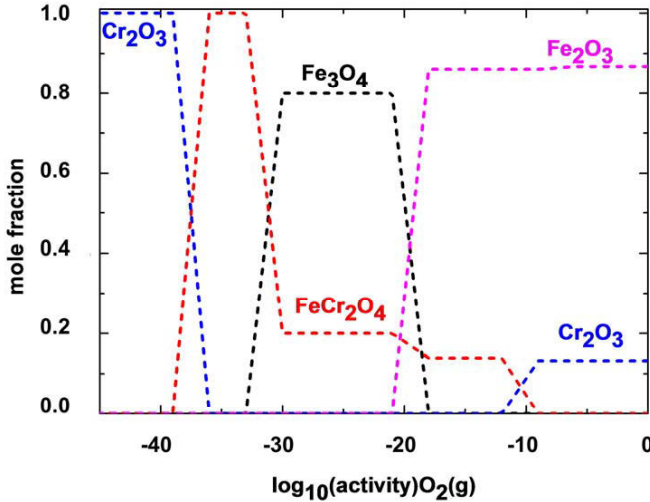


Fig. 5.4.3: The chemical equilibrium calculation of the Cr-12 reacting with oxygen at 750°C.

Chemical equilibrium calculation of the Fe-Cr-O system for Cr-12 steel at 750°C is performed by using FactSage and is presented in Fig. 5.4.3. On the X-axis oxygen partial pressure is varied and on the Y-axis the equilibrium amounts of formed phases are plotted. In Fig. 5.4.3, it can be observed that at higher partial pressures of oxygen, Fe_2O_3 is the most stable phase and with the chemical composition of Cr-12 steels 0.79 moles (recalculated from mole fraction) of Fe_2O_3 can be formed as shown in Fig. 5.4.3. At the same partial pressure Cr_2O_3 is also stable but the amount is very low compared to the Fe_2O_3 because of the chemical composition of the alloy. As the partial pressure decreases Fe_3O_4 and FeCr_2O_4 phases are more stable and at very low partial pressure of oxygen Cr_2O_3 formation is again possible.

Based on the diffusion data given in Table 5.4.1 the diffusion coefficients of all the diffusants are calculated at 750 °C for Cr-12 steel and are presented in Table 5.4.2.

Table 5.4.2: Diffusion coefficients calculated for the diffusing species in Cr-12 alloy at 750°C.

Diffusing element	Diffusion coefficient in m ² /sec
O in Fe ₂ O ₃	6.37×10^{-25}
O in Fe ₃ O ₄	3.34×10^{-19}
Fe in Fe ₂ O ₃	4.56×10^{-24}
Fe in Fe ₃ O ₄	9.49×10^{-16}
O in FeO	8.40×10^{-21}
Fe in FeO	5.9×10^{-12}
O in Cr ₂ O ₃	4.22×10^{-25}
Cr in Cr ₂ O ₃	1.55×10^{-19}
O in α -Fe	6.50×10^{-12}
Fe in α -Fe	4.31×10^{-17}
Cr in α -Fe	2.61×10^{-15}

From the diffusion coefficient values shown in the Table 5.4.2, the following conclusions can be drawn which are very important in simulating the growth of formation of external oxide scale on the steels.

- (1) The diffusion coefficients of O and Fe in Fe₂O₃ are different only by one order of magnitude
- (2) The diffusion coefficient of O in Cr₂O₃ is almost of the same magnitude as the diffusion coefficient of O in Fe₂O₃
- (3) The degree of non-stoichiometry in both chromium oxide and hematite is small and both are protective against rapid diffusion of the diffusion species
- (4) Diffusion of Fe in Fe₃O₄ is 3 orders of magnitude higher than the diffusion of O in Fe₃O₄
- (5) Diffusion of Fe in FeO is several orders of magnitude higher than the diffusion of O in FeO

Based on the above points, it can be expected that Fe₂O₃ is as protective as Cr₂O₃, thus, the internal oxidation growth should be very slow in the steels at this temperature. However,

5 Modelling and simulation

the experimental results showed a thicker internal oxide scale in the studied alloys (Fig. 4.1.3 and Fig. 4.1.7). This gives support to the idea that oxygen availability at the oxide original surface underneath the externally grown hematite layer is not due to solid-state diffusion of oxygen through hematite, rather the oxygen is using fast diffusion paths such as cracks and voids which are always present to a large extent in hematite layer. That means oxygen is always available at the interface so that internal oxide grows rapidly.

Simulation results of the thicknesses of both the external and internally grown oxide layers on Cr-12 after oxidising for 120 h at 750°C are presented in Fig. 5.4.4. The alloy original surface was considered at Y= 60 at the initial state before the simulation begins.

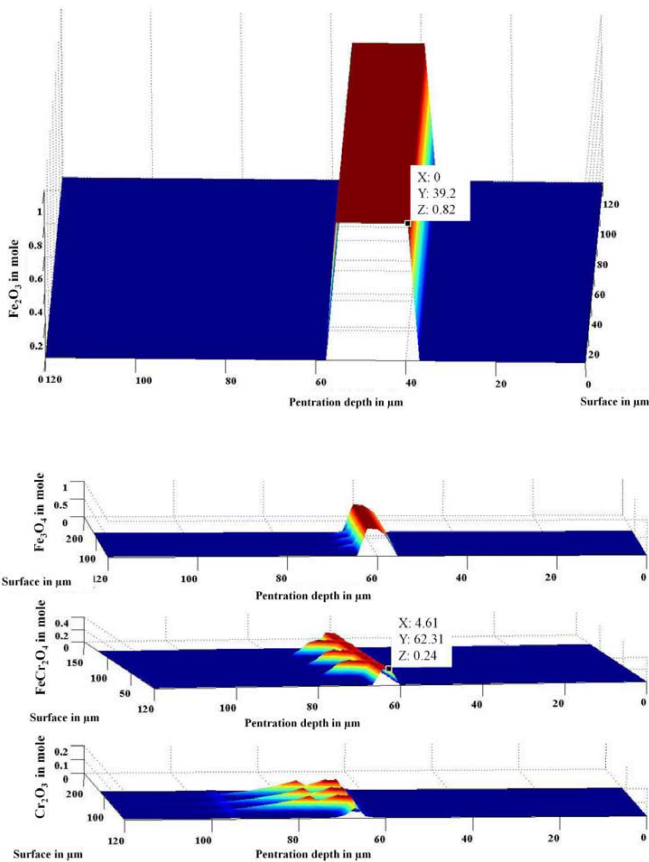


Fig. 5.4.4: Simulated oxide scale thicknesses formed on Cr-12 oxidised for 120 h at 750°C.

The hematite which was assumed to be present on the surface grows outside and its thickness is found to be about 20 μm . It was already mentioned that the main transport mechanism in wustite/magnetite is cation motion [75, 76]. As it is aforementioned the diffusion of Fe in internally grown magnetite is faster than incoming oxygen, Fe cations reach the oxide/metal interface and reacts with the oxygen (it is assumed that the oxygen is always available at the interface due to the presence of cracks and voids in hematite). This enables the growth of hematite externally. Magnetite is present on the original alloy surface as well as underneath the surface and its thickness is found to be 9 μm . Fe-Cr spinel is found to have grown internally and its thickness is 10 μm and it formed along the grain boundaries as well. Chromium oxide was formed along the grain boundaries. The simulation results of the oxide scales were found to be consistent with the experimental observation as shown in Fig. 4.1.7 (b).

5.4.2 Simulation of effect of shot-peening

The oxide scale formation on Cr-18 when it is oxidised at 750°C for 120 h was simulated and the resulting oxides are presented in Fig. 5.4.5. The diffusion coefficients were taken from Table 5.4.2. The mesh is divided into two parts as shown in Fig. 5.3.1. The original surface of the alloy was chosen at position $Y = 25$. The oxygen partial pressure is set to atmospheric pressure as an initial condition. As the oxidation time increases, the inward diffusion of oxygen and outward diffusion of Fe and Cr starts and forms the oxide phases as the thermodynamic equilibrium predicts. The individual diffusion coefficients of the diffusing species were then changed from the diffusion coefficients in the alloy to the diffusion coefficients in the formed oxide scales. From Fig. 5.4.5, it can be seen that the formed oxide scale has a three layered structure. The formation of Fe_3O_4 and FeCr_2O_4 on the outer surface can be observed. The position of the FeCr_2O_4 is found to be exactly on the original alloy surface and the Fe_3O_4 is formed as an outer scale. The internal formation of Cr_2O_3 can also be identified as a result of internal diffusion of the oxygen through the outer scale. The experimental results on this alloy as shown in the Fig. 4.1.7 (c) and Fig. 4.2.12 (e) confirms that the Fe-Cr spinel which is formed externally is rich in Cr at the interface and then iron-rich spinel is formed on the top. A thin CuO was also observed in the experimental results, which was not simulated here because of the insufficient database of Cu in the alloying system. The total thickness of the oxide scale from the simulations is found to be 10 μm which is less than the experimental observations. The reason for the difference in the simulated and experimentally observed thickness

5 Modelling and simulation

can be explained as following. The presence of cracks and pores in the oxide scales was not considered in the simulation. The estimation of the grain boundary diffusion coefficient of oxygen in the alloy can be smaller than that of reality. The simulation results are found to be in good agreement with the experimental results.

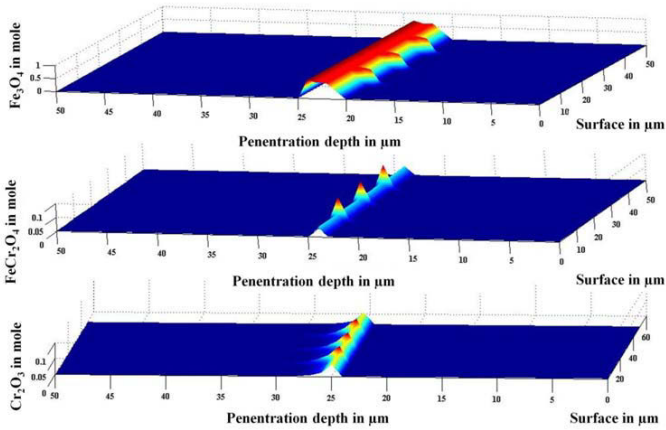


Fig. 5.4.5: Simulation results of the oxide scale formation on Cr-18 subjected to oxidation at 750°C for 120 h.

Simulation of the effect of shot-peening on the oxidation behaviour of Cr-18 is done as follows. According to the modelling in section 5.2, the thickness of shot-peened area is considered as 30 μm based on the hardness profile measured on SPCr-18 sample which is shown in Fig. 5.4.6. Even though the hardness change due to the shot-peening is observed about 150 μm deeper into the sample, maximum change is confined to 30-40 μm.

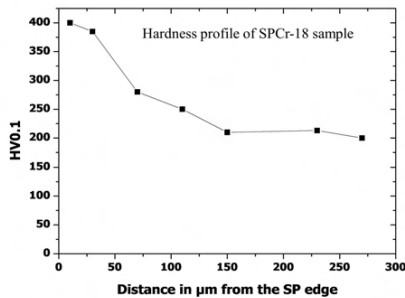


Fig. 5.4.6: Hardness profile of SPCr-18 sample. Measurements were taken starting from the SP side and continued towards the centre of the sample

5 Modelling and simulation

From the literature it is known that the enhancement in the diffusion coefficient of Cr resulting from the presence of dislocations is three orders of magnitude as compared to the bulk diffusion of Cr [48]. The diffusion coefficient of Cr in Cr-18 steel as given in Table 5.4.1 is increased by three orders of magnitude. The diffusion coefficients of Fe and O are taken from the literature data which are given in Table 5.4.1. From the annealing experiments done on the SPCr-18, it is known that the recovery occurs between 1 h and 24 h of pre-annealing at 750°C which is equal to the oxidation temperature (see Table 4.3.1. Hardness value has dropped to 270 HV0.1 after 24 h of annealing). Based on this fact the enhancement in the Cr diffusion coefficient was considered in the simulation for the initial 5 h of oxidation only. After 5 h of oxidation, bulk diffusion coefficient of Cr is introduced in the simulation. As the simulation progresses, a Cr_2O_3 scale forms on the surface. At the places where chromia forms the diffusion coefficients of Fe, O, and Cr are changed to the diffusion coefficients in chromia as given in Table 5.4.1. The simulated profiles are presented in Fig. 5.4.7. No Fe-oxide formation can be seen. Once the oxidation initiates, due to the higher diffusion coefficient of Cr than the internal diffusion of oxygen, Cr reaches the surface faster and forms the chromia layer. Once the chromia forms, the diffusion of oxygen slows down drastically, resulting in a slowly growing chromia layer of 2 μm thick.

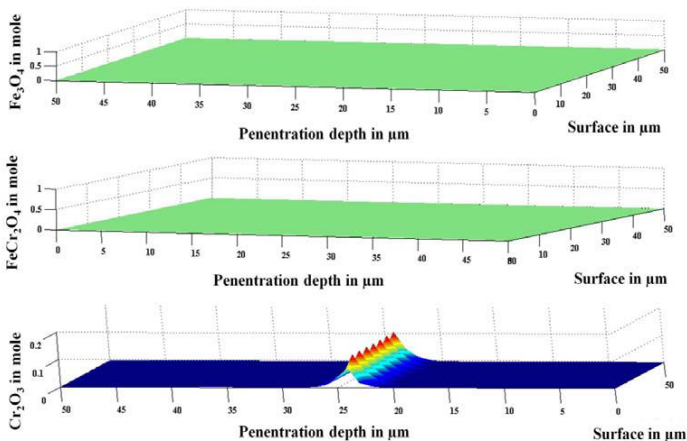


Fig. 5.4.7: The simulated profiles of the oxide scales formed on SPCr-18 which is oxidised at 750°C for 72 h.

The experimental observation of this oxidation profile was presented in Fig. 4.2.12 (f). The comparison of the simulated thicknesses with the experimentally observed thicknesses shows that the simulation results for the shot-peening effect are in good agreement with the experiments.

5.5 Simulations using finite element method (FEM)

These simulations using FEM method were developed in collaboration with Max-Planck-Institut für Eisenforschung, Düsseldorf. The basic idea of using chemical equilibrium calculation along with diffusion calculations of the species simultaneously at every reaction step is used as it is, and only the algorithm for solving the diffusion equations and the mesh creation is changed according to FEM.

5.5.1 Modelling using FEM

In the previous subchapters, it was shown that the Fick's law was solved by using the Finite difference method. Regarding the finite difference method, there exist always problems with the mathematical stability as the solution is determined by solving a system of linear equations; the number of unknowns is equal to the number of known values. To obtain a reasonably accurate solution, thousands of points are usually needed, but the computing time and hence the costs also increase. Hence, the solution of partial differential equations for a complicated geometry such as a honeycomb structure of grains in an alloy is almost impossible by using the finite difference method. This problem can be solved by using the Finite Element method [152]. This work was developed in collaboration with MPIE, Düsseldorf. The basic idea of FEM is to divide the body into finite elements, often called elements connected by nodes, and obtain an appropriate mesh, which represents the near-real microstructure as shown in Fig. 5.5.1.

5 Modelling and simulation

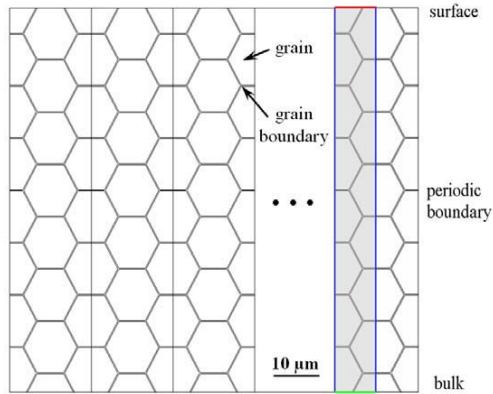


Fig. 5.5.1 Microstructure and boundary conditions used for the simulations [153].

The oxygen concentration at the surface (right boundary) is set to a constant concentration, according to the maximum solubility of oxygen in pure iron at given temperature and oxygen partial pressure. This corresponds to the constant source model, firstly proposed by Fisher [53].

Migration of the atomic species (i.e. iron, chromium and oxygen) is derived from the set of partial differential equations shown in equation 5.1, by means of the numerical simulation programme COMSOL (COMSOL Inc., USA). The formed oxide phases were considered to be immobile. Hence their movement was not taken into account in this step.

Enhanced element migration, according to Fisher's model, occurred in the grain boundary domains assuming a grain boundary thickness of 50 nm. This value corresponds to the thickness of the experimentally observed grain boundary oxides [154]. Due to the lack of reliable data for the oxygen diffusion coefficient along the grain boundary domain, its value was assumed to be 100 times faster than in the bulk material to fit experimental observations.

The calculation of the diffusion was carried out for small time intervals. The results obtained after each calculation step were transmitted into the thermodynamic sub-routine ChemApp (GTT-Technologies, Germany) for recalculating the phases in chemical equilibrium. The amount of each phase from the equilibrium calculation was set as the starting value for the diffusion calculation in the next time step.

After the last simulation step, the results were displayed as a 2D concentration map of each phase individually – similar to a cross-section of the specimen – as well as the element concentration distribution in the sample.

5.5.2 Simulation results using Comsol

Simulation results of the inner oxidation products of Cr-9 steel when oxidised at 750°C for 120 h are presented in Fig. 5.5.2. The distribution of the oxidation depth was derived from the steepest decrease in the innermost presence of the chromium containing oxides, since Cr_2O_3 is the first thermodynamically stable oxide phase which is formed. As can be seen from Fig. 5.5.2, the evolution of the total oxidation depth undergoes drastic changes during the initial stages of the oxidation. Whereas after 16 h, chromium oxide precipitates can be formed at 30 μm below the sample surface, the oxidation depth at 72 h is 55 μm . For longer time spans, the total oxidation depth increases slightly, as the oxygen flux towards the bulk material gets lowered due to iron oxidation. The calculated oxidation depths correlate nicely with the experimentally observed values, which can be found in Fig. 4.1.7. The peaks in graph on the bottom side of Fig. 5.5.2 are the result of the periodicity in the simulated microstructure and originate from the different amounts of the oxides, both inside the grains and along the grain boundary domains. A maximum oxidation depth of 60 μm including grain boundary oxidation was calculated for 120 h.

5 Modelling and simulation

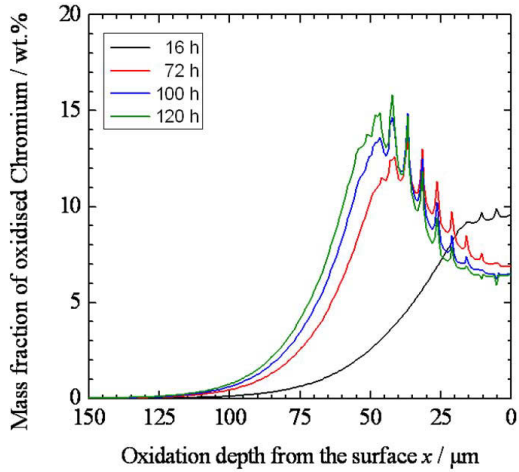
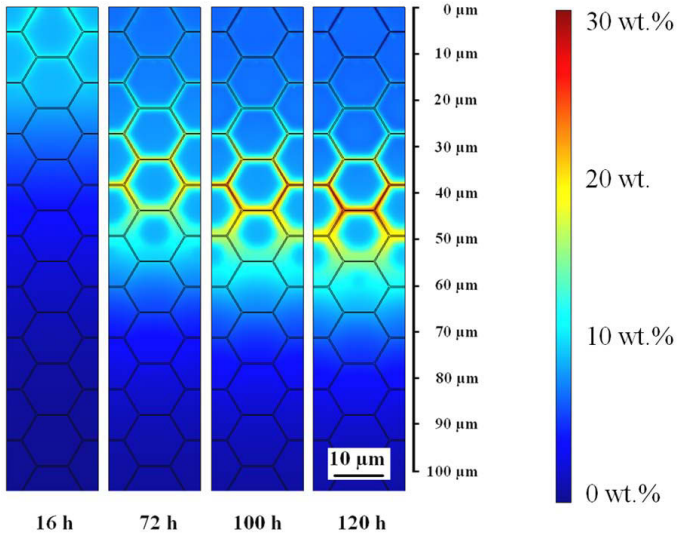


Fig. 5.5.2: Computed 2D-distribution (top) and line scan representation (bottom) of the weight fraction of oxidised chromium (Cr_2O_3 and FeCr_2O_4) in Fe, Cr, oxidised at 750°C for various times [153].

The sequence of the formed oxides follows the predictions from the thermodynamic stability diagram in Fig. 5.4.3. Initially, at low oxygen partial pressure (meaning inside the non-oxidised bulk material) the formation of chromia could be observed, which is then converted into the spinel compound FeCr_2O_4 . At a later stage, the remaining iron matrix gets oxidised into the wustite phase, which then converts into magnetite. Thus the pure iron oxides are only present, when the chromium has already been fully converted into the spinel (Fig. 5.5.3). It can clearly be seen that due to the elevated diffusion of iron, chromium and oxygen along the grain boundary domains, the spatial distribution is changed, but the sequence of oxide formation remains the same.

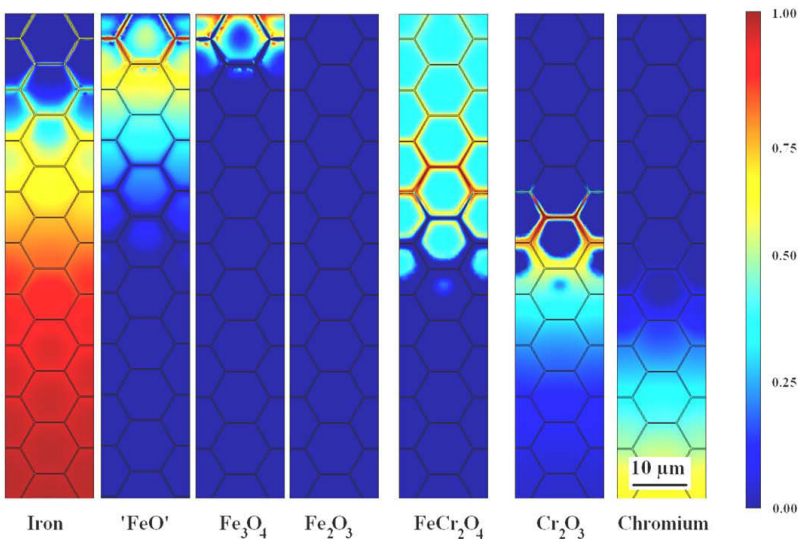


Fig. 5.5.3: Detailed phase distribution of all occurring phases in the alloy Cr-9 after oxidation at 750°C for 120 h [153].

Differences between the experimentally determined phase distribution and the results of the thermodynamic calculations occur in the case of Cr_2O_3 . Thermodynamically, chromia has to be the first oxide to be formed, whereby it should be present between the spinel type FeCr_2O_4 precipitates and the non-oxidised bulk material. However, only minor amounts of chromia could be detected in the measured samples. This finding is in agreement with the results of Kuroda et.al. [154], who argued that the formation of a hexagonal chromia nucleus is kinetically hindered compared to a cubic spinel-type oxide. Therefore, chromia is mostly not observed in experimental samples.

Enhancements in the computing speed, as compared to the initial programme **InCorr**, enable a better resolution of the spatial phase distribution and allow the consideration of different diffusion coefficients of the newly formed (oxide) phases.

5.6 Discussion of the simulation results

The simulation results presented in the previous section showed that the modelling of the simultaneous external/internal oxide scale formation and the effect of shot-peening was convincingly matching the experimental results. However, as the simulation results were based on certain assumptions, the modelling of the external scale formation in addition to the internal oxidation is discussed more elaborately in the following.

The theory of internal oxidation under the presence of an external oxide layer was extensively discussed in the literature [155-158]. The transformation from internal oxidation to external scale formation was also reported in the literature [159]. However, all the existing theories are limited to a binary alloying system AB, in which B is the reactive element and forms BO internally. If the alloy forms a stable BO on the surface of the alloy then the concentration of B in the alloy has to be large enough to make BO more stable than AO. Thus, the concentration of B at the alloy surface during oxidation must not fall below the critical value. The more reactive element B must not be oxidised internally, because this process produces isolated particles of BO dispersed in the metal matrix, which grow as a non-protective scale. A transition from internal to external oxidation of B occurs at sufficiently high concentrations of B in the alloy, as discussed by Wagner and Rapp [41, 160]. According to them the development and maintenance of a continuous external scale requires that two criteria are satisfied. First, the solute concentration in the alloy must exceed that necessary for outward diffusion to prevent internal oxidation. Second, once a continuous external scale is formed, diffusion in the alloy must be rapid enough to supply the solute at least that fast that the rate of scale growth is satisfied. Using these two criterions for the Fe-Cr alloys Essuman et al. [161] estimated the amount of Cr required to form a chromia scale on the surface and the amount of Cr supply at the interface. They found that the minimum amount of Cr required to form a continuous chromium oxide layer on the surface of a ferritic Fe-Cr alloys, varied between 9 and 14wt.% in the temperature range of 900-1200°C. For austenitic Fe-Cr alloying systems the value lies between 2.6-3.2wt.% for the same temperature range.

5 Modelling and simulation

For the alloys used in this study, the Cr concentration in the alloy was around 12wt.% for Cr-12 and 18wt.% in Cr-18. According to the mentioned theories all the alloys would have formed a chromia scale on the surface. However, from the experimental results it was shown that neither of the alloys used were able to produce a chromia layer on the surface externally. The oxide scale morphology formed on the alloying systems used is represented schematically in Fig. 5.6.1.

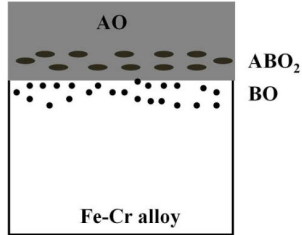


Fig. 5.6.1: Schematic representation of oxidation mode of Fe-Cr alloying systems used in this study. A: Fe, B: Cr.

Fig. 5.6.1 shows that both alloying elements oxidize simultaneously to give AO and BO, the oxygen partial pressure in the atmosphere being greater than the equilibrium dissociation pressure of both oxides. In this case different oxide scale formation mechanisms are possible.

- (1) AO and BO react to form a compound
- (2) AO and BO form a solid solution (A,B)O. In practice, some internal (A,B)O richer in A can be formed in the alloy
- (3) A double oxide is formed, often as spinel, which may give a complete surface layer of variable composition

In the alloying system used in this work, under conditions where Fe (A) and Cr (B) oxidize as shown in the Fig. 5.6.1, the transient oxidation of Fe must be considered for the reaction in order to predict the minimum amount of Cr to form a single continuous external layer of Cr_2O_3 . In addition, the compositional changes from FeO, Fe_3O_4 and Fe-Cr spinel should also be considered in the model. Moreover, the diffusion of Cr in short circuit paths such as grain boundary diffusion and diffusion through dislocations must be considered in the model. In the literature no such kind of model exists which considers all the factors as explained above to predict the external scale formation.

5 Modelling and simulation

To take into account the complexity of the alloying systems investigated, the simulations required experimental observations as input parameters. The simulations performed in the present work were based on the experimental observations. If the alloy is found to be oxidised simultaneously (both internally and externally) then a very thin outer oxide is assumed to be formed on the alloy surface as a starting point for the simulation. The equilibrium partial pressure of oxygen (calculated by FactSage) at the interface between the external/internal oxide scales is given as initial condition for the growth of the internal oxidation. If the inner oxide scales are Fe rich, then the diffusivity of oxygen is smaller than the Fe diffusion through these oxide scales and Fe reaches the outer surface by means of diffusion to form an outer scale. If the formed oxide scales are rich in Cr then the diffusivities of all elements are slowed down in the scales and the final thickness of internal and external scales are reduced. The formation of a chromia oxide layer on the surface due to shot-peening was modelled on the basis of oxidation kinetics. The criterion is that under given atmospheric pressure the diffusivity of Cr is enhanced in an effective area where dislocations are assumed to be present during the oxidation so that the internal diffusion of oxygen can be hindered and a chromia scale forms on the surface.

The change from the finite difference method to FEM by means of Comsol showed better simulation results in terms of mathematical stability (using small time steps and mesh discretisation of the mesh), good spatial resolution, phase distribution and capability of handling the honey comb grain structure.

6 Concluding discussion

The goal of the presented work was to verify and understand the influence of Cr-content on the oxidation behaviour of boiler steels as explained in the introduction chapter. The effect of microstructural change induced by the shot-peening treatment on the oxidation behaviour was also studied experimentally. The concept of dislocation engineering was further applied to the chosen steels and its effect on the oxidation behaviour was studied systematically with the help of TEM. Based on all the experimental results, a model for a simultaneous outward and internal oxide scale growth was proposed and oxide thicknesses were calculated. A model for the effect of shot-peening was also implemented and the corresponding results were presented. A concluding discussion on the performed work is presented as following.

6.1 The mechanisms of internal and external layer formation

The majority of studies on high temperature oxidation of steels are based on the assumption that oxides on low-alloy steels grow only by Fe outward diffusion, since the lattice diffusion coefficient of O anions in iron oxide is very small [137, 162, 163]. On the other hand, few studies discuss a mechanism for inward oxide scale growth which is correlated with the fast oxygen diffusion along oxide grain boundaries [164-166]. Elsewhere, the possibility of molecular oxygen permeation through micro-cracks and pores in the oxide scale is proposed leading to inward oxidation [75, 167, 168]. To understand the mechanisms of the oxide layer growth in the studied steels, a gold marker experiment was conducted on Cr-9 steel and the results were presented in Fig. 4.1.3 (a). The oxide morphology reveals that the iron oxides which grow on top of the gold marker are a result of external diffusion of Fe and the oxides present underneath the marker are due to the inward diffusion of oxygen. The uneven metal/oxide interface and the preferentially oxidised grain boundaries in the bulk are indications of an internal/intergranular oxidation mechanism by which scale grows inwards. Obviously inner scale grows by advanced grain-boundary oxidation, i.e., oxygen penetrates along the substrate grain boundaries leading to the formation of the stable oxide Cr_2O_3 . In the case of inward oxidation, grain boundaries serve as short-circuit diffusion paths for O-diffusion. From the literature it is known that the relation between the diffusion coefficient along grain boundaries and in the bulk lies in the range of 10^4 - 10^6 [48]. Hence, the internal oxides firstly nucleate and grow on the grain boundaries. The higher thermodynamical stability of Cr_2O_3 compared to the Fe-oxides enables easy formation even though the oxygen content is rather low.

Therefore, the observed formation of Cr_2O_3 at the intergranular reaction front is reasonable. The depletion of Cr due to the reaction process cause Fe to take part in the oxidation process, as soon as the oxygen concentration has increased to a level of thermodynamical stability of the FeCr_2O_4 spinel phase. With increasing oxygen potential and Fe to Cr ratio a part of the spinel phase ($\text{Fe}(\text{Fe,Cr})_2\text{O}_4$) will be transformed into magnetite, spreading from the grain boundaries into the grain interiors via oxygen bulk diffusion.

The layered structure of the oxide scale formed on these steels was predicted by thermodynamic calculations which were shown in Fig. 4.1.1. Hematite and chromia were present at high oxygen activities, while with decreasing oxygen activity magnetite and spinel become stable. Only Cr_2O_3 exists at lower oxygen potential. It is reasonable to assume that the outer layer was predominantly composed of hematite and magnetite basically resulting from the outward diffusion of Fe. The inner layer is mainly composed of spinel with limited Cr_2O_3 distributed at the front and results from the inward oxygen diffusion. From the present work and previous reports, it is noted that both outward and inward transport of iron and oxygen are involved in the scale growth of the steels studied.

6.2 Effect of Cr content on the oxidation behaviour

In this section the influence of alloy chemistry on the oxidation behaviour is discussed. Gravimetric measurements during oxidation of all the three steels studied showed that they were oxidised parabolically (see Fig. 4.1.4). Depending on the alloy composition and on the oxidation temperature three different behavioural patterns were observed. Growth of a thin protective oxide scale with a corresponding small mass change with the lowest parabolic constant was observed in case of Cr-18. An accelerated attack with a high parabolic rate constant was observed in Cr-9 which was noted by a large mass gain corresponding to the fast growth of a non-protective oxide scale with pores at the inner and outer scale interface as shown in Fig. 4.1.7 (a). Cr-12 also exhibited a parabolic behaviour with a parabolic constant in the range between the values of Cr-18 and Cr-9.

The beneficial effect of increasing the Cr content is a well-known fundamental of oxidation science. Increasing the Cr content in the alloy would lower the Cr-depletion at the interface for a given exposure time. When increasing the Cr content in the steel, the inner scale becomes more enriched in Cr leading to a better protection of the substrate. As shown in Fig. 4.1.8, the Cr distribution in the oxide scales formed on the studied steels reveals an enrich-

ment within the inner scale with a gradual increase in the Cr concentration from a low value at the outer/inner scale interface towards a high value at the inner scale/substrate interface. XRD analysis on all three steels showed that the inner scale is a mixed Fe-Cr spinel phase. Based on the experimental results, a schematic representation of the three alloys after the oxidation at 750°C for 120 h is presented in Fig. 6.2.1.

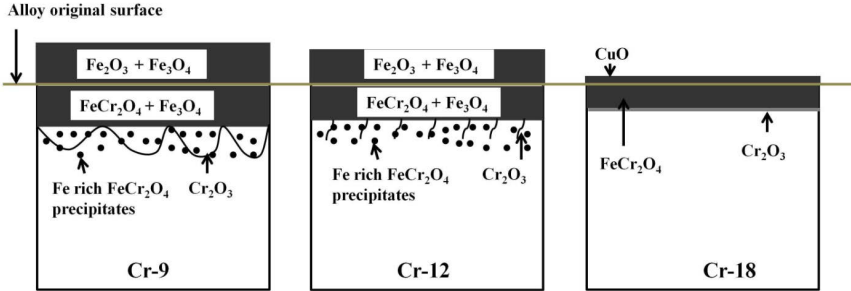


Fig. 6.2.1: Schematic representation of the oxide morphology of the studied steels.

From Fig. 6.2.1, it can be seen that at the reaction front in case of Cr-9 and Cr-12 Cr_2O_3 forms along the grain boundaries. The outer scale comprises of an outer Fe_2O_3 scale and an inner Fe_3O_4 layer. The Cr content in the inner scales of Cr-9 steel was found to be smaller than that of Cr-12. In addition to these oxide scales, the internal oxidation zone consists of an oxide film and precipitation of oxide particles in the grain interior, which was observed for Cr-9 and Cr-12. From the EDX measurements as shown in the result sections, the oxide particles were found to be iron rich precipitates. The inner scale in case of Cr-18 mainly consists of Cr-rich Fe-Cr spinel and a very thin chromia scale formed at the oxide/metal interface which acts as a barrier for internal oxygen attack and, hence, it decreases the oxidation kinetics.

For the three steels studied, it can be said that the Cr concentration was not sufficient to develop a slow growing Cr_2O_3 scale on the surface of the alloy that would protect the substrate. In the cases of Cr-9 and Cr-12 the outer layer contains Fe_2O_3 and Fe_3O_4 while the inner layer is a spinel phase of $\text{Fe}(\text{Fe},\text{Cr})_2\text{O}_4$ type. The Cr enrichment in this spinel phase changed considerably from small amounts to large amounts depending on the original Cr concentration.

6.3 Effect of shot-peening on the oxidation behaviour

The oxidation behaviour of the Cr-alloyed steels depends on many variables in which an important factor is the diffusivity of Cr in the alloy, with differences expected between alloys with different grain size, or with different amounts of surface deformation to alter the density of fast diffusion paths. Fast diffusion of Cr along extended defects play an overwhelming role by increasing the chromium flux towards the surface and thereby promotes the formation of protective oxides. The surface of the Cr-12 and Cr-18 steels was treated by means of shot-peening. The microstructural features of the shot-peened surface are significantly different to the bulk material. The microstructure of the shot-peened and non-shot-peened surface of Cr-12 and Cr-18 are presented in Fig. 4.2.1 and Fig. 4.2.2. Shot-peened region contain a large number of grain boundaries and dislocations. In addition to the microstructural examination, hardness measurements were carried out on the surface to verify the effect of shot-peening. Higher hardness near the surface of the shot-peened sample compared to the non-shot-peened surface is shown in Table 4.2.1. The change in the hardness explains the difference in the microstructure caused by the plastic deformation. The schematic representation of the microstructural change caused by the shot-peening is presented in Fig. 5.2.1. The grain refinement and presence of dislocations near the shot-peened surface can be identified from Fig. 5.2.1. The gravimetric measurements on the shot-peened Cr-12 and Cr-18 at the studied temperatures are presented in Fig. 4.2.3 and Fig. 4.2.11. Both SPCr-12 and SPCr-18 exhibited parabolic behaviour. The parabolic rate constants which are presented in Table 4.2.2 and 4.2.3 explain the effect of shot-peening on the oxidation behaviour of SPCr-12 and SPCr-18. The shot-peening effect on SPCr-12 is not as strong on the oxidation behaviour as it was observed on SPCr-18 at 750°C. At 700°C the shot-peening effect is more pronouncing in case of SPCr-18 as the parabolic constant drops by one order of magnitude. In case of SPCr-12 the effect is reversed and it enhanced the oxidation kinetics by promoting the formation of non-protective Fe-oxides. It is assumed that at this temperature the activation energy for the Cr diffusion was not sufficient to diffuse faster than Fe even under presence of dislocations. The discontinuous oxidation measurements done on SPCr-12 at 750°C reveals that during the initial stages of oxidation both shot-peened and non-shot-peened surfaces oxidises similarly and after some time the shot-peening effect comes into act by creating a higher number of nucleation sites for the oxidation (see Fig. 4.2.4). The Cr diffusion is enhanced along the dislocations and forms a protective chromia layer at the oxidation front. As the original concentration of Cr in the alloy is 12wt.%, the depletion in Cr during the oxidation causes a drop in the concentration levels

of Cr up to 8.28% as shown in Fig. 4.3.11 and Table 4.3.3. This depletion in the Cr concentration at the oxidation front permits the diffusion of Fe into chromia and it forms a Fe-Cr spinel. EDX analyses reported in Fig. 4.2.10 reveals that the Cr concentration within the inner oxide scale is higher than that of Fe. It can be said that the inner oxide which formed here is a Cr-rich Fe-Cr spinel. The formation of chromia at the oxidation front was also seen but it is not thick and uniform. The presence of Cr_2O_3 particles in a Fe-Cr spinel is shown in Fig. 4.2.6. The presence of dislocations at the oxidation front vanishes as the time of oxidation increases by means of recovery and recrystallisation. One other important factor is the depth of the affected zone due to the shot-peening. If the depth of the affected zone is in the range of a few micrometers, the internal oxidation occupies this zone completely and the beneficial effect of dislocations diminishes. The microstructure of the oxidation front of the SPCr-12 is shown in Fig. 4.3.10. Presence of a low dislocation density near the shot-peened surface can be observed. This gives rise to the idea that the dislocations which were present during the initial stage of oxidation vanish by means of recovery. It must be noted that a quick formation of a chromia layer and the continuous supply of Cr to the oxidation front is needed to maintain Cr_2O_3 formation to prevent internal oxidation and decrease the oxidation kinetics. This has occurred in case of SPCr-18, where a multi-layer oxide comprised of an outer CuO , inner FeCr_2O_4 and Cr_2O_3 was transformed into a single layer of Cr_2O_3 by the shot-peening treatment. A summarizing scheme of the shot-peening effect on these steels is given by means of the schematic diagram which is presented in Fig. 6.3.1.

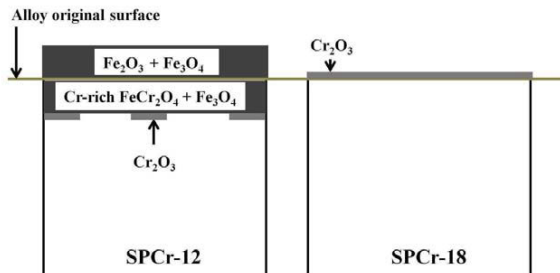


Fig. 6.3.1: Schematic representation of the shot-peening effect on the oxide scales developed on SPCr-12 and SPCr-18 after oxidation at 750°C.

The comparison of the schematics presented in Fig. 6.2.1 and Fig. 6.3.1 explain the difference between the oxidation mechanisms of non-SP and SP sides of Cr-12 and Cr-18. Microstructural differences at the oxidation front of SP and non-SPCr-12 reveal some interesting

phenomena. Firstly, the internal precipitation zone in case of non-SPCr-12 is absent in SPCr-12. The grain boundary oxidation which was observed in case of non-SPCr-12 was not present in case of SPCr-12. The thickness of the oxide scale in case of SPCr-12 was found to be smaller than that of non-SPCr-12. EDX spot analysis performed at the oxidation front of the non-SPCr-12, which is presented in Fig. 4.3.15, confirms that the Cr concentration at the metal/oxide interface reduced to 4wt.%. This indicates the depletion of Cr at the interface which in turn promotes the internal diffusion of oxygen to form an internal oxidation zone. The situation at this interface in case of SPCr-12 is improved as the Cr concentration is around 8wt.%. This is due to the enhanced diffusion of Cr along dislocations. As the Cr content in the alloy is too low to supply continuous flow to the oxidation front, even shot-peening could not help to form a chromia layer at the oxidation front. In contrary SPCr-18 showed better oxidation resistance by forming a thin homogeneous chromia layer on the surface. It should be noted that the presence of dislocations is not helpful alone to develop a chromia layer and that the Cr content in the alloy is also an important factor. In order to improve the oxidation behaviour of shot-peened steels a new concept named dislocation engineering is applied to the shot-peened steel which is discussed as following.

6.4 Dislocation engineering

It was already shown and discussed that the dislocations introduced by shot-peening can help in enhancing the Cr diffusion to the surface which in turn promotes the chromia layer formation. However, dislocations are not stable at high temperatures as already observed, and there is a need to stabilise the dislocations. Vacuum annealing prior to the oxidation can stabilise the dislocations into cells with fine spacings (recovery), but too high a temperature or time can cause recrystallisation. It is important to determine the optimal heat treatment before the oxidation so that a protective oxides scale formation results. Based on this idea, SPCr-12 and SPCr-18 were pre-annealed in vacuum at 750°C for different annealing times. It was found from the hardness measurement results which are shown in Table 4.3.1 that both shot-peened steels have undergone recovery during the annealing process. From the experimental observations, the shot-peened steels which were in a state of recovery were chosen for the oxidation measurements (depending on the fact that the change in the hardness profiles of the annealed SP steels is not so high as they will be after recrystallisation). After oxidising the SPCr-18 and SPCr-12 which were pre-annealed for different annealing times, the mass gains determined. The results are presented in Fig. 4.3.1 (a) and (b) respectively. The oxidation be-

behaviour of SPCr-12 was found to be changed considerably as a consequence of the pre-annealing treatment. The lowest mass gain was observed in case of SPCr-12 + 1 h pre-annealed and the mass gain was increased as the pre-annealing time increased. In case of SPCr-18 the pre-annealing effect seems to be less influential. The in-situ pre-annealing and AES measurements performed, which are presented in Fig. 4.3.4 for SPCr-18, reveal that the pre-annealing was enhancing the Cr diffusion through the dislocations and surface becomes enriched by more Cr. It was shown that the shot-peening was successful in forming a chromia layer on the surface of SPCr-18 after oxidation due to the high Cr concentration in the base alloy. In the pre-annealing case a quick formation of chromia layer was expected by means of point defects created during annihilation of dislocations, which enhances the diffusional growth. The Cr oxide grows basically by means of outward cation diffusion. The cation defects such as vacancies/interstitials can be annihilated/created by dislocation climb in the metal when the shot-peened steel is subjected to heating.

Results from the TEM investigation of a SPCr-12 + 5 h pre-annealed sample which was oxidised for 92 h is presented in Fig. 4.3.12 and Fig. 4.3.13. The presence of a high dislocation density shows dislocations being arranged in a network was observed in this examination. That means even after pre-annealing and oxidising for 92 h, still the dislocations were present at the subsurface region. A schematic representation of the subsurface microstructure of the SPCr-12 + 5 h pre-annealed sample is presented in Fig. 6.4.1. A network of dislocations which forms a group of subboundaries during the annealing procedure results in a reduced dislocation density as compared to the original shot-peened surface.

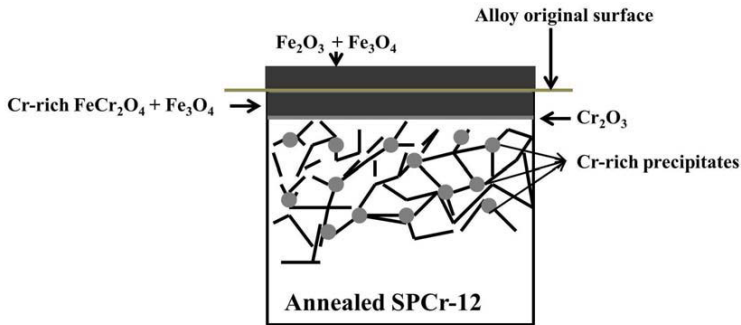


Fig. 6.4.1: Schematic representation of the microstructure of the subsurface of the pre-annealed and oxidised SPCr-12 sample.

Fig. 6.4.1 illustrates that the thickness of the outer oxide scale and the inner scale decreased comparatively to the oxidised SPCr-12 shown in Fig. 6.3.1. Another important observation was that a thin chromia layer formed at the oxidation front in case of SPCr-12 + pre-annealed. The subsurface was filled with a network of dislocations (probably a group of sub-boundaries) as shown in Fig. 6.4.1. These networks were assumed to be formed during the recovery process by means of dislocation climb often called polygonisation. These networks last for a longer time as the dislocation density was reduced. It can be stated that the dislocations were stabilised and serve as a network of fast diffusion paths for Cr for a longer time. The Cr-rich precipitates as shown in Fig. 6.4.1 are using these networks to diffuse faster to the oxidation front and maintain a sufficient amount of Cr to form a continuous chromia layer at the oxidation front.

6.5 Simulation of the external scale formation and effect of shot-peening

Based on the experimental observations, a few changes were made in the existing software **InCorr**. As **InCorr** simulates the internal oxidation processes, it excludes the transport of Fe and oxygen through the outer oxide layer. In the present work, no effective diffusion coefficient of oxygen was considered for the oxide scale growth. However, the model for the outer oxide scale growth was based on strong assumptions. One of those main assumptions was that a very thin outer scale was considered on the surface before the simulation starts. This enables to consider the diffusion coefficient of oxygen and iron through the outer scale. Another assumption was that underneath the outer scale and on the alloy original surface oxygen was assumed to be present as per the equilibrium calculations performed by FactSage (the partial pressure of oxygen at the outer/inner scale interface, i.e., equilibrium partial pressure of the $\text{Fe}_2\text{O}_3/\text{Fe}_3\text{O}_4$ interface as predicted by Fig. 4.1.1). By sticking to the boundary conditions, the simulations were performed on Cr-12 and a Ni-based alloy. The results were found to be in good agreement with the experiment, although, the simulation results did not consider the effect of microcracks and pores that formed in the oxide scales.

The shot-peening effect was modelled on the basis of experimental observations. A change in the diffusion mechanisms of oxygen and chromium was observed due to the shot-peening. Shot-peening allows Cr to diffuse faster than the internal diffusion of oxygen. An individual presence of a dislocation could not be implemented in the mesh, rather an effective area which was assumed to have a high dislocation density with an enhanced diffusion coefficient of Cr by a factor of 10^3 was introduced in the model. The depth of this zone was estimat-

ed by means of the hardness profile of the shot-peened steel. This enhancement in Cr diffusion increases the Cr flux to the surface and the Cr concentration at the surface increases. It enables the transition of an internal and external oxide structure into a single layered chromium oxide in case of SPCr-18. As for the experimental observations showed that the dislocations annihilated or disintegrated by means of recrystallisation after some time when the samples were subjected to oxidation. This time was estimated according to Table 4.3.1 and after this time the enhancement factor in the diffusion coefficient of Cr was deleted from the calculation. The simulated thickness results in case of SPCr-18 are found to be in reasonable agreement with the experimental results.

7 Conclusions and future aspects

The aim of this work was to study the influence of Cr-content on the oxidation behaviour of boiler steels and to model the oxidation kinetics based on the experimental results. Further, the effect of the surface modification techniques such as shot-peening and dislocation engineering were studied and the modelling was extended to include the effect of shot-peening on the oxidation behaviour.

Several oxidation tests were performed on the 9, 12 and 18wt.% Cr steels at both 700°C and 750°C. From these results it can be concluded that the Cr concentration in the base alloy severely influences the oxidation kinetics. It was found that the austenitic steels having 18wt.% Cr showed good oxidation resistance compared to the 9 and 12wt.% Cr steels at both 700°C and 750°C. None of the alloys succeeded in forming a compact Cr₂O₃ scale on the surface of the material which is required to provide guaranteed protection against oxidation. From the gold marker experiments shown in the same section, the mechanisms of the outer scale and inner scale formations were understood.

To improve the oxidation kinetics of the alloys, shot-peening treatment was applied on 12 and 18wt.% Cr steels and the effect was experimentally verified on these alloys and discussed. It was found that the shot-peening treatment was very efficient in decreasing the oxidation kinetics on the applied materials. It was seen that the shot-peening effect on the austenitic steel was more pronounced than on the 12wt.% Cr steel. A compact Cr₂O₃ layer was able to form on the surface of the 18wt.% Cr steel whereas in case of 12wt.% Cr steel an enrichment of Cr in the inner scales was observed and non-uniform Cr₂O₃ was observed at the metal/oxide interfaces.

It is shown that the shot blasting effect is associated with a microstructural change of the metallic surface, which changes the oxidation mechanism in the transient state. Dislocations created by shot-peening near the surface resulted in enhanced permeation of chromium which helped in the formation of a protective Cr-rich layer near the metal/oxide interface in case of 12wt.% Cr steels. After longer periods of oxidation, the dislocations could disappear by means of recovery and recrystallisation. At 700°C the enhancement of Cr was not enough to form a Cr-rich spinel whereas at 750°C a Cr-rich Fe-Cr spinel was formed as inner scale and the spinel slows down the oxidation kinetics. In addition to the extent and uniformity of shot-peening effect, reliability of this method depends on the Cr-content in the base alloy. Efforts to quantify the degree of shot-peening by measuring dislocation density proved difficult. As

this entire process was an integral effect of grain boundaries, subgrains in addition to the residual stress effect of shot-peening the effect of sample preparation techniques such as erosion cutting, milling and sample shape especially at the corners of the concave and convex shapes had shown considerable influence on oxide morphology and kinetics. The quantification of the enhancement in the diffusion coefficient of Cr could not be carried out as it requires some very carefully controlled diffusion measurements. In case of 12wt.% Cr steel the difference in the oxidation behaviour due to shot-peening at 700°C and 750°C could be investigated in more detail by measuring the temperature dependence of the kinetics of oxidation, and using this data to calculate the effective activation energy for diffusion of Cr in the shot-peened steels.

To study other means of enhancing oxidation resistance of these alloys, the effects of dislocation engineering were studied. The dislocation engineering concept was applied on both 12wt.% Cr and 18wt.% Cr steel which was discussed in detail. The main idea was to form stable network of dislocations at higher temperatures for longer time. This was achieved by pre-annealing the shot-peened steels in vacuum (at the same temperature where the oxidation tests will be performed) until the samples undergo a certain extent of recovery where the process of dislocation climb was active and resulted in the formation of a network of subboundaries. The density of dislocations decreased with the duration of annealing treatment, as would be expected from recovery and recrystallisation. Considerable change in the oxidation kinetics of shot-peened 12wt.% Cr steel was found when a preannealing treatment was given following shot-peening.

Dislocations formed a network at the metal/oxide interface as expected initially and they still retain after 92 h of oxidation. The diffusion of Cr from the metal to the subsurface region was continuously enhanced without being depleted. This helped to form a uniform chromium oxide scale at the metal/oxide interface in case of 12wt.% Cr steel. In case of high Cr austenitic steel this effect was found to support a quick formation of a chromium oxide scale on the surface as the shot-peening itself was able to change the diffusion mechanisms at the subsurface. A detailed analysis of dislocation structure evolution using FIB and TEM was beyond the scope of this work.

A more systematic study of the effect of shot-peening can be conducted by varying the shot-peening pressures and the extent of shot-peening as a part of future work. One such suggestion for future work is to pre-anneal the shot-peened steels in ultra-high vacuum for shorter times and check the dislocation evolution at each annealing time and then to oxidise the sam-

ples in-situ in AES and measure the depth profiles of elements in oxide layers. This would give more information about the diffusion mechanisms in the subsurface area. It is proposed that this dislocation engineering must be applied to the alloys and examine the oxidation behavior in water vapour environment to commercialise this process.

Based on the experimental results a model for the simultaneous oxide scale growth was developed. A model for the effect of shot-peening was also proposed. It must be noted that this model did not consider the effect of the individual contribution of the dislocations towards enhancement in the diffusion coefficient of Cr as it requires a much more complex mesh which was not possible with the used finite difference method technique used. The depth of the shot-peened area calculated from the hardness profiles and the microstructural investigation was used as a source for an effective enhanced diffusion coefficient for the Cr diffusion. The simulation results were found to be satisfactorily closer to the experimentally obtained results.

The modification of the mesh from a square shaped grain structure to the honeycomb shaped structure was implemented by using a more advanced finite element method. As a future aspect the grain shapes of inner oxides and outer oxide scales can be introduced in the mesh as the outer oxide grains look more lamellar in shape and inner oxide grains are coaxial in nature. Introduction of mobilities and chemical potentials instead of using diffusion coefficients and concentrations of the species would solve non-Fickian diffusion problems, where diffusion occurs from low concentration to high concentration especially in oxide scales, even though lack of mobility data along grain boundaries and in many oxides is a major obstacle. As an initial point this approach can be implemented on a simple Fe-oxidation and later can be applied to more complex alloying systems.

8 References

1. S. Reschke, Technisch-wirtschaftliche Möglichkeiten der Herstellung von Stahlrohren, Doctorate Thesis, Rheinisch-Westfälischen Technischen Hochschule Aachen, 1994.
2. P. Grammelis, E. Kakaras, and N. Koukouzas. *The Situation of Coal-Fired Power Plants in Europe and European Union's Priorities*. In *International Conference on Clean Coal Technologies for our Future*, Chia Laguna 2002, 5.
3. J. Breton. *Comparative IGCC Cost and Performance for Domestic Coals*. In *Gasification Technology Conference*, San Francisco 2002, 156.
4. R. Viswanathan, J. Sarver, and J. M. Tanzosh, *Boiler Materials for Ultra-Supercritical Coal Power Plants—Steamside Oxidation*. *Journal of Materials Engineering and Performance*, **15**(3), 2006, 255.
5. R. Viswanathan and W. Bakker, *Materials for Ultrasupercritical Coal Power Plants-boiler Materials: Part 1*. *Journal of Materials Engineering and Performance*, **10**(1), 2001, 81.
6. R. Viswanathan and W. Bakker, *Materials for Ultrasupercritical Coal Power Plants - Turbine Materials: Part 2*. *Journal of Materials Engineering and Performance*, **10**(1), 2001, 96.
7. M. Staubli, K. H. Mayer, T. U. Kern, R. W. Vanstone, R. Hanus, J. Stief, and K. H. Schonfeld. *Power Generation in the 21st Century*. In *3rd EPRI Conference on Advance in Materials Technologies for Fossil Power Plants*, U.K., 2001, 15.
8. I. I. Reformatskaya, V. A. Ryzhenkov, I. G. Rodionova, I. I. Ashcheulova, V. V. Yakushev, and V. D. Kiselev, *Corrosion of Heating Surfaces of Power Station Boiler Equipment made of Steel 12X18H10T*. *Protection of Metals*, **39**(6), 2003, 537.
9. I. I. Reformatskaya, A. N. Podobaev, G. M. Florianovich, and I. I. Ashcheulova, *Evaluation of the Corrosion Resistance of Low-carbon Pipe Steels under Conditions of Hot-water Supply*. *Protection of Metals*, **35**(1), 1999, 4.
10. L. I. Freiman, Y. M. Kolotykin, I. I. Reformatskaya, Y. P. Konnov, and A. E. Volkov, *Improved Efficiency of Alloying Stainless-Steel with Molybdenum by Reduction of Its Content of Sulfur and Manganese Inclusions*. *Protection of Metals*, **28**(2), 1992, 129.
11. N. J. Simms, J. R. Nicholls, and J. E. Oakey. *Materials for Solid Fuel Fired Gas Turbines: Burner Rig and Laboratory Studies*. In proceedings of *High Temperature Corrosion and Protection of Materials 5, Pts 1 and 2*, **369-3**, 2001, 833.
12. N. J. Simms and J. E. Oakey, *Protective Oxides in Coal-fired Combined Cycle Power Systems*. *Materials at High Temperatures*, **13**(2), 1995, 75.
13. N. J. Simms and J. E. Oakey. *Materials Issues in Coal-fired Combined Cycle Power Generation Systems: Laboratory versus Plant Testing*. In proceedings of *High Temperature Corrosion and Protection of Materials 4, Pts 1 and 2*, **251-2**, 1997, 543.

14. G. R. Wallwork and A. Z. Hed, *Some Limiting Factors in Use of Alloys at High Temperatures*. *Oxidation of Metals*, **3**(2), 1971, 171.
15. G. R. Wallwork and A. Z. Hed, *Some Limiting Factors in Use of Metal Alloys for High Temperatures*. *Journal of the Electrochemical Society*, **117**(8), 1970, C254.
16. R. Peraldi and B. A. Pint, *Effect of Cr and Ni Contents on the Oxidation Behavior of Ferritic and Austenitic Model Alloys in Air with Water Vapor*. *Oxidation of Metals*, **61**(5-6), 2004, 463.
17. B. A. Pint, R. Peraldi, and P. J. Maziasz. *The Use of Model Alloys to Develop Corrosion-resistant Stainless Steels*. In proceedings of *High Temperature Corrosion and Protection of Materials 6, Part 1 and 2*, **461-464**, 2004, 815.
18. S. E. Sadique, A. H. Mollah, M. S. Islam, M. M. Ali, M. H. H. Megat, and S. Basri, *High-temperature Oxidation Behavior of Iron-chromium-aluminum Alloys*. *Oxidation of Metals*, **54**(5-6), 2000, 385.
19. L. Sánchez, M. P. Hierro, and F. J. Pérez, *Effect of Chromium Content on the Oxidation Behaviour of Ferritic Steels for Applications in Steam Atmospheres at High Temperatures*. *Oxidation of Metals*, **71**(3-4), 2009, 173.
20. V. Trindade, H.-J. Christ, and U. Krupp, *Grain-Size Effects on the High-Temperature Oxidation Behaviour of Chromium Steels*. *Oxidation of Metals*, **73**(5), 2010, 551.
21. A. Nagode, B. Kosec, B. Ule, and G. Kosec, *Review of Creep Resistant Alloys For Power Plant Applications*. *Metalurgija*, **50**(1), 2011, 45.
22. A. Nagode, B. Ule, M. Jenko, and L. Kosec, *A Constitutive Creep Equation for 9Cr-1Mo-0.2V (P91-type) Steel under Constant Load and Constant Stress*. *Steel Research International*, **78**(8), 2007, 638.
23. D. J. Young, *High Temperature Oxidation and Corrosion of Metals*, London: Elsevier. 2008.
24. A. S. Khanna, *Introduction to High Temperature Oxidation and Corrosion*: ASM International. 2002.
25. P. Kofstad, *High Temperature Corrosion*, London: Elsevier. 1969.
26. P. Kofstad, *Non Stoichiometry, Diffusion, and Electrical Conductivity in Binary Metal Oxides*, New York: Wiley-Interscience. 1972.
27. P. Kofstad, *High Temperature Oxidation of Metals*, New York: John Wiley & Sons. 1966.
28. D. V. Thornton and K. H. Meyer, "European High Temperature Materials Developemnt" in *Advanced Heat Resistant Steels for Power Generation*. IOM communication Ltd, ed. E. R. Viswanathan and J. W. Nutting, London: 1999.
29. J. Pilling and N. Ridley, *Tempering of 2.25Cr-1Mo Low-Carbon Steels*. *Metallurgical Transactions A*, **13**(4), 1982, 557.

30. R. K. S. Raman, *Influence of Microstructural Variations in the Weldment on the High-Temperature Corrosion of 2.25Cr-1Mo Steel*. Metallurgical and Materials Transactions A, **26**(7), 1995, 1847.
31. R. K. S. Raman and B. C. Muddle, *Role of High Temperature Corrosion in Life Assessment and Microstructural Degradation of Cr-Mo Steel Weldments*. International Journal of Pressure Vessels and Piping, **77**(2-3), 2000, 117.
32. P. Roy and T. Lauritzen, *The Relative Strength of Base-Metal and Heat-Affected Zone in 2.25Cr-1Mo Weldments - a Microstructural Evaluation*. Welding Journal, **65**(2), 1986, S45.
33. J. Hald, *Metallurgy and Creep Properties of New 9-12%Cr Steels*. Steel Research, **67**(9), 1996, 369.
34. F. Abe and M. Tabuchi, *Microstructure and Creep Strength of Welds in Advanced Ferritic Power Plant Steels*. Science and Technology of Welding and Joining, **9**(1), 2004, 22.
35. A. Sundstrom and G. Ghai. Heat Resistant Austenitic Stainless Steel. US 6, 485,679 B1, 2002.
36. V. Raghavan, *Materials Science and Engineering, A first Course*, New Delhi: Prentice hall of India Pvt. Ltd. 2003.
37. B. C. Kyle, *Chemical and Process Thermodynamics*, New Delhi: Prentice Hall of India. 2000.
38. I. S. Stanley, *Chemical and Engineering Thermodynamics*, New York: John Wiley & Sons. 1997.
39. N. Birks, G. H. Meier, and F. S. Pettit, *Introduction to the High Temperature Oxidation of Metals*, Cambridge: Cambridge University Press. 2006.
40. C. Wagner, *Ionen und Elektronenleitung in Silberbromid und Abweichungen von der Idealen stochiometrischen Zusammensetzung*. Zeitschrift für Elektrochemie, **63**(9-10), 1959, 1027.
41. C. Wagner, *Reaktionstypen bei der Oxydation von Legierungen*. Zeitschrift für Elektrochemie, **63**(7), 1959, 772.
42. A. Fick, *Über Diffusion*. Annalen der Physik and Chemie, **94**, 1855, 59.
43. A. Fick, *On Liquid Diffusion (Reprinted from the London, Edinburgh, and Dublin Philosophical Magazine and Journal of Science, Vol 10, Pg 30, 1855)*. Journal of Membrane Science, **100**(1), 1995, 33.
44. N. A. Gjostein, *Short Circuit Diffusion*. Diffusion, ed. H.I. Aaronson, Ohio, American Society for Metals: 1973.
45. H. Mehrer, *Diffusion in Solids*. Springer series Berlin: Springer 2007.

8 References

46. H. G. Sockel, B. Saal, and M. Heilmaier, *Determination of the Grain-Boundary Diffusion-Coefficient of Oxygen in Cr₂O₃*. *Surface and Interface Analysis*, **12**(1-12), 1988, 531.
47. A. C. S. Sabioni, A. M. Huntz, F. Silva, and F. Jomard, *Diffusion of Iron in Cr₂O₃: Polycrystals and Thin Films*. *Materials Science and Engineering: A*, **392**(1-2), 2005, 254.
48. A. Atkinson, *Diffusion Along Grain-boundaries and Dislocations in Oxides, Alkali-Halides and Carbides*. *Solid State Ionics*, **12**(Mar), 1984, 309.
49. R. S. Barnes, *Diffusion of Copper Along the Grain Boundaries of Nickel*. *Nature*, **166**(4233), 1950, 1032.
50. H. Gleiter, *Microstructure*. *Physical Metallurgy*, ed. R.W. Cahn and P. Haasen, Amsterdam, North-Holland Publishing: 1983.
51. R. W. Balluffi, *Grain-Boundary Diffusion Mechanisms in Metals*. *Diffusion in Crystalline Solids*, ed. G.E. Murch and A.S. Nowick, Academic Press, Inc.,: 1984.
52. D. Wolf and S. Yip, *Materials Interfaces - Atomic-Level Structure and Properties*, London: Chapman and Hall. 1992.
53. J. C. Fisher, *Calculation of Diffusion Penetration Curves for Surface and Grain Boundary Diffusion*. *Journal of Applied Physics*, **22**(1), 1951, 74.
54. I. Kaur, Y. Mishin, and W. Gust, *Fundamentals of Grain and Interface Boundary Diffusion*, New York: John Wiley and Sons, Ltd. 1995.
55. L. G. Harrison, *Influence of Dislocations on Diffusion Kinetics in Solids with Particular Reference to Alkali Halides*. *Transactions of the Faraday Society*, **57**(8), 1961, 1191.
56. I. V. Belova and G. E. Murch, *The Transition from Harrison Type-B to Type-A Kinetics in Grain-boundary Tracer Diffusion*. *Philosophical Magazine A*, **81**(10), 2001, 2447.
57. E. W. Hart, *On the Role of Dislocations in Bulk Diffusion*. *Acta Metallurgica*, **5**(10), 1957, 597.
58. S. William F, *Principles of Materials Science and Engineering*, New York: McGraw-Hill Book Company. 1931.
59. I. Altenberger, B. Scholtes, U. Martin, and H. Oettel, *Cyclic Deformation and Near Surface Microstructures of Shot peened or Deep Rolled Austenitic Stainless Steel AISI 304*. *Materials Science and Engineering A*, **264**(1-2), 1999, 1.
60. A. Blarasin, M. Guagliano, and L. Vergani, *Fatigue Crack Growth Prediction in Specimens Similar Spur Gear Teeth*. *Fatigue & Fracture of Engineering Materials & Structures*, **20**(8), 1997, 1171.
61. L. Wagner, *Mechanical Surface Treatments on Titanium, Aluminum and Magnesium Alloys*. *Materials Science and Engineering A*, **263**(2), 1999, 210.

62. J. O. Almen and P. H. Black, *Residual Stresses and Fatigue in Metals*, New York: McGraw-Hill Publ. Company. 1963.
63. K. J. Marsh, *Shot Peening: Techniques and Applications*, London: EMAS. 1993.
64. M. Guagliano, *Relating Almen Intensity to Residual Stresses Induced by Shot peening: A Numerical Approach*. Journal of Materials Processing Technology, **110**(3), 2001, 277.
65. M. Guagliano, *Fatigue Failure of a Bar of a Twin-screw Extruder for Plastics*. Engineering Failure Analysis, **12**(6), 2005, 950.
66. M. Guagliano, E. Riva, and M. Guidetti, *Contact Fatigue Failure Analysis of Shot-peened Gears*. Engineering Failure Analysis, **9**(2), 2002, 147.
67. V. Schulze, *Modern Mechanical Surface Treatment*, Weinheim: Wiley-VCH. 2006.
68. K. J. Miller. *The 27th John Players Lecture: Metal Fatigue - Past, Current and Future*. In proceedings of *The Institution of Mechanical Engineers*, **205**, 1991, 291.
69. K. Dai and L. Shaw, *Comparison Between Shot peening and Surface Nanocrystallization and Hardening Processes*. Materials Science and Engineering A, **463**(1-2), 2007, 46.
70. I. Fernandez-Pariente and M. Guagliano, *About the Role of Residual Stresses and Surface Work Hardening on Fatigue ΔK_{th} of a Nitrided and Shot peened Low-alloy Steel*. Surface & Coatings Technology, **202**(13), 2008, 3072.
71. J. L. Liu, M. Umemoto, Y. Todaka, and K. Tsuchiya, *Formation of a Nanocrystalline Surface Layer on Steels by Air Blast Shot Peening*. Journal of Materials Science, **42**(18), 2007, 7716.
72. L. Wang and D. Y. Li, *Mechanical, Electrochemical and Tribological Properties of Nanocrystalline Surface of Brass Produced by Sandblasting and Annealing*. Surface and Coatings Technology, **167**(2-3), 2003, 188.
73. X. Y. Wang and D. Y. Li, *Mechanical, Electrochemical and Tribological Properties of Nanocrystalline Surface of 304 Stainless Steel*. Wear, **255**(7-12), 2003, 836.
74. S. B. Fard and M. Guagliano, *Effects of Surfaces Nanocrystallization Induced by Shot peening on Material Properties : A Review*. Frattura ed Integrità strutturale, **7**, 2009, 3.
75. R. J. Hussey and M. Cohen, *Oxidation of Fe in Temperature Range 450-550°C, 2. Pressure Range 10^3 -760 Torr*. Corrosion Science, **11**(10), 1971, 713.
76. R. J. Hussey and M. Cohen, *Oxidation of Fe in Temperature Range 450-550°C, 1. Pressure range 10^0 - 10^4 Torr*. Corrosion Science, **11**(10), 1971, 699.
77. J. Païdassi, *The Kinetics of the Air oxidation of Iron in the Range 700-1250°C* Acta Metallurgica, **6**(3), 1958, 184.

78. D. P. Whittle and G. C. Wood, *Chromium Oxide Scale Growth on Iron-Chromium Alloys, 2. Influence of Alloy Composition*. Journal of the Electrochemical Society, **115**(2), 1968, 133.
79. G. C. Wood, *High-temperature oxidation of alloys*. Oxidation of Metals, **2**(1), 1970, 11.
80. G. C. Wood, M. G. Hobby, and B. Vaszko, *Electron-Probe Microanalysis of Nodular Scale Growth on Austenitic Stainless Steel*. Journal of the Iron and Steel Institute, **202**(8), 1964, 685.
81. G. C. Wood, T. Hodgkiess, and D. P. Whittle, *A Comparison of the Scaling Behaviour of Pure Iron-Chromium and Nickel-Chromium Alloys in Oxygen*. Corrosion Science, **6**(3-4), 1966, 129.
82. G. C. Wood and D. P. Whittle, *Chromium Oxide Scale Growth on Iron-Chromium Alloys, 1. Influence of Variables on Oxidation of Fe-28Cr*. Journal of the Electrochemical Society, **115**(2), 1968, 126.
83. J. E. Croll and G. R. Wallwork, *The Design of Iron-Chromium-Nickel Alloys for use at High Temperatures*. Oxidation of Metals, **1**(1), 1969, 55.
84. G. R. Wallwork, *Oxidation of Alloys*. Reports on Progress in Physics, **39**(5), 1976, 401.
85. V. R. Howes, *Oxide Growth and Spalling on Fe-Cr Alloys Studied by Hot Stage Microscopy*. Corrosion Science, **8**(10), 1968, 729.
86. P. K. Footner, D. R. Holmes, and D. Mortimer, *Oxidation of Iron-Chromium Binary Alloys*. Nature, **216**(5110), 1967, 54.
87. R. Dieckmann, *Defects and Cation Diffusion in Magnetite (Iv) - Nonstoichiometry and Point-Defect Structure of Magnetite $Fe_{3-\delta}O_4$* . Berichte der Bunsen-Gesellschaft-Physical Chemistry Chemical Physics, **86**(2), 1982, 112.
88. R. Dieckmann, C. A. Witt, and T. O. Mason, *Defects and Cation Diffusion in Magnetite(V) - Electrical-Conduction, Cation Distribution and Point-Defects in $Fe_{3-\delta}O_4$* . Berichte der Bunsen-Gesellschaft-Physical Chemistry Chemical Physics, **87**(6), 1983, 495.
89. J. Töpfer, S. Aggarwal, and R. Dieckmann, *Point Defects and Cation Tracer Diffusion in $(Cr_xFe_{1-x})_{3-\delta}O_4$ Spinels*. Solid State Ionics, **81**(3-4), 1995, 251.
90. P. Kofstad, *Defects and Transport Properties of Metal Oxides*. Oxidation of Metals, **44**(1), 1995, 3.
91. A. Holt and P. Kofstad, *Electrical-Conductivity and Defect Structure of Cr_2O_3 , 1. High-Temperatures ($> \sim 1000$ °C)*. Solid State Ionics, **69**(2), 1994, 127.
92. A. Holt and P. Kofstad, *Electrical-Conductivity and Defect Structure of Cr_2O_3 , 2. Reduced Temperatures ($< \sim 1000$ °C)*. Solid State Ionics, **69**(2), 1994, 137.

93. K. Hoshino and N. L. Peterson, *Cation Self-Diffusion in Cr₂O₃*. Journal of the American Ceramic Society, **66**(11), 1983, C202.
94. A. C. S. Sabioni, A. M. Huntz, F. Millot, and C. Monty, *Self-diffusion in Cr₂O₃, 3. Chromium and Oxygen Grain-boundary Diffusion in Polycrystals*. Philosophical Magazine A, **66**(3), 1992, 361.
95. A. C. S. Sabioni, A. M. Huntz, F. Millot, and C. Monty, *Self-Diffusion in Cr₂O₃, 2. Oxygen Diffusion in Single-Crystals*. Philosophical Magazine A, **66**(3), 1992, 351.
96. A. C. S. Sabioni, A. M. Huntz, J. Philibert, B. Lesage, and C. Monty, *Relation between the Oxidation Growth-Rate of Chromia Scales and Self-Diffusion in Cr₂O₃*. Journal of Materials Science, **27**(17), 1992, 4782.
97. R. E. Lobnig, H. P. Schmidt, K. Hennesen, and H. J. Grabke, *Diffusion of Cations in Chromia Layers Grown on Iron-Base Alloys*. Oxidation of Metals, **37**(1-2), 1992, 81.
98. M. G. C. Cox, V. D. Scott, and B. Mcenaney, *Chemical Diffusion Model for Partitioning of Transition-Elements in Oxide Scales on Alloys*. Philosophical Magazine, **26**(4), 1972, 839.
99. M. G. Hobby and G. C. Wood, *The Role of Nickel in the High-Temperature Oxidation of Fe-Cr-Ni Alloys in Oxygen*. Oxidation of Metals, **1**(1), 1969, 23.
100. D. L. Douglass and J. S. Armijo, *The Effect of Silicon and Manganese on the Oxidation Mechanism of Ni-20Cr*. Oxidation of Metals, **2**(2), 1970, 207.
101. J. Benard, *L'Oxydation des Métaux II* Paris: Gauthier-Villars. 1964.
102. F. Masuyama, N. Komai, T. Yokoyama, S. Yamamoto, K. Miyata, and M. Igarashi, *3-year Experience with 2.25Cr-1.6W (HCM2S) and 12Cr-0.4Mo-2W (HCM12A) Steel Tubes in a Power Boiler*. JSME International Journal Series B-Fluids and Thermal Engineering, **41**(4), 1998, 1098.
103. H. Irie, F. Abe, and K. Yagi, *Recent Results of Long-term Creep Rupture Test*. Creep and Fracture of Engineering Materials and Structures, **171-1**, 2000, 17.
104. R. C. Thomson and H. K. D. H. Bhadeshia, *Carbide Precipitation in 12Cr1MoV Power-Plant Steel*. Metallurgical Transactions a-Physical Metallurgy and Materials Science, **23**(4), 1992, 1171.
105. F. H. Stott, I. G. Wright, T. Hodgkiess, and G. C. Wood, *Factors Affecting High-Temperature Oxidation Behavior of Some Dilute Nickel-Base and Cobalt-Base Alloys*. Oxidation of Metals, **11**(3), 1977, 141.
106. G. C. Wood and Hodgkies.T, *Mechanism of Oxidation of Dilute Nickel - Chromium Alloys*. Nature, **211**(5056), 1966, 1358.
107. G. C. Wood, Hodgkies.T, and D. P. Whittle, *A Comparison of Scaling Behaviour of Pure Iron-Chromium and Nickel-Chromium Alloys in Oxygen*. Corrosion Science, **6**(3-4), 1966, 129.

108. H. Hindam and D. P. Whittle, *Microstructure, Adhesion and Growth-Kinetics of Protective Scales on Metals and Alloys*. *Oxidation of Metals*, **18**(5-6), 1982, 245.
109. F. Burgahn, O. Vohringer, and E. Macherauch, *Micro-Residual-Stress States in Surface-Layers of Shot-Peened 42CrMo4*. *Zeitschrift für Metallkunde*, **84**(4), 1993, 224.
110. H. J. Grabke, E. M. Müller-Lorenz, S. Strauss, E. Pippel, and J. Woltersdorf, *Effects of Grain Size, Cold Working, and Surface Finish on the Metal-Dusting Resistance of Steels*. *Oxidation of Metals*, **50**(3-4), 1998, 241.
111. C. Ostwald and H. J. Grabke, *Initial Oxidation and Chromium Diffusion, 1. Effects of Surface Working on 9-20% Cr Steels*. *Corrosion Science*, **46**(5), 2004, 1113.
112. C. Piehl, Z. Tokei, and H. J. Grabke, *The Role of Fast Diffusion Paths in the Selective Oxidation of Chromium Steels*. *Diffusions in Materials: Dimat2000, Pts 1 & 2*, **194-1**, 2001, 1689.
113. C. Piehl, Z. Tokei, and H. J. Grabke, *Surface Treatment and Cold Working as Tools to Improve Oxidation Behaviour of Chromium Steels*. *High Temperature Corrosion and Protection of Materials 5, Pts 1 and 2*, **369-3**, 2001, 319.
114. H. J. Grabke, Z. Tokei, and C. Ostwald, *Initial Oxidation of a 9%CrMo- and a 12%CrMoV-steel*. *Steel Research International*, **75**(1), 2004, 38.
115. Z. D. Xiang and P. K. Datta, *Shot peening Effect on Aluminide Diffusion Coating Formation on Alloy Steels at Low Temperatures*. *Scripta Materialia*, **55**(12), 2006, 1151.
116. C. Piehl, Z. Tokei, and H. J. Grabke, *Influence of Chromium Diffusion and Different Surface Finishes on the Oxidation Behaviour of Chromium Steels*. *Materials at High Temperatures*, **17**(2), 2000, 243.
117. R. Naraparaju, H. J. Christ, F. Renner, and A. Kostka, *Effect of Shot-peening on the Oxidation Behaviour of Boiler Steels*. *Oxidation of Metals*, **76**(3), 2011, 233.
118. L. Xingeng and H. Jiawen, *Effect of shot blasting on oxidation behavior of TP304H steel at 610–770 °C in water vapor*. *Materials Letters*, **60**(3), 2006, 339.
119. R. Naraparaju, V. B. Trindade, H. J. Christ, and U. Krupp, *Effect of Shot peening on High Temperature Oxidation Behaviour of Boiler Steel: Experimental Results and Simulation*. *Corrosion Engineering Science and Technology*, **44**(3), 2009, 211.
120. R. Dieckmann, T. O. Mason, J. D. Hodge, and H. Schmalzried, *Defects and Cation Diffusion in Magnetite (III) Tracer Diffusion of Foreign Tracer Cations as a Function of Temperature and Oxygen Potential*. *Berichte Der Bunsen-Gesellschaft-Physical Chemistry Chemical Physics*, **82**(8), 1978, 778.
121. R. Dieckmann and H. Schmalzried, *Defects and Cation Diffusion in Magnetite(II)*. *Berichte Der Bunsen-Gesellschaft-Physical Chemistry Chemical Physics*, **81**(4), 1977, 414.

122. R. Dieckmann and H. Schmalzried, *Defects and Cation Diffusion in Magnetite .I.* Berichte Der Bunsen-Gesellschaft-Physical Chemistry Chemical Physics, **81**(3), 1977, 344.
123. O. Kubaschewski and B. E. Hopkins, *Oxidation of Metals and Alloys*, London: Butterworths. 1962.
124. J. Friedel, *Dislocations*. Metallurgy and materials, London: Addison-Wesley publishing company, Inc. 1964.
125. H. G. V. Bueren, *Imperfections in crystals*. Series in Physics, Amsterdam: North-holland publishing co. 1960.
126. J. W. T. Read, *Dislocations in Crystals*. International series in pure and applied physics, New York: McGraw-Hill Book company, Inc. 1953.
127. I. A. Ovid'ko and A. B. Reizis, *Grain-boundary Dislocation Climb and Diffusion in Nanocrystalline Solids*. Physics of the Solid State, **43**(1), 2001, 35.
128. H. J. Christ, H. G. Sockel, and W. Christl, *Aufkohlung von Hochtemperaturwerkstoffen – Teil I: Modellmäßige mathematische Beschreibung des Vorganges der Eindiffusion mit gleichzeitiger Ausscheidung einer Verbindung des eindringenden Elementes*. Materials and Corrosion, **37**(7), 1986, 385.
129. U. Krupp, V. B. Trindade, P. Schmidt, H. J. Christ, U. Buschmann, and W. Wiechert, *Oxidation Mechanisms of Cr-Containing Steels and Ni-base Alloys at High temperatures, Part II: Computer-based Simulation*. Materials and Corrosion, **57**(3), 2006, 263.
130. U. Krupp and H. J. Christ, *Internal Nitridation of Nickel-base Alloys, Part II. Behavior of Quaternary Ni-Cr-Al-Ti Alloys and Computer-based Description*. Oxidation of Metals, **52**(3-4), 1999, 299.
131. U. Krupp and H. J. Christ, *Internal Corrosion of Engineering Alloys: Experiment and Computer Simulation*. Journal of Phase Equilibria and Diffusion, **26**(5), 2005, 487.
132. V. B. Trindade, U. Krupp, H. J. Christ, M. J. Monteiro, and F. C. Rizzo, *Experimental Characterization and Computer-based Simulation of Thermodynamics and Kinetics of Corrosion of Steels at High Temperatures*. Materialwissenschaft und Werkstofftechnik, **36**(10), 2005, 471.
133. G. Zamponi, InCorr-Guide Book, Master Thesis, University of Siegen, 2006.
134. J. Crank, *The Mathematics of Diffusion*. 2nd ed., Oxford Clarendon Press. 1986.
135. V. B. Trindade, Hochtemperaturoxidation chromlegierter Stähle und von Nickel-Basislegierungen: Experimentelle Untersuchung und Computersimulation, Doctorate Thesis, University of Siegen, 2005.
136. V. B. Trindade, U. Krupp, and H. J. Christ, *Computer-Based Simulation of High-temperature Corrosion Phenomena*. Journal of the Brazilian Chemical Society, **19**(1), 2008, 157.

137. L. Himmel, R. F. Mehl, and C. E. Birchenall, *Self-Diffusion of Iron in Iron Oxides and the Wagner Theory of Oxidation*. Journal of Metals, **5**(6), 1953, 827.
138. J. D. Ans, *Taschenbuch für Chemiker und Physiker Band I – Physikalisch-chemische Daten*, Berlin: Springer-Verlag. 1992.
139. A. G. Crouch and J. Robertson, *Creep and Oxygen Diffusion in Magnetite*. Acta Metallurgica et Materialia, **38**(12), 1990, 2567.
140. S. Yamaguchi and M. Someno, *The Tracer Diffusivity of Oxygen in Wustite and Cobaltous Oxide*. Transactions of the Japan Institute of Metals, **23**(5), 1982, 259.
141. J. H. Swisher and Turkdoga, *Solubility Permeability and Diffusivity of Oxygen in Solid Iron*. Transactions of the Metallurgical Society of AIME, **239**(4), 1967, 426.
142. A. W. Bowen and G. M. Leak, *Diffusion in bcc Iron Base Alloys*. Metallurgical Transactions, **1**(10), 1970, 2767.
143. A. W. Bowen and G. M. Leak, *Solute Diffusion in Alpha-Iron and Gamma-Iron*. Metallurgical Transactions, **1**(6), 1970, 1695.
144. K. Hauffe, *Reaktionen in und an festen Stoffen*, Berlin: Springer-Verlag. 1966.
145. S. B. Jung, T. Yamane, Y. Minamino, K. Hirao, H. Araki, and S. Saji, *Interdiffusion and Its Size Effect in Nickel Solid-Solutions of Ni-Co, Ni-Cr and Ni-Ti Systems*. Journal of Materials Science Letters, **11**(20), 1992, 1333.
146. Z. Tokei, K. Hennesen, H. Viehhaus, and J. Grabke, *Diffusion of Chromium in Ferritic and Austenitic 9-20 wt-% Chromium steels*. Materials Science and Technology, **16**(10), 2000, 1129.
147. J. W. Park and C. J. Altstetter, *The Diffusion and Solubility of Oxygen in Solid Nickel*. Metallurgical Transactions A, **18**(1), 1987, 43.
148. R. C. Weast, *CRC Handbook of Chemistry and Physics*, Boca Raton, USA: CRC Press. 1986.
149. D. P. Whittle, Y. Shida, G. C. Wood, F. H. Stott, and B. D. Bastow, *Enhanced Diffusion of Oxygen during Internal Oxidation of Nickel-Base Alloys*. Philosophical Magazine A, **46**(6), 1982, 931.
150. A. C. S. Sabioni, B. Lesage, A. M. Huntz, J. C. Pivin, and C. Monty, *Self-Diffusion in Cr₂O₃, I. Chromium Diffusion in Single-Crystals*. Philosophical Magazine A, **66**(3), 1992, 333.
151. J. Ehlers, D. J. Young, E. J. Smaardijk, A. K. Tyagi, H. J. Penkalla, L. Singheiser, and W. J. Quadackers, *Enhanced Oxidation of the 9%Cr Steel P91 in Water Vapour Containing Environments*. Corrosion Science, **48**(11), 2006, 3428.
152. F. Jacob and B. Ted, *A First Course in Finite Elements*, Wet Sussex: John Wiley & Sons Ltd. 2007.

153. M. Auinger, R. Naraparaju, H. J. Christ, and M. Rohwerder, *Modelling High Temperature Oxidation in Iron–Chromium Systems: Combined Kinetic and Thermodynamic Calculation of the Long-Term Behaviour and Experimental Verification*. *Oxidation of Metals*, **76**(3), 2011, 247.
154. K. Kuroda, P. A. Labun, G. Welsch, and T. E. Mitchell, *Oxide-Formation Characteristics in the Early Stages of Oxidation of Fe and Fe-Cr Alloys*. *Oxidation of Metals*, **19**(3-4), 1983, 117.
155. C. Wagner, *Oxidation of Alloys Involving Noble Metals*. *Journal of the Electrochemical Society*, **103**(10), 1956, 571.
156. C. Wagner, *Formation of Composite Scales Consisting of Oxides of Different Metals*. *Journal of the Electrochemical Society*, **103**(11), 1956, 627.
157. R. A. Rapp, *The Transition from Internal to External Oxidation and the Formation of Interruption Bands in Silver-Indium Alloys*. *Acta Metallurgica*, **9**(8), 1961, 730.
158. C. Wagner, *Theoretical Analysis of the Diffusion Processes Determining the Oxidation Rate of Alloys*. *Journal of the Electrochemical Society*, **99**(10), 1952, 369.
159. F. Gesmundo and F. Viani, *Transition from Internal to External Oxidation for Binary-Alloys in the Presence of an Outer Scale*. *Oxidation of Metals*, **25**(5-6), 1986, 269.
160. R. A. Rapp, *Kinetics, Microstructures and Mechanism of Internal Oxidation - Its Effect and Prevention in High Temperature Alloy Oxidation*. *Corrosion*, **21**(12), 1965, 382.
161. E. Essuman, G. H. Meier, J. Zurek, M. Haensel, and W. J. Quadackers, *The Effect of Water Vapor on Selective Oxidation of Fe-Cr alloys*. *Oxidation of Metals*, **69**(3-4), 2008, 143.
162. J. E. Castle and P. L. Surman, *Self-Diffusion of Oxygen in Magnetite . Techniques for Sampling and Isotopic Analysis of Micro Quantities of Water*. *Journal of Physical Chemistry*, **71**(13), 1967, 4255.
163. G. Garnaud and R. A. Rapp, *Thickness of Oxide Layers Formed during Oxidation of Iron*. *Oxidation of Metals*, **11**(4), 1977, 193.
164. N. Appannagaari and S. N. Basu, *Modeling of O^{18} Tracer Distribution during Double Oxidation Experiments for Inward Growing Scales*. *Journal of Applied Physics*, **78**(3), 1995, 2060.
165. K. Nakagawa, Y. Matsunaga, and T. Yanagisawa, *Corrosion Behavior of Ferritic Steels on the Air Sides of Boiler Tubes in a Steam/air Dual Environment*. *Materials at High Temperatures*, **18**(1), 2001, 51.
166. W. Wegener and G. Borchardt, *Analysis of O^{18} Tracer Profiles in 2-Stage Oxidation Experiments, 1. Predominant Oxygen Diffusion in the Growing Scale*. *Oxidation of Metals*, **36**(3-4), 1991, 339.
167. R. Bredesen and P. Kofstad, *On the Oxidation of Iron in CO_2+CO Gas-Mixtures, 1. Scale Morphology and Reaction-Kinetics*. *Oxidation of Metals*, **34**(5-6), 1990, 361.

168. R. Y. Chen and W. Y. D. Yuen, *Oxidation of Low-Carbon, Low-Silicon Mild Steel at 450-900°C under Conditions Relevant to Hot-Strip Processing*. *Oxidation of Metals*, **57**(1-2), 2002, 53.

